

Dissertation
submitted to the
Combined Faculties for the Natural Sciences and for Mathematics
of the Ruperto-Carola University of Heidelberg, Germany
for the degree of
Doctor of the Natural Sciences

Presented by

Andrey Shornikov
born in Uralsk, USSR

Oral examination: 20th June 2012

An electron cooler for ultra-low energy cryogenic operation

Andrey Shornikov

Referees:

Prof. Dr. Andreas Wolf
Prof. Dr. Selim Jochim

Zusammenfassung: Es werden grundlegende Konzepte zur Erzeugung eines kalten und extrem niederenergetischen, magnetisch geführten Elektronenstrahls entwickelt, welcher als Elektronen-Kühler und -Target am elektrostatischen kryogenen Speicherring CSR dienen soll. Die Machbarkeit sehr langsamer Elektronenstrahlen, mit kinetischen Energien unterhalb eines Elektronenvolts und Stromdichten, die den Anforderungen von Elektronenkühlung und Elektron-Ion-Kollisionsexperimenten genügen, wurde durch Experimente am Elektronen-Target des Speicherrings TSR unter Verwendung einer kryogenen Kathode unter Beweis gestellt. Ein Vakuum- und Magnetfeldsystem wurde konzipiert, das die Verwendung dieses extrem niederenergetischen Elektronenstrahls im CSR ermöglicht. Ein neuartiges Verfahren zum Zusammenführen von Elektronen- und Ionenstrahlen wurde entwickelt und mit Hilfe numerischer Magnetfeld- und Teilchenspur-Simulationen analysiert. Ein Konzept zur Herstellung von Hochtemperatur-Supraleiter-Spulen, welche von Kryogen durchströmt werden, wird vorgestellt. Ein darauf basierender Spulenprototyp wurde gebaut und unter realistischen Bedingungen erfolgreich getestet. Um die Magnetspulen unabhängig von der Hauptkälteanlage des CSR zu betreiben, wurde ein auf tiefkaltem Neon basierendes zwei-Phasen-Niederdruck-Kühlsystem entwickelt, aufgebaut und erfolgreich in Betrieb genommen. Die hier vorgestellte Arbeit liefert somit ein experimentell getestetes Konzept für den Bau des CSR-Elektronen-Kühlers.

Abstract: Basic concepts are developed for realizing a cold, ultra-low energy, magnetically guided electron beam to serve as an electron cooler and an electron target for the electrostatic Cryogenic Storage Ring (CSR). The feasibility of ultra-low energy electron beams with sub-eV kinetic energy and densities sufficient for electron cooling and merged-beam collision experiments is demonstrated at the TSR electron target using a cryogenic electron source. A mechanical and magnetic system is laid out for implementing this ultra-low energy beam at the CSR. A new electron and ion beam merging scheme is developed and analyzed by numeric magnetic field and particle track calculations. The design concept of cryogen-filled HTS magnets was developed. For this purpose a prototype magnet was manufactured and tested under realistic operating conditions. A two-phase neon-based cryogenic low pressure cooling system to cool the magnets independent of the main CSR cooling machine was designed, constructed and successfully taken in operation. The reported work yields an experimentally tested design concept of the electron cooling system.

Contents

1	Introduction	1
1.1	Molecular, atomic and cluster physics with storage rings	1
1.2	Magnetic and electrostatic storage rings	3
1.3	Outline of this work	5
2	An electrostatic storage ring for electron-cooled ion beams	7
2.1	Overview of the CSR	7
2.1.1	Geometry and lattice	7
2.1.2	The lifetime of slow ions, vacuum conditions and cryogenic operation	8
2.1.3	Room temperature operation	9
2.2	Phase space cooling	10
2.3	Electron cooling	13
3	Ultra-low energy electron beams	19
3.1	Cold electron source	19
3.1.1	The cryogenic NEA photocathode	19
3.1.2	The electron gun	21
3.1.3	Transverse temperature and adiabatic magnetic expansion	22
3.2	Ultra-low energy electron deceleration experiments	24
3.2.1	Deceleration of a space charged limited electron beam	25
3.2.2	Measurements	32
3.3	Parameter ranges	37
3.4	Performance and modeling of an ultra-low energy cooling device at CSR	38
3.4.1	Longitudinal temperature and relaxation mechanisms	39
3.4.2	Cooling times of heavy ions	41
3.4.3	Magnetic system for the cooler	43
3.4.4	Model of the optics	47
3.4.5	Field quality and tracking	50
3.5	Summary	55
4	Realization of the CSR electron cooler	57
4.1	Magnets design and construction	57
4.1.1	Environment and general design concept	57
4.1.2	Magnets data	61
4.1.3	Magnet realization	62
4.1.4	Superconductive coils design	64
4.1.5	Construction of the test coil	69
4.2	Cryogenic cooling system	74
4.2.1	Concept of the cryogenic cooling system	74

4.2.2	Cryogenic cooling system design studies	76
4.2.3	Design of the heat exchanger and cryostat	80
4.2.4	Construction of the LPCS	82
4.2.5	Gas circulation and control system	86
4.3	Commissioning of the LPCS and the test magnet	89
4.3.1	Pre-operation tests of the LPCS	89
4.3.2	Taking the LPCS in operation	90
4.3.3	Joint test of the HTS magnet and the LPCS	93
4.4	Summary of the cryogenic tests	104
5	Summary and outlook	107

List of Figures

2.1	The CSR geometry and lattice.	8
2.2	Cryogenic concept of the CSR	9
2.3	The emittance and cooling	11
2.4	Lattice properties of the CSR.	12
2.5	Ion velocities in the co-moving frame.	12
2.6	Principle of electron cooling	13
2.7	Geometry of the collision.	14
2.8	Development of the electron cooling technology	18
3.1	Band diagram of a CsO coated GaAs surface-vacuum interface with NEA	20
3.2	Two-dimensional energy distribution of electrons emitted from the TSR GaAs photocathode electron source	21
3.3	Schematic of the TSR electron gun.	22
3.4	Adiabatic transverse expansion of an electron beam	24
3.5	Radial distribution of the space charge potential	27
3.6	Dimensionless potential ϕ as a function of s and u	29
3.7	Value of x for maximum current as a function of y	30
3.8	Analytical approximation compared to numerically integrated ϕ	31
3.9	Perveance as a function of x for the TSR electron target.	31
3.10	The TSR e-target in the ultra low energy operation mode	32
3.11	Potential diagram along the electron track.	33
3.12	Deceleration curve of a 8 μ A electron beam.	34
3.13	Rescaling of the retarding voltage into the actual potential difference	35
3.14	The maximum experimental perveance is found to be 4.1 μ perv.	36
3.15	Current enhancement due to beam deceleration.	37
3.16	Available electron density of the beam.	38
3.17	Longitudinal temperature and TLR relaxation.	40
3.18	TLR relaxation for a magnetized beam.	41
3.19	Longitudinal and transverse velocity spreads of electrons and ions	42
3.20	Cooling times of heavy singly charged ions	43
3.21	Guiding magnetic field providing an adiabatic transport as a function of the electron energy.	45
3.22	Influence of the toroidal field on ions.	46
3.23	The cooler optics model	48
3.24	Good field region.	51
3.25	Adiabatic electron transport	52
3.26	Compensation scheme.	53
3.27	Angular spread of 300 keV proton beam.	54
4.1	The CSR outer vacuum construction	58

4.2	The model and the manufactured CSR linear chamber.	59
4.3	Preliminary design of the XHV beam line in the cooler section.	59
4.4	Layout of the CSR merging chamber	60
4.5	Electrical resistivity of copper at cryogenic conditions.	63
4.6	HTS coil body	65
4.7	HTS coil assembly	66
4.8	HTS coil section view	67
4.9	HTS coil current feedthrough	68
4.10	HTS coil cryogen couplings	69
4.11	Coil body with HTS wound HTS wire	70
4.12	HTS soldering process	71
4.13	In sealings	72
4.14	Mounting of a corner flange	73
4.15	LN test of the resistance	73
4.16	Simplified scheme of the LPCS	75
4.17	Cooling capacity of the Leybold 140T Coolpower	76
4.18	The condenser	77
4.19	A schematic counter-flow heat exchanger.	77
4.20	The circulation scheme in the heat exchanger.	80
4.21	The LPCS tower design	82
4.22	The heat exchanger assembly	84
4.23	Construction of the condenser assembly	85
4.24	The mechanical decoupling of the cold head	86
4.25	Connections in the cryostat	86
4.26	Control and diagnostics scheme of LPCS	87
4.27	The external gas circuit of the LPCS	89
4.28	First condensation event	91
4.29	Transfer of cooling power to the short cut load	92
4.30	Runaway of the cooling system	93
4.31	Preparing the coil to the test.	95
4.32	The test magnet in cryostat	96
4.33	Mass spectra of the residual gas in the load cryostat	98
4.34	Change of mass 20 QMS signal.	98
4.35	Transfer of the cooling power to the load at 1.1 bar working pressure.	99
4.36	Transfer of the cooling power to the load at 1.5-1.6 bar working pressure.	100
4.37	Transferred cooling power as a function of the flow rate.	101
4.38	Field produced by the test coil.	103
4.39	Test of a conductively cooled HTS prototype coil.	103
4.40	Resistance of the conductively cooled prototype coil	104

Chapter 1

Introduction

1.1 Molecular, atomic and cluster physics with storage rings

In space, over 150 molecules have been identified to the moment in diverse sources such as circumstellar envelopes, cold and hot gas interstellar cloud cores, galactic center clouds and outflows [1]. Approximately 50 of them are complex organic molecules having more than 6 atoms, with carbon as the most common heavy element. In cold interstellar cloud cores only exothermic barrier-free reactions, such as reactions of neutral atoms with positive ions, can form such molecules in gas-phase reactions [2]. Negative ions, first found in space in 2006 [3], and 5 different species being identified up to now [4], also contribute in the interstellar chemistry. To explain the observed abundances of molecules and their formation mechanisms, astrochemistry demands for experimental input on fundamental interactions of negative and positive organic ions with electrons, neutrals and photons. These reactions include electron-ion recombination, photoexcitation and photodetachment which can all be dissociative.

Another astrophysics area requiring more data on electron-ion collisions is the physics of collisionally ionized plasmas driven by electron impact ionization (EII). Such plasmas are formed in many astrophysical sources, including stellar coronae, active galactic nuclei and supernova remnants. An equilibrium state of such plasmas is characterized by a certain charge state distribution (CSD) which must be taken into account to extract plasma density, temperature and composition from observed spectroscopic data. To calculate equilibrium CSDs, the ionization cross-sections and recombination rates of all plasma components must be known [5].

Molecular physics is also the basis for many processes in terrestrial environments, such as abiotic synthesis of organic molecules and creation of the first biological molecules from inorganic matter (abiogenesis). Beyond the molecular physics area, on the boundary of molecular and solid state physics the fast growing area of cluster physics demands for experimental input on non-planar clusters [6] to develop a comprehensive theory

of thermal and electronic properties of such objects and promote new advances in the theory of metals and solid state. In recent years, numerous types of metal and carbon cluster were successfully produced in form of negative ions and studied in ion storage and trapping devices (Al_n^- [7], Co_n^- , Cu_n^- , Ni_n^- , Na_n^- [8], C_n^- [9]).

Many of the mentioned experimental data on ionization and recombination processes crucial for astrophysics, molecular, plasma and cluster physics, can be obtained in laboratory experiments with storage rings. The greatest advantage of storage rings compared to single-pass devices is the powerful set of beam diagnostic and quality enhancement techniques available. One of the most outstanding techniques is phase space cooling. The phase space cooling in a storage ring compresses the stored ion beam in space and reduces its momentum spread, enhancing several experimental conditions at once. First of all it reduces the transverse beam size making it well localized. If then the cooled beam is used in an experiment where an ion reacts with an incident electron or photon, the products measured on a detector downstream have got a well defined origin region for all events, which can ease the reconstruction of the event kinematics and improves the detection efficiency eliminating non-reconstructable far-from-axis events. In electron-ion reactions a compressed momentum spread of the ions causes a reduced spread of relative electron-ion velocities, which enhances the energy resolution of such an experiment. The third advantage of a compressed beam is its higher luminosity resulting in an enhanced probability of interaction with a projectile particle along the interaction track in a merged beam geometry. And last but not least, the lifetime of a cooled beam is longer since a beam position closer to the ideal orbit of a storage ring is less sensitive to optics aberrations and the cooling force counterbalances the momentum transfer from the rest gas collisions, which otherwise causes scattering and loss of ions, as soon as scattered ions leave stable orbits in the ring. If the storage time is long enough compared to the radiative decay time of internal excitations, the stored ions can reach vibrational and rotational levels close to the ground state (if not re-excited) which simplifies the analysis of the data and allows to carry out experiments in interstellar medium (ISM) relevant conditions with just a few levels above the ground state being populated. This also helps in the interpretation of experimental data, since it can be compared to calculations for well-defined states. If the storage time exceeds the cooling time, the total intensity of the ion beam can be increased by stacking of multiple sequential ion injections.

Phase space cooling in a storage ring, not limited to certain ion species, can be performed by means of either stochastic or electron cooling. The first method is based on measurement and correction of the beam deflections by a set of pick-up and kicker electrodes along the ion track, while the latter uses merging of velocity matched ($v_{ion} = v_{el}$) cold electron and hot ion beams in a dedicated merged beam section to establish thermal equilibrium between electrons and ions. Electron cooling thus brings the ion temperature close to the electron temperature.

1.2 Magnetic and electrostatic storage rings

Numerous experiments on dissociative recombination (DR), electron impact ionization (EII), dielectronic recombination (DiR) of diverse ion species were carried out at the Test Storage Ring (TSR) in Heidelberg using electron beam devices for the phase space cooling as well as an electron target for collision experiments (non exhaustive list of DR experiments: $^4\text{He}_2^+$ [10], CF^+ [11], H_3^+ [12], D_3O^+ [13], DCO^+ [14], DCND^+ [15], HF^+ [16]; EII: Mg^{7+} [17], Fe^{11+} [18]; recent examples for DiR: W^{20+} [19], Fe^{16+} [20], $\text{Fe}^{10/11+}$ [21]).

Today the astrochemistry community is requesting more experiments on *heavy* molecular ions. The TSR being a magnetic storage ring has a mass limit for a singly charged ion of a given energy to be stored. This limit is dictated by the maximum acceptable rigidity of an ion beam given by the maximum ring bending radius r and maximum magnetic field B such that $Br = \sqrt{2M_i E_i}/q$. In case of the TSR the rigidity limit is 1.495 Tm [22], which is close to the limits of other rings of similar type (ASTRID: 1.87 Tm [23], S-LSR: 1 Tm [24], CRYRING: 1.4 Tm [25]). Molecular ions can generally not be produced in a charge state higher than unity without breaking of chemical bonds (while stripping), and also the primary interest of astrochemistry lies in singly charged ions. Hence the only way to store heavy molecular ions in a ring is to lower the energy. At lower energies and for heavier masses the beam velocity reaches the range where the ion lifetime due to interaction with the residual gas is getting short [26] compared to phase space cooling and radiative cooling times. This calls for a vacuum pressure below the Ultra High Vacuum (UHV) limit of 10^{-11} mbar typical for the TSR and other room temperature operated storage devices. For the heaviest ions, electrostatic storage rings are an attractive alternative, since the bending force Eq is independent on ion mass. Thus the velocity of ions stored at a given energy scales as $M_i^{-1/2}$ compared to the M_i^{-1} velocity scaling in a magnetic ring on rigidity limit. Although this gain in stored ion velocity is prominent only for ion masses over 200 a.m.u. (using the TSR rigidity) and it solely does not eliminate the lifetime problem completely.

To address experimental problems on weakly bound negative ions [27] and reach rovibrational ground states of molecular ions there is also a demand for storage devices where the blackbody radiation is kept at levels corresponding to ISM temperatures below 10 K. The solution which allows both to increase the storage time and reduce the infrared radiation background is to operate a storage ring at cryogenic conditions.

Next generation storage ring projects were thus proposed, built and taken into operation during the past decade and are being built, as summarized in Table 1.1.

The Cryogenic Storage Ring (CSR) proposed and presently under construction at the Max Planck Institute for Nuclear Physics (MPIK) in Heidelberg as a successor to the TSR takes a very special place in the row of such storage devices. The CSR is

Table 1.1: Electrostatic rings in service and under construction

	closed orbit, m	Max. energy, keV	operation temp., K	electron cooling	status
CSR, Heidelberg [28]	35.2	300	2-300	yes	under constr.
USR, Darmstadt [29]	43	300	2-300	yes	proposed
DESIREE, Stockholm [30], [31]	9.3	100	5-300	no	under constr.
FLSR, Frankfurt [32]	14.2	50	300	no	in service
TMU E-ring, Tokyo [33]	7.7	30	77	no	in service
KEK, Kyoto [34], [35]	8.1	30	300	yes*	in service
ELISA, Århus [36]	6.3	25	230-300	no	in service
Mini-Ring, Lyon [37]	0.3	4	300	no	in service
New-Ring, Tokyo [T. Azuma priv.]	1	4	4	no	proposed

* observed enhancement of the lifetime without a phase space compression

an entirely cryogenic storage ring, but in contrast to the table-top format typical for electrostatic rings (see Table 1.1) the CSR is designed to have dedicated 2.6-meters long straight sections suitable for large-scale built-in experimental devices. The bigger bending radii and corresponding corner sections are due to the much higher beam energy than used at small electrostatic rings. The CSR features cryogenic operation, extremely high vacuum (XHV) conditions, a set of modular electrostatic ion sources, possibilities for phase-space cooling, merged beam experiments for electron-ion collisions and ion-laser beam interactions, as well as ion-neutral beam experiments in both merged and crossed beam geometries. Being an electrostatic ring the CSR is designed to operate at ion energies much lower than the MeV energies of magnetic rings.

The energy range suitable for proposed experiments and compatible with a compact design of the ring and the source array was found to be 20-300 keV/q. Such energies of the ion beam are at least an order of magnitude lower than used at the TSR and similar storage devices, but they are higher than at practically all electrostatic rings so far. As shown by Danared [38] for the DESIREE storage ring, stochastic cooling is not feasible for such low energies. Due to the low revolution frequency of the beam, the required cooling times exceed the expected ion beam lifetimes for any acceptable ion current of singly charged ions. Thus the only feasible option to provide phase space cooling at the CSR conditions is electron cooling. The electron beam device must be a dual-purpose apparatus providing not only a velocity matched electron beam for phase space cooling, but also a more energetic detuned beam for recombination/ionization experiments with

incident electron energies from a few meV for recombination experiments to as high as ~ 1 keV for impact ionization. Such an electron beam device is being designed in parallel with the ring to become one of its key features. Operating in velocity matched mode $v_i = v_e$ (electron cooling) it should provide an intense electron beam of energy $E_e = E_i(m_e/M_i)$, *which ranges from 163 eV for 300 keV protons to as low as 1 eV for a singly-charged molecular ion of 160 a.m.u. mass.* The lower part of the energy range, below 10 eV, corresponds to most of the interesting heavy ions. These energies are significantly lower than the lowest energies for which electron cooling has been achieved. Implementing of electron cooling at such energies, hereafter denoted as *ultra-low*, is an experimental and technological challenge since high quality electron beams of such energy were not achieved anywhere else before. Crucial properties of the electron beam depend upon external parameters in different ways compared to higher energies. The general CSR design concept puts additional technical constraints on the cooler design.

1.3 Outline of this work

This work is dedicated to development of an electron cooler/target (hereafter referred to as cooler) suitable for operation in the CSR. The development includes experimental studies on ultra-low energy electron beams at the existing TSR electron target, numerical simulations of the cooler magnetic optics, mechanical design and cryogenic test of key components that were developed in this work. The content of the work is organized in the following way. The second chapter gives a more detailed introduction of the CSR, summarizing general design requirements originating from XHV and cryogenic operation. It also provides the basic CSR ion beam properties relevant to the electron cooler design. A short theory background on electron cooling is given at the end of the chapter to highlight which electron beam parameters play the key roles in successful operation of an electron cooler.

The subsequent chapter “Ultra-low energy electron beams” starts with experimental studies on ultra-low energy electron beams aiming to reach maximum density of the electron beam at low energies and to develop a proper calibration technique for the beam kinetic energy. Then values of transverse and longitudinal electron temperatures in the energy range of interest are calculated to serve as an input for the calculation of magnetic field magnitudes required for the electron optics and estimation of cooling times. The electron and ion beam properties are subsequently used to formulate a design specification of the cooler. A magnetic field geometry according to this specification is numerically simulated by means of finite element analysis software, and its performance is evaluated by electron and ion tracking.

The chapter “Realization of the CSR electron cooler” is devoted to practical steps from the field geometry towards construction of the cooler. The chapter starts with an

overview of the general mechanical design concept. The conductor geometry elaborated in the previous chapter is analyzed regarding its optimal realization. A prototype superconducting coil is designed and taken in operation, and a cryogenic cooling system for the magnets is designed and also taken into operation. At the end of this section the results of the joint test of the cooling system and the test magnet are reported. Finally the “Summary and outlook” chapter summarizes the results from earlier chapters and gives an outlook to the further construction stages of the electron cooler.

Chapter 2

An electrostatic storage ring for electron-cooled ion beams

2.1 Overview of the CSR

2.1.1 Geometry and lattice

The CSR is shaped by four 2.6 meters straight sections connected by 90° corners forming a closed orbit of about 35 meters circumference determined by the high ion energy and the size of the straight sections. All the bending and focusing elements are installed in the corner sections and include four focusing quadrupoles, two 6° electrostatic deflectors (which separate charged and neutral products) and two 39° deflectors. The beam is injected in the corner indicated in fig. 2.1 from either a 300 kV electrostatic injector or an alternative 60 kV ion source. The latter can also provide a neutral beam produced by electron photodetachment from singly charged negative ions [39]. The following downstream linear section is dedicated to merged ion-neutral beam experiments. The next are the electron cooler section, followed by a beam diagnostic [40] and a gas jet target [41] section (labeled as “reaction microscope” in fig. 2.1). Beam diagnostics is foreseen in all four straight sections. Everywhere, apart from the electron cooler section, it is based on capacitive beam position monitors. The cooler section instead features mechanical, rotating beam scrapers. In the dedicated beam diagnostics section a Schottky pick-up and current monitor are installed [40]. The primary array of detectors for electron-ion experiments is placed downstream from the cooler and includes counting and fragment imaging detectors. Counting detectors of similar type are foreseen for the other experimental sections as well.

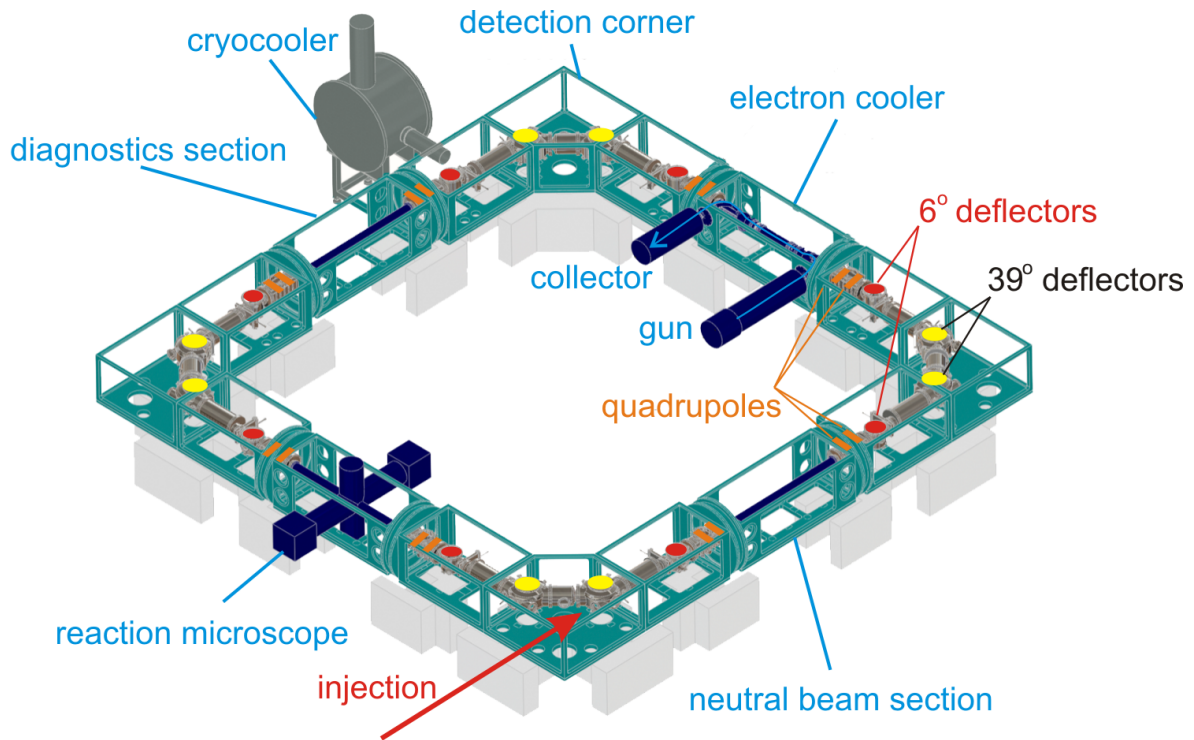


Figure 2.1: The CSR geometry and lattice.

2.1.2 The lifetime of slow ions, vacuum conditions and cryogenic operation

As mentioned above the ion beam lifetime limits the mass of stored medium energy ions at a given vacuum pressure. For the storage of negative ions the lifetime is limited by electron loss collisions and for the positive ions the electron capture process plays the key role. As shown by Schlachter et al. [26] the cross-section of electron capture scales with the ion energy per nucleon as $\sim E^{-4.8}$ for $10 < E < 1000$ keV/a.m.u. which makes storage of medium energy ions possible for only few or some tens of seconds [42, 34, 43].

At the same time experiments with molecular ions must give the molecules time to de-excite. While more energetic vibrational excitations have cooling times of less than 100 sec [44], the rotational states are much more long-lived. The corresponding cooling times for homonuclear molecules like H_2 or O_2 can exceed 10^6 sec [44]. For less symmetric heteronuclear molecules these cooling times are shorter, but as shown by Mendes [45] on the example of the simple linear molecule DCND^+ studied at the TSR, rotation states with $J < 4$ can have cooling times exceeding 10^5 seconds. Thus, to achieve rovibrational ground state population one needs to improve the expected lifetime by two orders of magnitude, which for a given energy can be done only by reducing the density of the residual atmosphere. In case of the CSR it means that a vacuum pressure corresponding to 1000 cm^{-3} particles must be achieved. At the room temperature this corresponds to 10^{-13} mbar (XHV). The residual atmosphere at UHV conditions consists mainly of hydrogen outgassed from stainless steel chamber walls

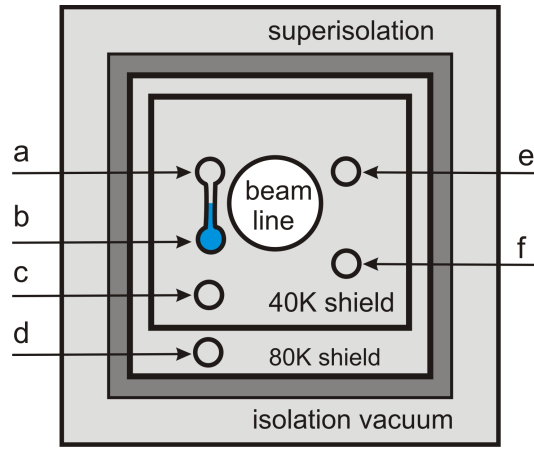


Figure 2.2: Cryogenic concept of the CSR, a) 1.8 K He vapor line (17 mbar), b) superfluid He 1.8 K, c) 40K gas-He, d) 80K gas-He, e) 5K gas He 1-st turn, f) 5K gas-He 2-nd turn.

and structures. To surpass the UHV limit of 10^{-11} mbar hydrogen must be effectively removed. In cryogenic operation hydrogen can be pumped by cryo-adsorption or cryo-condensation. The former works at higher temperatures, but its capacity is limited by a monolayer coverage of the adsorbate. The latter provides higher speed and unlimited pumping capacity, but needs a surface at a temperature below vapor saturation at a given pressure. This temperature for hydrogen at XHV pressure is about 1.8 K [46].

The cryogenic concept of the CSR thus includes 1.8 K pumping units supplied with superfluid liquid helium (LHe) uniformly distributed in the ring (5 units per corner plus 2 in the cooler section to prevent a local pressure bump [47]). To assist pumping of other gases, suppress the blackbody radiation and reduce outgassing of the chamber walls the beam line will be cooled to the 10 K temperature. The cryogenic/vacuum concept has been successfully tested on a big scale 3-m long electrostatic Cryogenic Trap for Fast ions (CTF) built in 2007-2008 as a benchmark for the CSR. As a proxy of the vacuum pressure in the XHV range, the collision-induced loss rate of N_2^+ ions has been measured, demonstrating a $1/e$ lifetime of 340 seconds at 14 keV, which corresponds to a residual gas density of $2 \pm 1 \times 10^3 \text{ cm}^{-3}$ ($8 \pm 4 \times 10^{-14}$ mbar) [48].

2.1.3 Room temperature operation

According to the experimental program, to address experiments at the intermediate temperatures from cryogenic to the room temperature the CSR must also be able to function in an operation mode when the beam line and shields are not actively cooled to cryogenic temperatures by the helium lines. In this room temperature (RT) mode of operation UHV conditions can be provided by pumping based only on non-evaporative getter (NEG) modules, charcoal-covered bakeable cryopumps and differential pumping of outer connections by means of ion-getter pumps [49]. To enable RT operation the beam line must be baked at up to 220-350° C to reduce outgassing and activate the NEG modules. All in-vacuum equipment must either be able to survive the bakeout

or be easily removable. In the RT operation the 40 K and 80 K cooling lines are unavailable and only limited cooling power can be provided by two loops of the 5 K line (see fig. 2.2), with the second loop temperature varying from 5 to 80 K depending on position in the cooling circuit. Thus for cryogenically operated parts producing significant load due to heat emission or heat leaks (such as magnets) an independent cooling system must be foreseen.

2.2 Phase space cooling

The subject of this work is the realization of electron cooling (a special case of phase space cooling) aiming to improve and extend experimental performance of the CSR. It is worth to start with a short introduction of some ion beam parameters such as emittance and temperature for the CSR.

In the 2-dimensional phase space of the particle coordinate q and its momentum p , an ion beam can be represented as an area or a curve enclosing the p and q coordinates of every particle in the beam. Liouville's theorem states that in the absence of friction forces the shape and position of the enclosing curve can be changed (by focusing or shifting of the beam), but the enclosed area is an invariant so that $\int pdq = \text{const.}$

In a storage ring the transverse beam dynamics is governed by Hill's equation

$$\frac{d^2x}{ds^2} + k(s)x = 0 \quad (2.1)$$

where x denotes one of the transverse coordinates, s is the longitudinal coordinate, and $k(s)$ is a periodic function of the ring lattice period of L representing the ring periodic field so $k(s+L) = k(s)$. This equation can be represented in Courant-Snyder parametrization [50] for the transverse coordinate x and its divergence $x' = dx/ds$ as

$$\gamma(s)x(s)^2 + 2\alpha x(s)x'(s) + \beta(s)x'(s)^2 = \frac{\varepsilon_x}{\pi} \quad (2.2)$$

where $\beta(s)$ is the beta function, $\alpha(s) = -d\beta(s)/ds$ and $\gamma(s) = (1+\alpha^2)/\beta$. The equation describes an ellipse in coordinates x and x' and its surface ε_x is called emittance, see fig. 2.3.

As a consequence of Liouville's theorem the emittance ε_x is a constant. The r.m.s. size of the beam and its divergence depend on the emittance as

$$\sigma_x = \frac{\sqrt{\beta_x \varepsilon_x}}{2} \quad \sigma'_x = \frac{\sqrt{\gamma_x \varepsilon_x}}{2} \quad (2.3)$$

The maximum beam emittance which still can be stored by a ring is called acceptance. In case of the CSR the acceptance according to the lattice simulations [51] is 120 mm×mrad for the horizontal coordinate and 180 mm×mrad for the vertical direction, with the maximum beam size in the middle of a linear section of ± 4 and ± 1.4 cm for

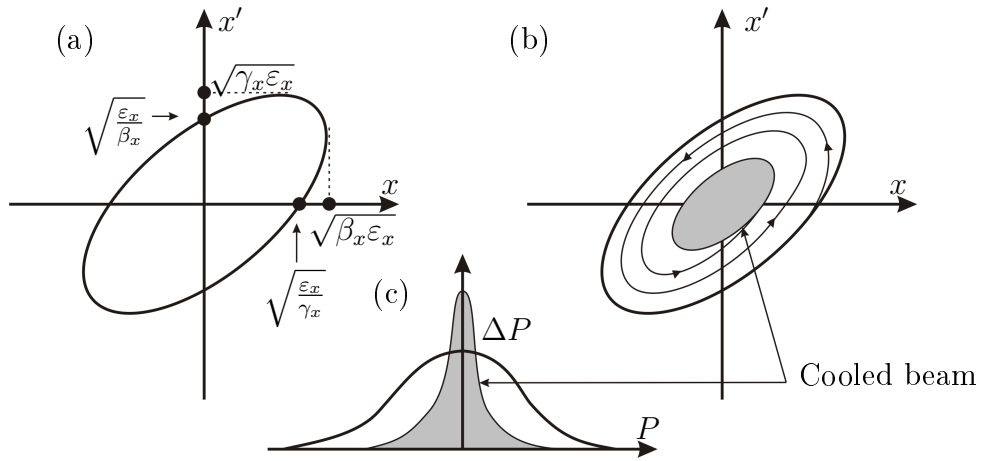


Figure 2.3: The emittance and cooling. (a) The emittance in Courant-Snyder parametrization (b) Beam cooling (c) Reduction of the momentum spread as a result of cooling process.

the horizontal and vertical coordinate, respectively. Examples of phase space ellipses of the maximum size at a position in the center of the straight section are shown on the left of fig. 2.4. The β -function, describing the variation of the ellipse parameters along the ion trajectory in the ring, is given in fig. 2.4 on the right.

If we consider an ion beam stored on a closed orbit in the ring at average velocity v_0 (hereafter we will consider all ion beams as non-relativistic, since even for 300 keV protons the ion velocity is only 2.5×10^{-2} times the speed of light) in an orthogonal reference frame co-moving along the closed orbit, the relative velocity of each individual ion can be expressed as the sum of a longitudinal and a transverse component (see fig. 2.5b) such that:

$$\vec{v}_i = v_{\parallel} \vec{u}_{\parallel} + v_{\perp} \vec{u}_{\perp}, \quad (2.4)$$

$$\vec{v}_i = v_x \vec{i} + v_y \vec{j} + v_s \vec{k} \quad (v_s = v_{\parallel}), \quad (2.5)$$

where the index \parallel denotes the axis parallel to \vec{v}_0 in this point of the trajectory and \perp refers to the plane perpendicular to \vec{v}_0 . We can then introduce *the ion beam temperatures in the rest frame* such that

$$k_B T_{\perp} = \left\langle \frac{1}{2} M_i v_{i\perp}^2 \right\rangle \quad (2.6)$$

where k_B is the Boltzmann constant, M_i the mass of the ion and $v_{i\perp}$ the perpendicular ion velocity in the beam frame. Brackets mean the averaging over the ion velocities. This defines the transverse ion beam temperature as

$$k_B T_{\perp} = \frac{1}{2} M_i \langle v_{i\perp}^2 \rangle = \frac{1}{2} M_i v_{i\parallel}^2 (\sigma_{x'}^2 + \sigma_{y'}^2) = \frac{1}{8} M_i v_{i\parallel} (\gamma_x \varepsilon_x + \gamma_y \varepsilon_y). \quad (2.7)$$

Similar for the longitudinal momentum spread,

$$\frac{1}{2} k_B T_{\parallel} = \frac{1}{2} M_i \langle v_{i\parallel}^2 \rangle \quad (2.8)$$

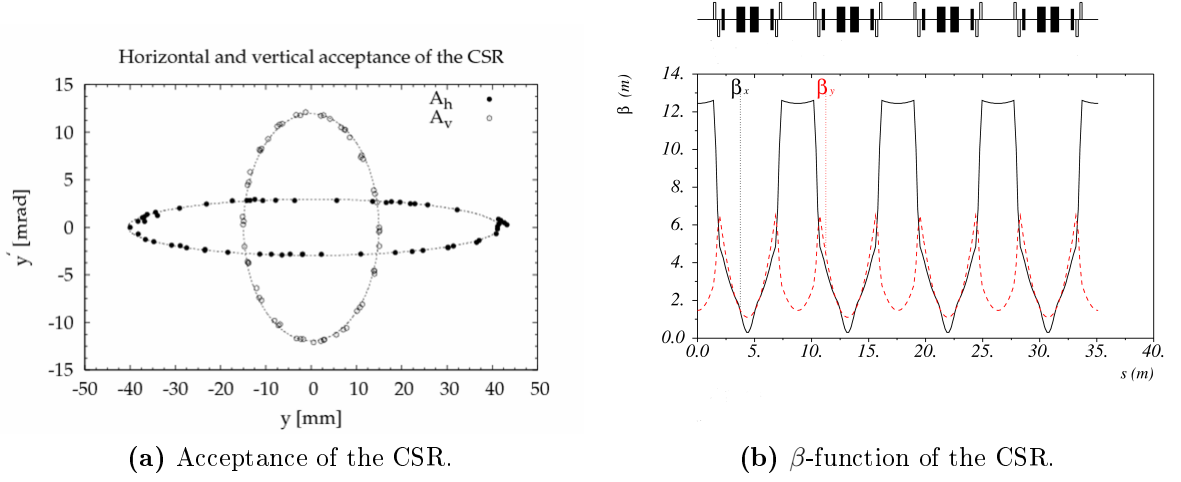


Figure 2.4: The acceptance of the CSR (left) and the β -function of the lattice (right) [51].

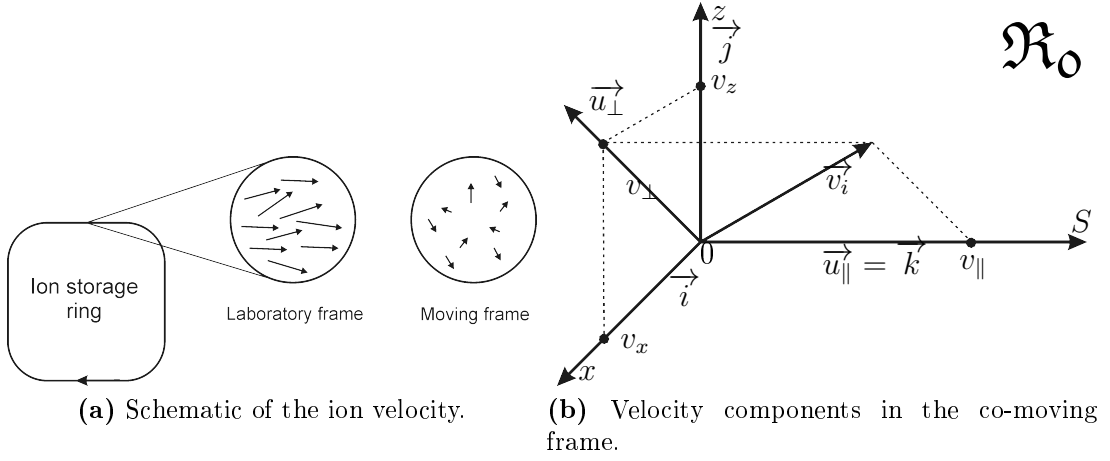


Figure 2.5: Ion velocities in the co-moving frame.

where $v_{i\parallel}$ is the longitudinal ion velocity in the beam frame. The specification of the CSR assumes the energy spread of stored ions of about 10^{-4} of the set ion energy. Thus for a typical ion energy of $E_{ion} = 300$ keV the energy spread for a singly charged ion is $\Delta E_{in} = 30$ eV. Changing to the co-moving frame the energy spread ΔE_{cm} is

$$\Delta E = \left. \frac{\partial E}{\partial v} \right|_{v_{\parallel}} \Delta v \rightarrow \Delta E_{cm} = \frac{m}{2} (\Delta v)^2 = \frac{(\Delta E_{in})^2}{4E_{ion}} \quad (2.9)$$

for a 300 keV ion one gets a longitudinal temperature of 0.75 meV in the comoving frame independent on the ion mass. Using eq. 2.7, the acceptance and β -function values of the CSR ($\varepsilon_{x/y} = 1.2/1.8 \times 10^{-4}$ m, $\beta_{x/y} = 12.1/1.3$ m, for the middle of the linear section $\alpha(s) = 0 \rightarrow \gamma(s) = \frac{1}{\beta}$) one can also get the transverse ion temperature estimate as

$$k_B T_{\perp} = \frac{1}{8} M_i v_{i\parallel}^2 \left(\frac{\varepsilon_x}{\beta_x} + \frac{\varepsilon_y}{\beta_y} \right) \approx 3.7 \times 10^{-5} E_{ion} \quad (2.10)$$

Which for an ion energy of 300 keV gives 11.1 eV or about 1.3×10^5 K.

Generally in storage rings there are several processes, such as collisions with rest gas molecules, which violate the assumptions of Liouville's theorem, so that the phase space volume is not preserved and the beam emittance grows. To improve both the experimental resolution and the beam lifetime one needs to introduce a friction force, which acts in a way to compress the occupied phase space. As these forces reduce the momentum spread of the ions (i.e. temperature) hereafter they are referred to as cooling forces. A cooling force acting on the ion beam counterbalances the heating processes related to the beam environment such as rest gas collisions, caused by mutual scattering of the ions in the beam itself, or introduced by experiments with an internal gas target, when the ions are scattered in the collisions with neutral atoms injected as a gas jet. After compression of the beam phase space additional particles can be injected into the storage ring. As a result of this stacking process after some repetitions of injection and cooling cycles the overall beam intensity can be significantly increased. Thus the presence of an adequate cooling force allows to maintain and in cases of stacking even increase the intensity of the ion beam simultaneously improving the beam quality. This makes it possible to address experimental problems otherwise unavailable without cooling of the ion beams due to fast ion losses or unacceptably low count rate. The cooling forces can be of various origins. As mentioned before the stochastic cooling used in high energy accelerators is not feasible at the CSR energy and current range. Thus the only option is electron cooling.

2.3 Electron cooling

The idea of electron cooling was proposed by G. I. Budker in 1966 [52] and first demonstrated at the NAP-M ring at BINP in 1974 [53]. The principle of electron cooling is based on embedding a hot ion beam in a cold (in the comoving frame) electron beam over a certain distance. A typical layout of an electron cooler is shown in fig. 2.6.

The electrons are produced continuously by a cathode. Then they are accelerated to match the velocity of the ion beam. The velocity matched electron beam is merged

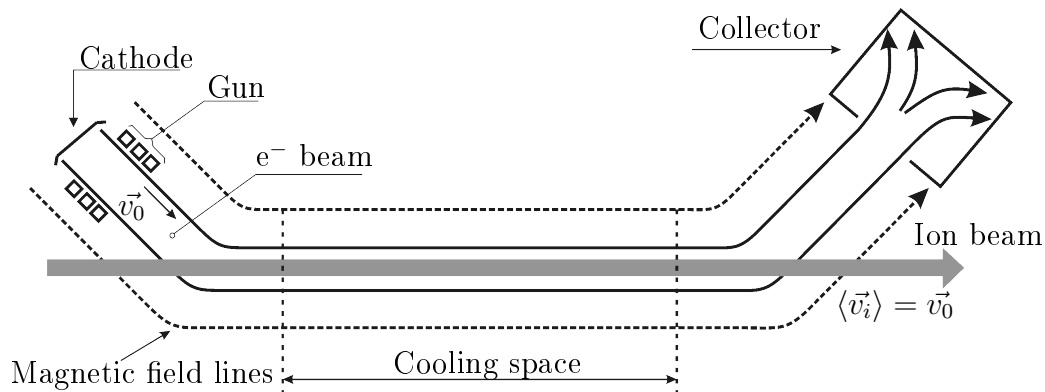


Figure 2.6: Principle of electron cooling. The magnetic field lines schematically show near-homogenic magnetic field that guides the electron beam from the cathode to the collector.

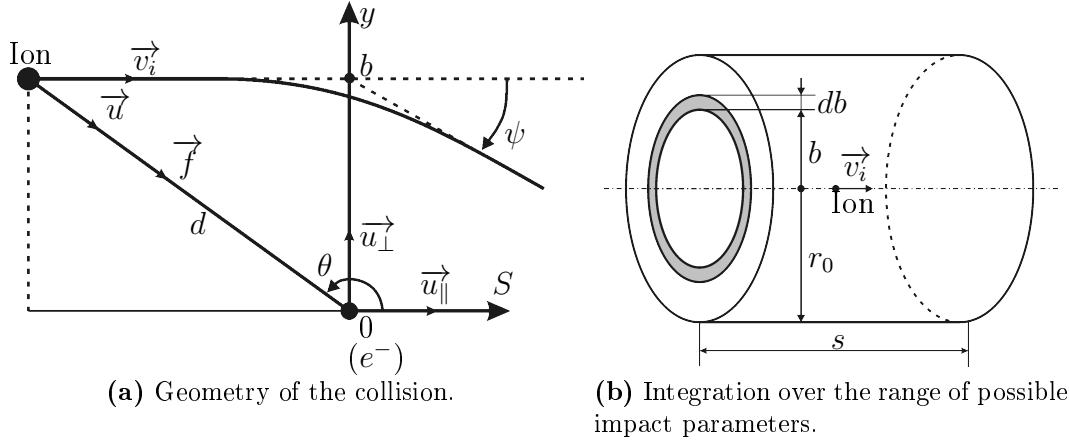


Figure 2.7: Geometry of the collision.

with the ion beam over the length of the interaction region. At the end of this section the electron beam is steered away and dumped in a collector.

In the interaction region two groups of charged particles with temperatures T_{ion} and T_{el} are mixed. Due to Coulomb interaction, the fact that the electron density is much higher than the ion density, and because at each revolution the ion beam interacts with a new cold bunch of electrons, the ion temperature must approach the electron temperature.

If we will now take into account the fact that the electrons and ions are characterized by not only a single temperature, but by momentum distributions asymmetric for transverse and longitudinal degrees of freedom, the cooling process is also asymmetric and depends upon relations of electron and ion energy distributions between each other. The interaction of the electron and ion beam can be considered in a so-called *binary collision model*, where an ion is assumed to experience a single collision with an individual electron and then this interaction is averaged over all possible impact parameters and relative velocities relevant for the experimental conditions. A detailed description of the model can be found in [54]. Let us consider a single ion at velocity v_i in the electron rest frame \mathfrak{R}_0 . For an exponential decrease of the ion velocity we can write

$$v_i(t) = v_{i,0} \exp(-t/\tau_{v_i}) \quad (2.11)$$

where $v_{i,0} = v_i(t=0)$. Then the 1/e cooling time τ_{v_i} is given by

$$\frac{1}{\tau_{v_i}} = -\frac{1}{v_i} \frac{dv_i}{dt} = -\frac{1}{m_i \cdot v_i} \left(m_i \frac{dv_i}{dt} \right) = -\frac{F(v_i)}{p_i} \quad (2.12)$$

where $F(v_i)$ is the cooling force and p_i the ion momentum in \mathfrak{R}_0 . In the case of exponential decrease as in eq. 2.11 $F(v_i)$ is proportional to v_i . To understand the nature of the cooling force let us first consider a binary electron-ion interaction in the absence of a magnetic field, shown in fig. 2.7a.

The ion in a charge state Z initially at position $(-\infty, b)$ with velocity $\vec{v}_i = v_i \cdot \vec{u}_{\parallel}$ will interact with an electron at rest at $(0,0)$. The Coulomb force \vec{f} between the electron and the ion will induce a change in momentum given by

$$\vec{f} = \frac{d\vec{p}}{dt} = \frac{Ze^2}{4\pi\epsilon_0} \cdot \frac{1}{d^2} \vec{u} \quad (2.13)$$

The total change in momentum is then the integral of eq. 2.13 from $-\infty$ to $+\infty$:

$$\Delta\vec{p} = \int_{-\infty}^{+\infty} \vec{f} dt = \frac{Ze^2}{4\pi\epsilon_0} \int_{-\infty}^{+\infty} \frac{\vec{u}}{s^2 + b^2} dt = \Delta p_{\parallel} \vec{u}_{\parallel} + \Delta p_{\perp} \vec{u}_{\perp} \quad (2.14)$$

where

$$\vec{u} = \frac{\vec{f}}{|\vec{f}|} = -\cos\theta \cdot \vec{u}_{\parallel} - \sin\theta \cdot \vec{u}_{\perp} = \frac{-s}{\sqrt{s^2 + b^2}} \vec{u}_{\parallel} + \frac{-b}{\sqrt{s^2 + b^2}} \vec{u}_{\perp} \quad (2.15)$$

For small-angle scattering Δp_{\parallel} vanishes because the longitudinal component of the force is an odd function and is integrated over a symmetric range. For the transverse component we get

$$\Delta p_{\perp} = \frac{-Ze^2 b}{4\pi\epsilon_0} \int_{-\infty}^{+\infty} \frac{dt}{(s^2 + b^2)^{3/2}} \quad (2.16)$$

and since $s = v_i t$

$$\Delta p_{\perp} = \frac{-Ze^2 b}{4\pi\epsilon_0 v_i b^2} \lim_{s \rightarrow \infty} \left[\frac{s}{\sqrt{s^2 + b^2}} + \frac{s}{\sqrt{s^2 + b^2}} \right] = \frac{-2Ze^2}{4\pi\epsilon_0 v_i b} \quad (2.17)$$

Due to the conservation of momentum the momentum change of the electron is $\Delta\vec{p}_e = -\Delta\vec{p}_i$ and the energy gained by the electron (and lost by the ion) is

$$\Delta E(b) = \frac{(\Delta p_i)^2}{2m_e} = \frac{-Z^2 e^4}{(4\pi\epsilon_0)^2 v_i^2 b^2} \quad (2.18)$$

Now we take into account multiple collisions with all possible impact parameters b . If n_e is the electron beam density then the number of electrons in the volume $\pi b^2 ds$ is $n = \pi b^2 n_e ds$ while $dn = 2\pi b n_e ds db$ is the number of electrons between b and $b + db$ over the length ds (see fig. 2.7b).

The energy loss per unit interaction length is then:

$$\frac{dE}{ds} = 2\pi \int_{b_{min}}^{b_{max}} b n_e \Delta E(b) db = \frac{Z^2 e^4}{4\pi\epsilon_0^2 m_e v_i^2} n_e \ln \left(\frac{b_{max}}{b_{min}} \right) \quad (2.19)$$

The latter term $\ln(b_{max}/b_{min})$ is the so called Coulomb Logarithm L_C which limits the range, over which the Coulomb interaction is integrated, which otherwise, for the infinite range, would be non convergent. b_{min} can be estimated by the maximum

momentum transfer to the electron (classical head-on collision):

$$\frac{2Ze^2}{4\pi\epsilon_0 v_i b_{min}} = \Delta p_{max} = 2m_e v_i \rightarrow b_{min} = \frac{Ze^2}{4\pi\epsilon_0 m_e v_i^2} \quad (2.20)$$

For b_{max} we take $b_{max} = \min(\lambda_D, r_0)$ where r_0 is the beam radius and λ_D is the Debye screening radius. An ion embedded in the electron cloud will cause rearrangement of electrons in the way to shield the ion electric field. The field magnitude then decreases exponentially with the electron-ion distance with a decay constant called the Debye length λ_D

$$\frac{1}{\lambda_D^2} = \frac{e^2}{\epsilon_0 k_B} \left[\frac{n_e}{T_e} + \frac{n_i Z^2}{T_i} \right] \quad (2.21)$$

where k_B is the Boltzmann constant, and n_e , n_i and T_e , T_i are the electron and ion densities and temperatures, respectively. Due to both higher electron density and lower temperature the electron term dominates (details on electron beam properties are discussed in the following chapter):

$$\lambda_D \approx \sqrt{\frac{\epsilon_0 k_B T_e}{n_e e^2}} \quad (2.22)$$

Depending on the ion mass and hence the density of a velocity-matched electron beam the Debye length is about $10^{-4} - 10^{-3}$ meters, which is much smaller than the electron beam radius and hence should be taken as b_{max} .

The next step towards a realistic picture is to take into account that the electrons have non-zero temperature and hence a velocity spread. It is worth to mention that most of the cooling experiments take advantage of magnetized electrons. In a strong enough magnetic field transverse and longitudinal motions of electrons in the beam can be thought as completely decoupled, treated independently and each of them is characterized by its own temperature [54]. Due to the same kinematic reason as for the ion beam, the longitudinal electron temperature is typically much lower than the transverse, and the guiding magnetic field keeps them from equalization such that $T_{e\perp} > T_{e\parallel}$. If we thus introduce the electron velocity distribution as

$$f(v_e) = \frac{e^{-\left[\frac{v_{e\parallel}^2}{2\Delta_{e\parallel}^2} + \frac{v_{e\perp}^2}{2\Delta_{e\perp}^2}\right]}}{(2\pi)^{3/2} \Delta_{e\parallel} \Delta_{e\perp}^2}; 1 = \int f(v_e) d^3 v_e \quad (2.23)$$

$$\text{where } \Delta_{e\parallel}^2 = \frac{k_B T_{e\parallel}}{m_e}; \Delta_{e\perp}^2 = \frac{k_B T_{e\perp}}{m_e} \quad (2.24)$$

Then the cooling force is

$$\vec{F} = -\frac{Z^2 e^4 n_e}{4\pi \epsilon_0^2 m_e} \int L_C \frac{\vec{v}_i - \vec{v}_e}{|\vec{v}_i - \vec{v}_e|^3} f(v_e) d^3 v_e. \quad (2.25)$$

This is the exact equation to calculate the cooling force but it is too general to be applied analytically and requires some ground assumptions and simplifications to be made. As we qualitatively see from eq. 2.25 the cooling force depends upon the ratio of electron and ion velocity spreads, which defines the asymptotic shape of the force. For the quantitative characteristic the electron density is a crucial parameter. The electron current density is limited by the space charge effects at the gun and interaction regions so that the electron current depends on voltage as $I = pU^{\frac{3}{2}}$ [55] where p is a constant for a given gun geometry. The longitudinal electron temperature presented in equation 2.25 is a function of both electron density and kinetic energy of the beam. As mentioned before the electron cooler of the CSR is mainly aimed to operate at the electron energy range below 10 eV. This creates a set of conditions very uncommon for an electron cooling device. Since its introduction in 1970s the electron cooling physics and design aspects were carefully studied and a lot of experience was gathered through this period. But as one can see in fig. 2.8 the focus was kept on the 1-100 keV region. Apart from this main stream, electron cooling at energies down to 158 eV was reported at CRYRING [56]. A few results are also reported on the observed ion lifetime enhancement in the presence of a velocity matched electron beam. Although the compression of the beam phase space was not reported, these experiments succeeded to achieve measurable effects on the ion beam lifetime. At the KEK electrostatic ring in experiments on 20 keV protons their lifetime was enhanced by a factor of two at the electron energy of 10.9 eV [35]. In experiments at CRYRING [57] on C_2H_2^+ at 77 eV and water clusters $\text{H}(\text{H}_2\text{O})_4^+$ at 11 eV marginal effects on the lifetime have been reported. After commissioning of the new electron target in 2004 [58] the biggest advance in the low cooling energy range was done in experiments at the TSR.

The TSR is a unique machine because it is equipped with two electron cooling devices. The first one built-in from the very beginning is based on a thermocathode electron source and takes advantages of high electron current at medium and high energies, the second one installed in 2004 features a cryogenic photocathode electron source providing the world best resolution in recombination experiments especially valuable at low energies. Both devices can be and were used as either electron cooler or an internal electron target for recombination experiments. To avoid confusion, hereafter, in accordance with its main utilization, the high resolution photocathode device will be referred to as the electron target of the TSR or, shortened, e-target.

The electron target of the TSR so far came closest to the ultra-low cooling energy range. Working on the limit of both the ring and the e-target, efficient phase space compression was demonstrated for CF^+ at 53 eV [11], DCND^+ at 44 eV [59], HS^+ at 47 eV and D_2Cl^+ at 34 eV. The TSR electron target is thus a suitable workbench to produce and study ultra-low energy electron beams to find out actual beam parameters such as n_e , $T_{e\perp}$, $T_{e\parallel}$. The beam characteristics of the TSR e-target can be without loss of generality applied to the CSR, because the key feature of the e-target, its photocathode

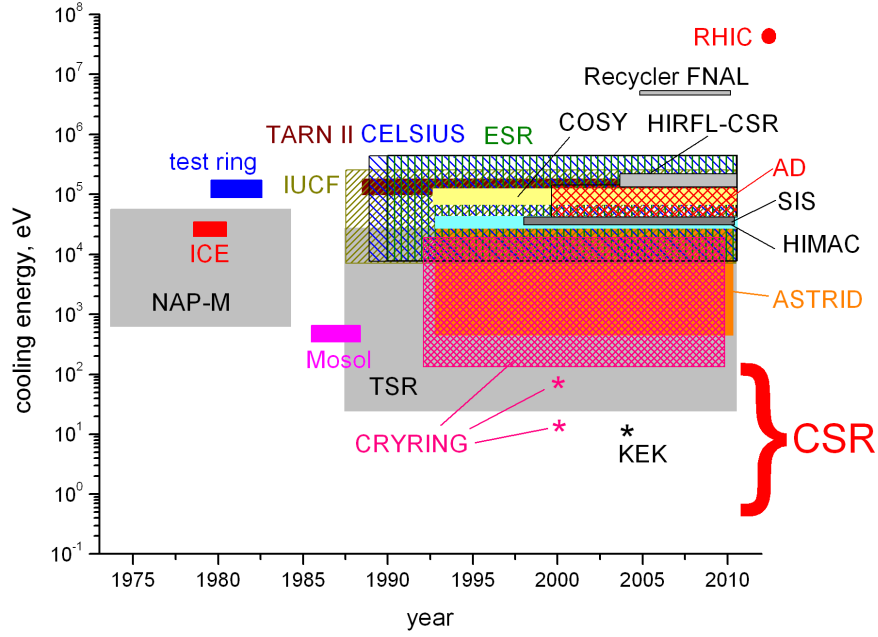


Figure 2.8: Development of the electron cooling technology [11, 59, 56, 60, 25, 57, 61, 35]. The stars show the early attempts of electron cooling at the very low energies, which demonstrated enhancement of the ion beam lifetime, but the phase space compression was not monitored.

based cryogenic electron source, will be transferred to the CSR.

As described in the following chapter, the TSR e-target was used to perform experimental studies on ultra-low energy electron beams. Using the photocathode electron source an ultra-low energy electron beam of high density was successfully achieved. Applying the beam deceleration technique the electron density was enhanced by an order of magnitude. This beam density together with available data on the cryogenic electron source were used later to estimate the performance of the future CSR cooler, find out its limits and develop a design concept suitable for the CSR application.

Chapter 3

Ultra-low energy electron beams

In this chapter we will establish the basic properties of ultra-low energy electron beams in the new regime required by the CSR. In particular, the achievable density and temperatures are crucial for the cooler performance under these advanced conditions. The biggest advance towards the ultra-low energy region is realized by experiments with the TSR e-target, whose electron source will be transferred to the CSR. Successful operation of the TSR e-target at low energies and its potential for the CSR is associated with its cryogenic photocathode-based electron source. This source provides an electron beam with initial electron energy spread an order of magnitude lower than that of thermocathode sources, which dramatically improves the cooling performance. This chapter starts with an account of this electron source and electron gun and then describes the steps realized to generate dense ultra-low energy electron beam with this source.

3.1 Cold electron source

3.1.1 The cryogenic NEA photocathode

The nature of an electron source plays a key role in the temperature related properties of an electron beam since it defines the initial energy spread of emitted electrons. The most common electron gun design features a thermionic electron source, where the temperature of the cathode T and the extractable current density J are connected by Richardson's law of thermionic emission,

$$J = \frac{4\pi m k_B^2 e \lambda_r}{h^3} T^2 e^{-\frac{W}{kT}}, \quad (3.1)$$

where λ_r is a material-dependent constant of the order of unity, h is Planck's constant and W is the material's work function. Thus for a thermocathode the initial energy spread of electrons corresponds to the temperature of the hot cathode filament heated to 1300-1800 K. In the 1980-s different groups proposed to use photocathodes as al-

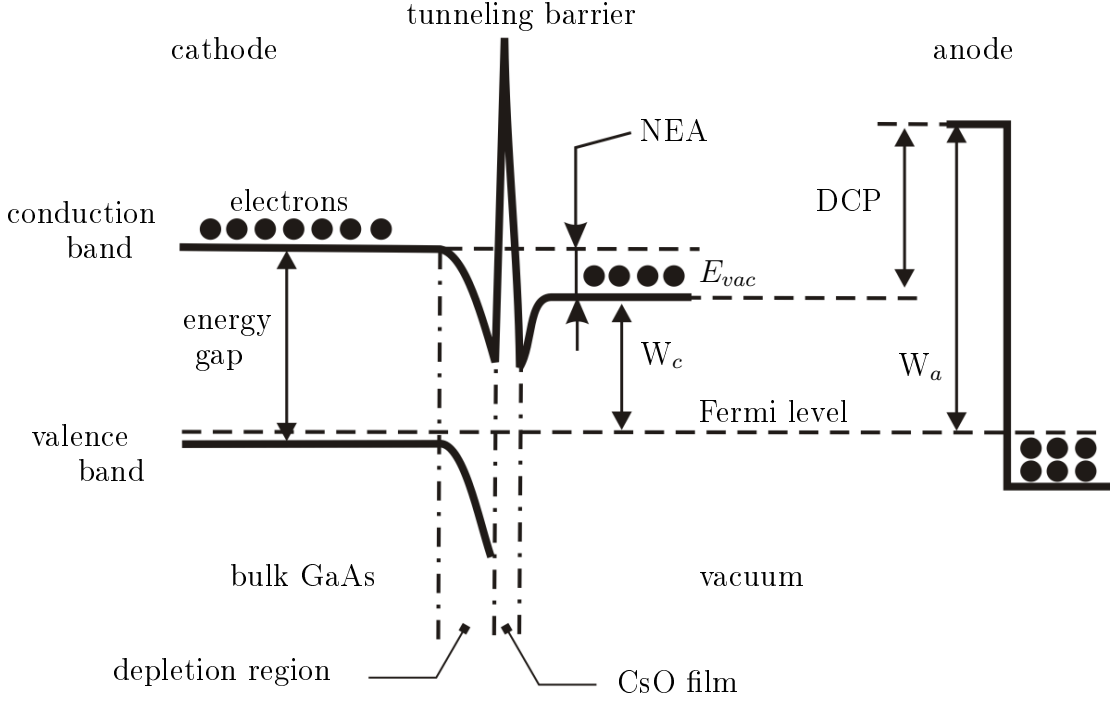


Figure 3.1: Band diagram of a CsO coated GaAs surface-vacuum interface with NEA. W_c - cathode work function, W_a - anode work function, DCP - difference of contact potentials.

ternative sources whose current does not depend upon their temperature [62, 63]. The main limitation for the photocathodes was their relatively low efficiency and need for powerful UV light sources. To escape into vacuum from a cathode an electron must have an energy exceeding the material work function, which for metals is typically 4.5-5.5 eV. However there is a very special case of photocathodes based on heavily p-doped direct-band III-V semiconductor crystals (GaAs, InP, $\text{In}_x\text{Ga}_{1-x}\text{P}$) with monolayer-thin coverage of Cs and O. First discovered by Scheer and van Laar in 1965 [64] such photocathodes achieve a state of effective negative electron affinity (NEA) where electrons, photoexcited to the conduction band in the crystal bulk, have energies E_c higher than the potential energy of an electron in the vacuum close to the crystal surface E_{vac} (see fig. 3.1). These, electrons can drift towards the crystal surface and then escape into the vacuum by tunneling through a thin potential barrier on the crystal/vacuum interface. Comprehensive theory of NEA-photocathodes together with experimental data on their performance are given in [65].

State-of-the-art NEA photocathodes have a quantum yield (QY, the ratio of emitted electrons to the number of incident photons) up to 0.3-0.4 and work under visible light, near infrared or near UV illumination, depending on the band gap of the chosen material. The first proposals for the electron cooling application [63] of liquid nitrogen cooled NEA-photocathodes expected longitudinal temperatures of about 6 meV (which corresponds to electrons thermalized down to the crystal temperature) and transverse temperatures of about 1 meV, by taking advantage of electron refraction at

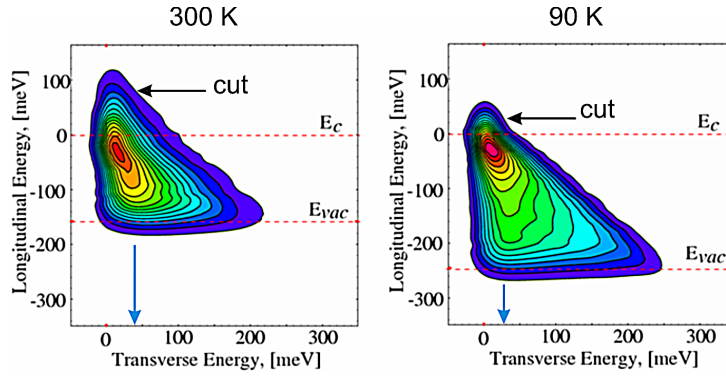


Figure 3.2: Two-dimensional energy distribution of electrons as a function of longitudinal (E_{\parallel}) and transverse (E_{\perp}) energies measured at the temperatures of 300 K and 90 K [67]. E_c is the bottom of the conduction band in the bulk crystal and E_{vac} is the zero potential energy in vacuum close to the surface of the cathode. The black arrows “cut” show the position of the extraction potential barrier, which allows to reach low transverse electron energy as shown by the blue arrows. The pictures are courtesy of D. Orlov.

the crystal/vacuum interface [65]. The latter turned out to be not possible for practical cathodes with some square millimeters of emitting surface due to local surface roughness [66]. As shown by measurements at the test setup during the commissioning stage of the TSR e-target the energy distribution of electrons emitted from a NEA-GaAs photocathode in both longitudinal and transverse directions can be characterized by temperatures close to the cathode temperature for the fraction of the electrons which did not suffer inelastic scattering [67]. As we see in fig. 3.2, the main part of the energy distribution was measured [67] to have the width of the NEA value $NEA = E_c - E_{vac}$, since inelastic scattering of the emitted electrons occurs in the band-bending region near the surface of the crystal. But there is a significant Boltzmann-like distribution of electrons above the conduction band position in the bulk crystal E_c . If only this part is cut of the energy distribution by setting a proper extraction potential barrier as shown in figure 3.2 by the black arrows labeled “cut”, then the transverse energy of the electrons in the beam is limited to the values close to the thermal energy of the electrons in the bulk crystal as it is shown in fig. 3.2 by the blue arrows. Emission from this part of the distribution can provide a cold electron beam with temperatures about 10 meV and an effective QY of 2–3% at 90 K cathode temperature [68, 59, 69, 67, 70].

3.1.2 The electron gun

The photocathode is being used in a specially designed gun [68, 59, 69] of Pierce geometry with 3 electrodes (extraction, Pierce and acceleration) in front of the cathode (see fig. 3.3). The cathode can be illuminated by laser beams either in transmission (wavelength 808 nm) or reflection (532 nm) mode. In both cases the emitting surface forming the beam is limited by a round $\varnothing 3$ mm opening in the Pierce electrode. To lower the temperature of emitted electrons the photocathode is cooled by a nitrogen vapor cooling line. The cathode is usually cooled to a temperature of about 100-150 K

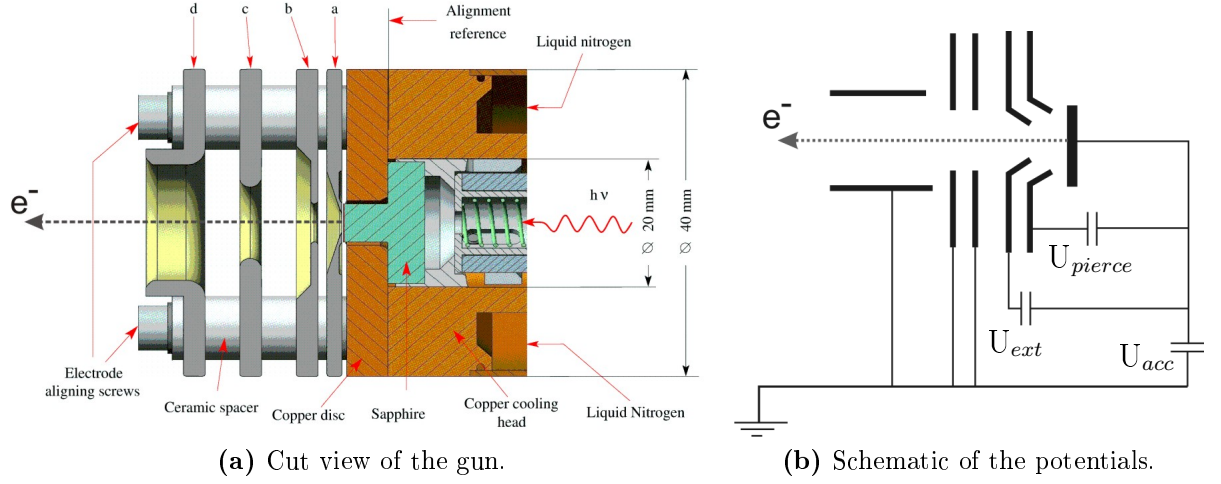


Figure 3.3: Schematic of the TSR GaAs photocathode gun [68], a - Pierce electrode, b - extraction electrode U_{ext} , c, d - acceleration electrodes, placed at the distance 2.4, 10.0 and 17.6 mm from Pierce electrode. In the ultra-low energy experiments electrodes c and d are at ground potential, the extraction b is set to U_{ext} 2.2-11 V depending on extracted current ($2 \times 10^{-11} - 1.3 \times 10^{-5}$ A), Pierce electrode a is set to U_{pierce} 2.51 V, U_{acc} is set to 20 V.

to avoid fast cathode degradation due to cryoadsorption on its surface at lower temperatures [59]. In most of our measurements reported later in this section the temperature has been set to 240 K because of reparation works in the cooling line. The electron gun is immersed in a guiding magnetic field of 8000 Gauss. After extraction from the photocathode by an extraction voltage set relative to the cathode, the electrons are accelerated to a chosen energy by a set of adiabatic acceleration electrodes and undergo magnetic expansion in a region where the guiding magnetic field is reduced to about 400 Gauss in order to lower the transverse temperature. The process of magnetic expansion is described in the following section.

3.1.3 Transverse temperature and adiabatic magnetic expansion

If we consider an electron emitted into vacuum at velocity \vec{v} from a source embedded in a magnetic field \vec{B} then we can show that the magnetic moment $\mu = r_L^2 e \omega_c / 2 = m v_\perp^2 / 2B$ is an invariant in a slowly changing magnetic field. Here $r_L = v_\perp m_e / eB$ is the Larmor radius, v_\perp is the velocity component perpendicular to the magnetic field B and ω_c is the cyclotron frequency. Following Spitzer [71], to prove this statement we need to consider the magnetic field with axial symmetry and an electron rotating around the axis at the Larmor radius r_L .

$$\nabla \vec{B} = 0 \quad \text{gives} \quad \frac{1}{r} \frac{\partial}{\partial r} (r B_r) + \frac{\partial B_z}{\partial z} = 0. \quad (3.2)$$

Assuming $\partial B_z/\partial z$ is constant over the cross section of the particle orbit and equal to $\partial B/\partial z$ one can integrate equation 3.2 over r :

$$\frac{\partial}{\partial r}(rB_r) = -r \frac{\partial B}{\partial z} \Rightarrow B_r = -\frac{1}{2}r \frac{\partial B}{\partial z}, \quad (3.3)$$

where r in the latter expression is equal to the cyclotron motion radius of the electron r_L . Then the component of the Lorentz force acting in z direction is given by

$$m \frac{dv_{\parallel}}{dt} = ev_{\perp} B_r = -\frac{ev_{\perp} r}{2} \frac{\partial B}{\partial z} = \frac{em_e v_{\perp}^2}{2eB} \frac{\partial B}{\partial z} = \mu \frac{\partial B}{\partial z}. \quad (3.4)$$

Multiplying both parts by v_{\parallel} we obtain

$$\frac{d}{dt} \left(\frac{1}{2} m v_{\parallel}^2 \right) = \mu \frac{dB}{dt} \quad (3.5)$$

in the same time from conservation of total energy $\frac{d}{dt}(mv_{\parallel}^2 + mv_{\perp}^2)/2 = 0$ and the definition of μ we get

$$\frac{d}{dt} \left(\frac{1}{2} m v_{\parallel}^2 \right) = -\frac{d}{dt} \left(\frac{1}{2} m v_{\perp}^2 \right) = \mu \frac{dB}{dt} = -\frac{d}{dt}(\mu B) \Rightarrow \frac{d}{dt}\mu = 0. \quad (3.6)$$

Thus the value of μ is not changing along the trajectory. If the electrons are produced at a source embedded in a magnetic field of magnitude B_i with a mean transverse energy E_{\perp}^i and then move along a field gradient to a region with a magnetic field B_f , the final transverse energy will be

$$E_{\perp}^f = E_{\perp}^i \frac{B_f}{B_i} = \frac{E_{\perp}^i}{\alpha}, \quad (3.7)$$

where the ratio of the field magnitudes α is called expansion factor. It gives the factor by which the mean transverse energy will be reduced by transfer it into the longitudinal degree of freedom. This method is called adiabatic expansion since it relies on the condition that the field magnitude changes over a distance long compared to the ‘‘Larmor length’’ $v_{\parallel} m_e / eB$ of the electrons in the beam. Here one should mention that the transverse expansion not only lowers the temperature but also reduces the available electron density in the interaction region, due to the spatial expansion of the beam. If we consider a particle far outside of the symmetry axis at a radial position $R \gg r_L$ the previously obtained result about lowering of the transverse energy will still be true, but the particle will also have an additional drift motion, as long as the guiding magnetic field B has now a radial component given by eq. 3.3, so the drift velocity v_d of the transverse motion will be $v_d = v_z B_r / B_z$, using $dR = v_d dt$

$$dR = -\frac{R}{2B} \frac{\partial B}{\partial z} v_z dt = -\frac{R}{2B} \frac{\partial B}{\partial z} dz = -\frac{R}{2B} dB \quad (3.8)$$

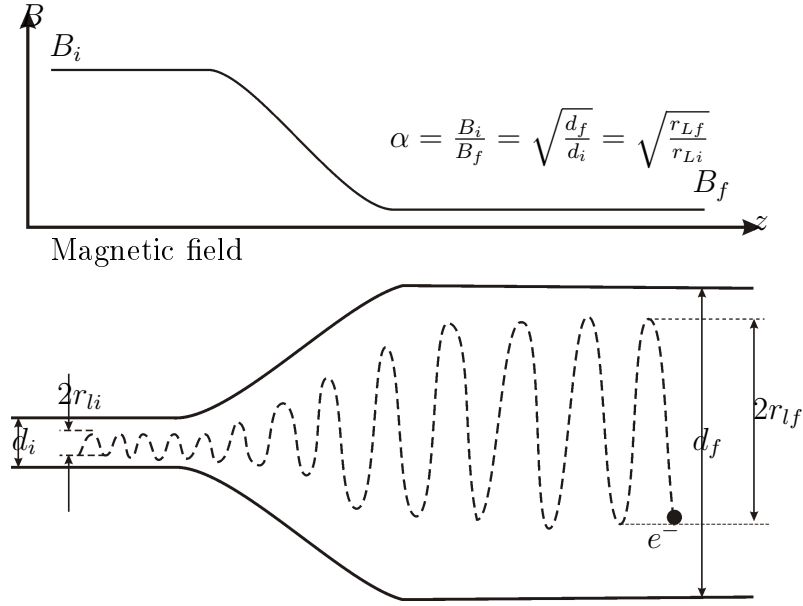


Figure 3.4: Adiabatic transverse expansion of an electron beam

$$\frac{dR}{R} = -\frac{1}{2} \frac{dB}{B} \rightarrow \ln(R)|_{R_i}^{R_f} = -\frac{1}{2} \ln B|_{B_i}^{B_f} \rightarrow R_f = \sqrt{\frac{B_i}{B_f}} R_i = \sqrt{\alpha} R_i \quad (3.9)$$

where index i denotes initial and f final radii and magnetic fields. As we see the final beam radius as well the Larmor radius of an individual electron expand as a square root of an expansion factor (see fig. 3.4)

Typical values of α for modern electron guns at different storage rings vary from 10 to 100. At the TSR the expansion from 20 to 40 is normally used. For the CSR operation the expansion factor will be limited to 20 in order to keep the reduction of the electron density by the beam expansion at a reasonable level. Now from the electron energy distributions measured at the test setup giving a value of $k_B T_{\perp} \approx 10$ meV before expansion [67] and from the known expansion settings we can establish that in the interaction region the transverse electron temperature is less than 0.5 meV. This is about two orders of magnitude better than in the earliest working electron coolers. High expansion factor α goes at cost of electron density. Hence, using a photocathode and lower expansion factor allows to gain in the electron density compared to a thermocathode beam of the same temperature, which is especially important at low energy.

3.2 Ultra-low energy electron deceleration experiments

One of the main challenges for the ultra-low energy electron cooling is to achieve sufficient electron density in the beam. Sufficient density here means that the ion beam can be cooled within its storage lifetime at the CSR. The electron density is limited due to the space charge effects in the gun and the interaction region. Therefore, we first consider the theory of the space-charge-limited electron beam. Then we will look

at the experimental results on beam deceleration carried out at the TSR e-target in order to achieve an electron beam of maximum density. The experimental data on the electron density will be used later to set requirements on the magnetic optics of the CSR electron cooler and to derive the cooling times of heavy ions at the CSR.

3.2.1 Deceleration of a space charged limited electron beam

The current I emitted by an electron source depends on the applied extraction voltage U_{ext} as $I = pU_{ext}^{\frac{3}{2}}$, where the perveance p is determined by the electron gun geometry and has a usual value around $10^{-6} A/V^{\frac{3}{2}}$ (the unit $A/V^{\frac{3}{2}}$ is later called perv). Thus at ultra-low energies (1-10 eV) only maximum currents of about 1-30 μA are available corresponding to 10^5 - 10^4 electrons per cm^3 . As shown in eq. 2.25 the cooling force is proportional to the electron density. The same holds for the count rate in recombination experiments. The electron density at such low energies is defined by the space charge effects only, and not by the emissivity of the cathode. Therefore an increase of electron current by enhancement of the gun perveance would have a significant positive impact on the cooler performance. The limiting factor for the current increase in the gun, however, is the space charge potential created by the electron beam. This gets especially critical at low energies, where the electron motion is slow and the space charge potential is comparable to the electron kinetic energy. In addition, the *difference of contact potentials (DCP)* exists between parts of the electron optics made of materials with different work functions, such as NEA-GaAs photocathodes and gold-plated electrodes (see fig. 3.1). The DCP is of the same $\sim eV$ order of magnitude as the kinetic energy and the space charge potential and must be taken into account at ultra-low energies as an important contribution to obtain a proper energy calibration. For a given gun geometry, the only way to increase the current density is to extract the electrons from the gun at higher energy and then decelerate the electron beam to the required energy. In this scheme the limitation on the current density results not from the gun itself, but rather from the possibility to decelerate a beam of a given current. Such experiments were carried out at the TSR e-target in order to establish the range within which the current density can be varied.

The electrons emitted at the certain position in relation to the beam axis in a strong enough uniform guiding magnetic field will stay confined in the manifold of Larmor's radius close to this position along the track. For the typical TSR e-target experimental case reported below ($k_B T_{\perp} = 0.5$ meV $B = 400$ G) r_L is ~ 1 μm . Thus for calculations of the space charge effects we can assume that the *current density* across a sample area along the flow tube is constant. If the space charge potential is small compared to the kinetic energy of the electrons, then constant current density $\vec{j} = en\vec{v} = \text{const}$ implies an approximately uniform charge distribution $n = \text{const}$. Thus, for a beam of radius ρ in a drift tube of radius R using Gauß's theorem gives the well-known and widely used

parabolic and logarithmic space charge potential

$$\Phi(r) = \Phi(R) - \frac{ne\rho^2}{4\varepsilon_0} \begin{cases} 2\ln\left(\frac{R}{r}\right) & \rho < r < R, \\ 2\ln\left(\frac{R}{\rho}\right) + 1 - \frac{r^2}{\rho^2} & r < \rho \end{cases}. \quad (3.10)$$

This equation gives corrections to the mean kinetic energy of an electron beam in the drift tube taking as variables the density of the fully expanded beam and the beam line geometry.

The typical approach to characterize an electron gun is to consider the cathode as a flat infinite emitting surface, which emits the electron current of density \vec{j} normal to its surface. The collector is defined as a plane, parallel to the cathode and separated by a distance d set under potential U_0 relative to the cathode. In this case the one-dimensional Poisson equation for the space charge region is given by

$$\frac{\partial^2 U}{\partial z^2} = \frac{j\sqrt{m}}{\varepsilon_0\sqrt{2e}} \frac{1}{\sqrt{U}}. \quad (3.11)$$

The solution of this non-linear equation gives the well known three-halves power law $I = pU^{3/2}$ for the current ($j = \frac{4\varepsilon_0}{9} \sqrt{\frac{2e}{m_e}} \frac{U_0^{3/2}}{d^2}$ for the infinite emitting plane). The three-halves power law is used to characterize real electron guns by adjusting the perveance p to include the influence of the electrode geometry, the applied magnetic field and other parameters omitted in the simple 1-d model.

A modified approach should be used to calculate the space charge potential of a high current ultra-low energy electron beam. At the low energies and high beam densities the space charge potential is comparable to the kinetic energy. In this case the velocity \vec{v} and the particle density n are functions of the radial position $\vec{v}(r)$ and $n(r)$ connected by the current density conservation $\vec{j} = en\vec{v} = \text{const.}$ and Poisson's equation. However the condition $j = \text{const.}$ does not imply $n = \text{const.}$ as assumed in eq. 3.2.1. Let us consider the space charge problem in the interaction region of an electron cooler. A cylindrical electron beam of radius ρ is guided through a conducting cylindrical tube long compared to its radius R . In this region the problem can be considered in cylindrical coordinates in the way that all functions depend only on the radial coordinate and the variation along the z -axis can be left out. We define $U(r) = 0$ at the center of the beam. The space-charge-induced potential difference between zero and the beam line surface ($r = R$) is denoted as U_{SC} , while the potential difference between the beam line and the electron source is U_0 . A schematic of the introduced potentials on example of the TSR e-target geometry is provided in fig. 3.5.

The velocity of an electron at radial position r is then

$$v = \sqrt{\frac{2e}{m}(U_0 - U_{SC} + U(r))}; \quad (3.12)$$

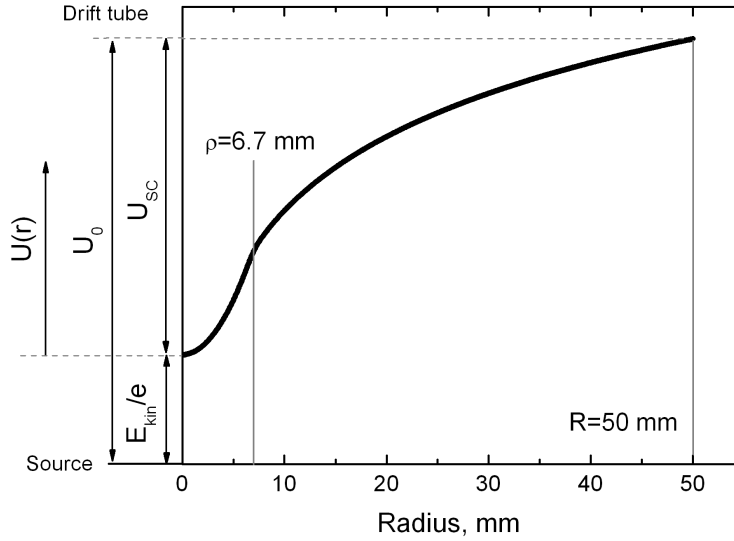


Figure 3.5: Potential distribution $U(r)$ across the drift tube in the presence of a high perveance electron beam of geometrical parameters typical for the TSR/CSR.

assuming a constant *current density* $j = I/\pi\rho^2$, the charge density is then $en = j/v$ and the cylindrical Poisson equation for the radial electric potential is given by

$$\frac{d^2}{dr^2}U(r) + \frac{1}{r}\frac{d}{dr}U(r) = \frac{I\sqrt{m}}{\varepsilon_0\pi\rho^2\sqrt{2e}} \frac{1}{\sqrt{U_0 - U_{SC} + U(r)}} \quad (3.13)$$

in the range $r < \rho$ while it is

$$\frac{d^2}{dr^2}U(r) + \frac{1}{r}\frac{d}{dr}U(r) = 0 \quad (3.14)$$

for $\rho < r < R$. Following the approach of Smith and Hartman [72], the equation 3.13 may be expressed in terms of the dimensionless variables s and ϕ where $s = r/a$, $\phi = U(r)/(U_0 - U_{SC})$ and

$$a^2 = \frac{\varepsilon_0\pi\rho^2\sqrt{2e}}{I\sqrt{m}}(U_0 - U_{SC})^{\frac{3}{2}}. \quad (3.15)$$

In these variables equation 3.13 turns into

$$\frac{d^2}{ds^2}\phi(s) + \frac{1}{s}\frac{d}{ds}\phi(s) = \frac{1}{\sqrt{1 + \phi(s)}} \quad (3.16)$$

In the region $\rho < r < R$ where the local charge density is zero, one can calculate the potential using eq. 3.14 as:

$$\frac{1}{r}\frac{d}{dr}\left(r\frac{dU}{dr}\right) = 0 \implies r\frac{dU}{dr} = C \implies U(r) = C\ln(r) + D \quad (3.17)$$

The potential must satisfy the boundary condition at $U(r)|_{r=R} = U_{SC}$ and at $r = \rho$ smoothly join the potential in the region $r < \rho$, where the local charge density is

non-zero. If we denote $U(r)|_{r=\rho} = U_\rho$ then at $r > \rho$

$$U(r) = \frac{(U_{SC} - U_\rho) \ln\left(\frac{r}{\rho}\right) + U_\rho \ln\left(\frac{R}{\rho}\right)}{\ln\left(\frac{R}{\rho}\right)}. \quad (3.18)$$

The differentiability condition

$$\left. \frac{dU(r)}{dr} \right|_{r=\rho-0} \stackrel{!}{=} \left. \frac{dU(r)}{dr} \right|_{r=\rho+0} \quad (3.19)$$

can be expressed in terms of ϕ and s as follows:

$$\frac{U_0 - U_{SC}}{a} \left(\frac{d\phi}{ds} \right) \Big|_{s_\rho} \stackrel{!}{=} \frac{U_{SC} - U_\rho}{\rho \ln\left(\frac{R}{\rho}\right)} \implies \phi_\rho = \phi_R - \ln\left(\frac{R}{\rho}\right) s_\rho \left(\frac{d\phi}{ds} \right) \Big|_{s_\rho}, \quad (3.20)$$

$$\text{where } \phi_\rho = U_\rho/(U_0 - U_{SC}), \quad s_\rho = \rho/a \text{ and } \phi_R = U_{SC}/(U_0 - U_{SC}). \quad (3.21)$$

Equation 3.20 may be regarded as an equation to determine the value of s_ρ which ensures derivability of the potential. Since ρ is known, this gives a and hence, with eq. 3.15 an equation connecting I , U_0 and U_{SC} . The method suggested by Smith and Hartman [72] to solve the equation requires us to assume that the solution of 3.16 is known, so one can introduce a function $u = sd\phi/ds$ and plot $\phi(s)$ as an implicit function of u , $\phi(u)$. Introducing $\tilde{\phi}(u) = \phi_R - \ln(R/\rho)u$, the equation 3.20, expressing the matching condition, is just $\tilde{\phi}(u_\rho) = \phi_\rho$. The intersection of the $\tilde{\phi}(u)$ line with the solution of eq. 3.16 in the inner region $s < \rho/a$, expressed as a function $\phi(u)$, gives us the value $\phi_\rho = \phi(u_\rho)$ that fulfills the matching condition. Using this value one can find s_ρ such that $\phi(s_\rho) = \phi_\rho$ (see fig. 3.6). Knowing that, one can find the beam current I . It is expressed in terms of the space charge ratio $x = U_{SC}/U_0$ using the definition of $a = r/s$, eq. 3.15, in the case $a = \rho/s_\rho$ as

$$I = \frac{s_\rho}{4} \sqrt{\frac{2e}{m}} (1-x)^{3/2} U_0^{3/2} = p U_0^{3/2}. \quad (3.22)$$

Thus, the current depends on applied voltage U_0 , the space charge ratio x and a further term s_ρ which also depends on x and the geometry.

Unfortunately the solution of the original equation 3.16 cannot be expressed in terms of elementary functions. One has to either approximate it analytically in terms of series expansion or to solve it numerically. First let us consider the analytical option. Using the boundary condition $\phi(0) = 0$ and taking s to be small (right hand side of eq. 3.16 set to 1) one can get in zero order approximation $\phi(s) = s^2/4$, which corresponds to constant charge density in the beam. Expanding $1/\sqrt{1 + \phi(s)}$ to $1 - s^2/8$

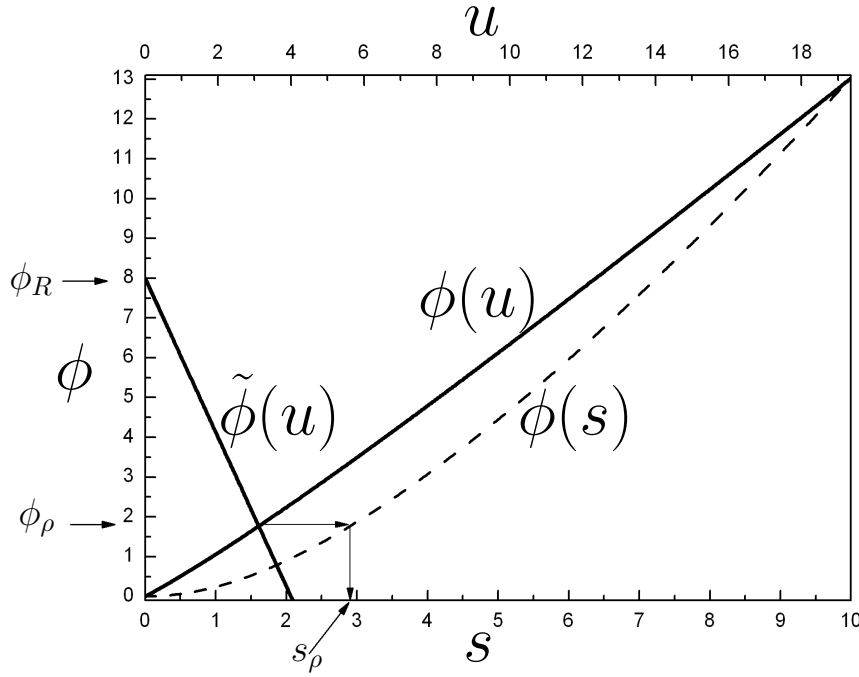


Figure 3.6: Dimensionless potential ϕ as a function of s and u , finding full beam current using the smooth joining condition for $\ln R/\rho = 2.01$, the case of the TSR e-target.

one gets a representation of $\phi(s)$ in the vicinity of zero:

$$\phi(s) = \frac{s^2}{4} \left(1 - \frac{s^2}{32} + \frac{7s^4}{4^3 6^2} + \dots \right). \quad (3.23)$$

Substituting this into equation 3.20 using up to the s^4 term in the parentheses, and introducing $y = R/\rho$ as a parameter one obtains

$$s_\rho^2 = \frac{1}{1 + 2 \ln y} \left(\frac{4x}{1-x} + \frac{1 + 4 \ln y}{32} s_\rho^4 - \frac{7s_\rho^6}{4^3 6^2} (1 + 6 \ln y) \right). \quad (3.24)$$

Starting from the approximation

$$(s_\rho^2)^{(1)} = \frac{1}{1 + 2 \ln y} \frac{4x}{1-x} \quad (3.25)$$

and re-iterating for the next terms one gets a series expression of s_ρ as a function of x

$$(s_\rho^2)^{(3)} = A \frac{x}{1-x} \left(1 + B \frac{x}{1-x} + C \left(\frac{x}{1-x} \right)^2 \right), \quad (3.26)$$

where

$$A = \frac{4}{1 + \ln y}, \quad B = \frac{1 + 4 \ln y}{8(1 + 2 \ln y)}, \quad \text{and} \quad C = \frac{1}{16} \left(\frac{(1 + 4 \ln y)^2}{2(1 + 2 \ln y)^4} - \frac{7(1 + 4 \ln y)}{9(1 + 2 \ln y)^3} \right). \quad (3.27)$$

In order to compare this analytic approximation to the numerical results let us first outline the domain of the problem by setting practical ranges of parameters ϕ , s , x , y . For an electron beam produced by the TSR e-target expanded by a factor of 20 and a 100 mm diameter drift tube, $y = 7.46$. To define the range where x is varying one needs to substitute the series expression of $s_\rho^{(3)}(x)$ into equation 3.22 and find the value of x , which makes the current maximum, as a function of y :

$$x_{I_{max}} = \frac{2}{3} \left(1 + \frac{1}{4} \frac{1 + 4 \ln y}{(1 + 2 \ln y)^2} \right). \quad (3.28)$$

As one can see in fig. 3.7, at $y = 7.46$ for the CSR case, the corresponding value of x is ~ 0.73 . Now we can get back to the definition of the dimensionless coordinate s in

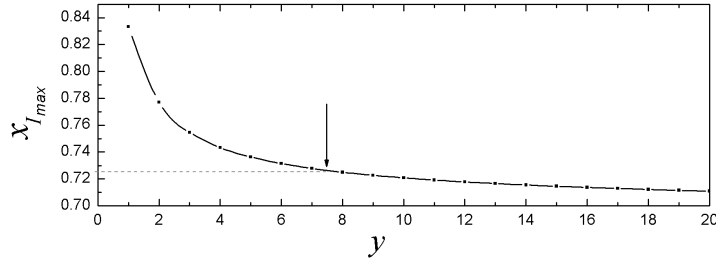


Figure 3.7: Value of x for maximum current as a function of y , the ratio $\frac{R}{\rho}$ of the drift tube (R) and the beam (ρ) radii.

equation 3.15 and rewrite it as

$$s = \frac{r \sqrt{I \sqrt{m}}}{\sqrt{\varepsilon_0 \pi \rho^2 \sqrt{2e} U_0^{3/2} (1-x)^{3/2}}}. \quad (3.29)$$

The lowest boundary of s is obviously zero ($r = 0$). The original equation 3.16 is solved only for $r < \rho$. As we have seen the maximum current is achieved at $x \sim 0.73$ which makes the term $1/(1-x)^{3/4}$ less or equal to 2.67. $\sqrt{\frac{I}{U_0^{3/2}}}$ equals the square root of the beam perveance, which for a factor of 10 current enhancement would give $2.4 \times 10^{-3} \text{ A}^{1/2}/\text{V}^{3/4}$. The combination of constants in front of the expression gives $\sqrt{\frac{\sqrt{m}}{\varepsilon_0 \pi \sqrt{2e}}} = 2.46 \times 10^2 \text{ V}^{3/4} \text{ A}^{-1/2}$. As a result $s_{CSR} \in [0; 1.58]$.

Now we can integrate equation 3.16 specifically in the region of interest and compare it to the analytical series approximation 3.23. There is perfect agreement with the numerical solution for $s < 2$ (see fig. 3.8).

Using the series expansion for s_ρ one can get $p(x)$ for the TSR/CSR geometry as shown in fig. 3.9. This theoretical understanding allows us to interpret the experimental data on the beam deceleration in the next section.

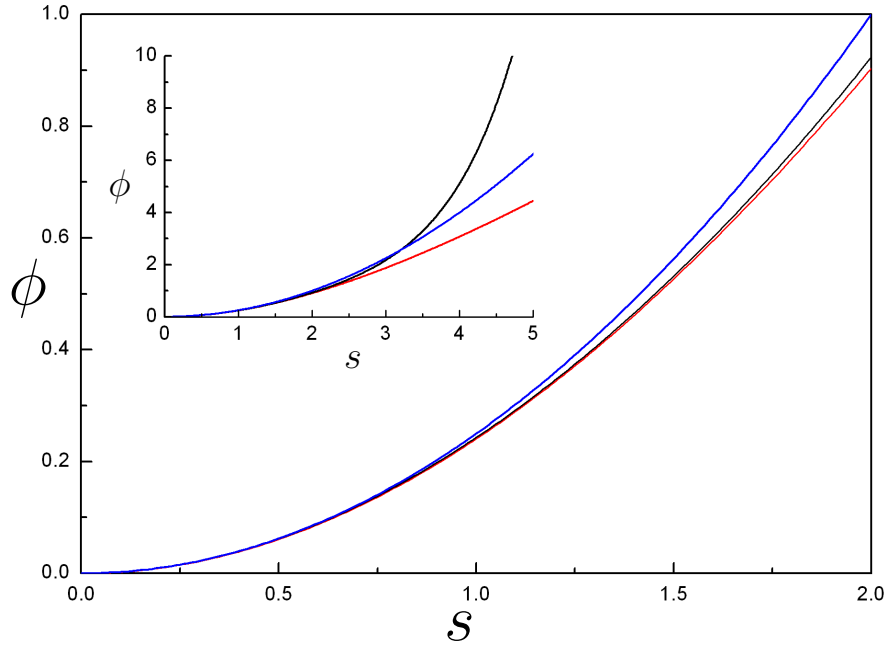


Figure 3.8: Analytical series approximation up to $O(s^6)$ term (black) compared to numerically integrated ϕ (red) and zero order parabolic approximation (blue). The insert shows the extended region demonstrating the limits of the series representation.

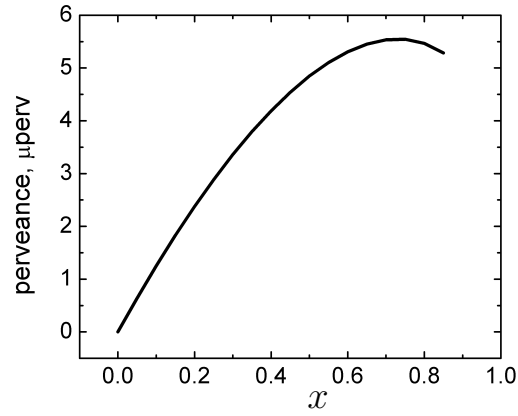


Figure 3.9: Perveance as a function of x for the TSR electron target.

3.2.2 Measurements

The beam deceleration technique as a method to enhance the electron gun performance for an ultra-low energy beam has been implemented at the TSR e-target and set of experiments have been carried out. The purpose of these experiments was to reach the maximum beam densities at ultra-low energies and test the beam quality in such conditions. The scheme and the layout of the setup are shown in fig. 3.10

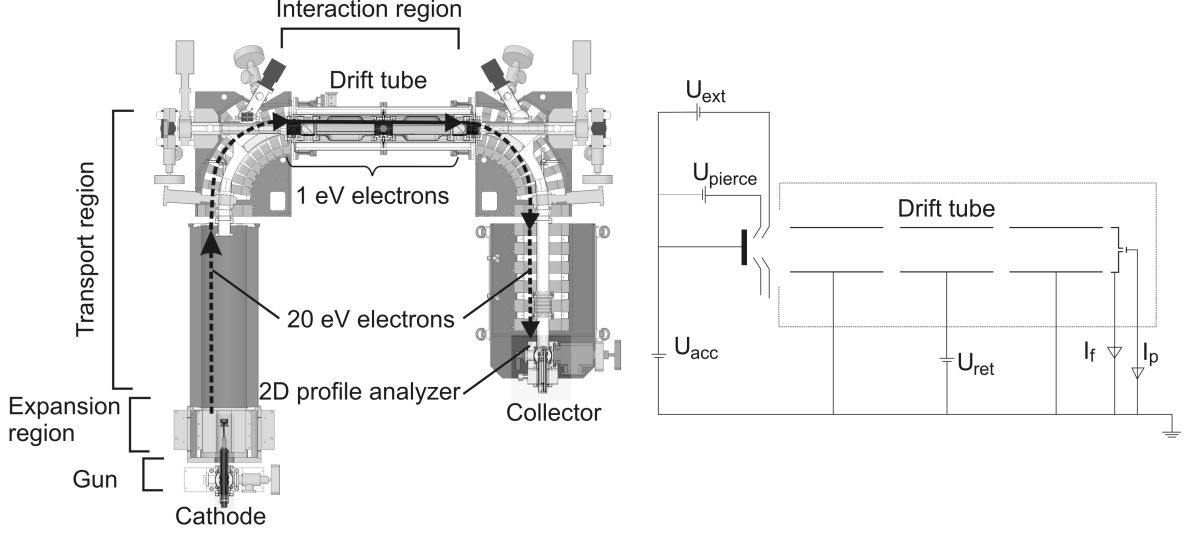


Figure 3.10: The TSR e-target set up for the experiments in the ultra low energy operation mode.

After extraction and expansion at ~ 20 eV kinetic energy ($U_{acc} \sim 20$ V), the electron beam is decelerated in the interaction section of the electron target. The scheme is similar to a filter-lens retarding field analyzer as proposed by Caulton [73] for axial velocity distribution measurements. During the beam transport towards the interaction region, the energy of the electrons can be assumed to be independent on the extracted current if one neglects the difference in the beam space charge potential for 20 eV electrons. The electron optics of the gun (apart from the extraction electrode, whose voltage U_{ext} will be variable), expansion and transport sections can thus be static while the electron energy in the interaction region is varied by tuning the retarding potential U_{ret} of the drift tubes surrounding the beam axis.

For the potential along the electron trajectory, which defines the kinetic energy E_{kin} finally reached by the deceleration, a number of influences must be taken into account as shown in fig. 3.11. These include the DCP due to the difference of the cathode and anode work functions W_c and W_a , the space charge potential of the beam U_{SC} and the changing by the applied extraction voltage retarding potential at the cathode, which at given acceleration and retarding potentials U_{acc} and U_{ret} finally defines the potential difference U_0 (in terms of the previous section) between the electron source and the drift tube. The gray areas show the electron energy distributions: The Boltzmann thermal distribution in the bulk crystal, and the broadened distribution of the emitted electrons near the cathode surface (as in fig. 3.2) with a Boltzmann-like tail at higher energies

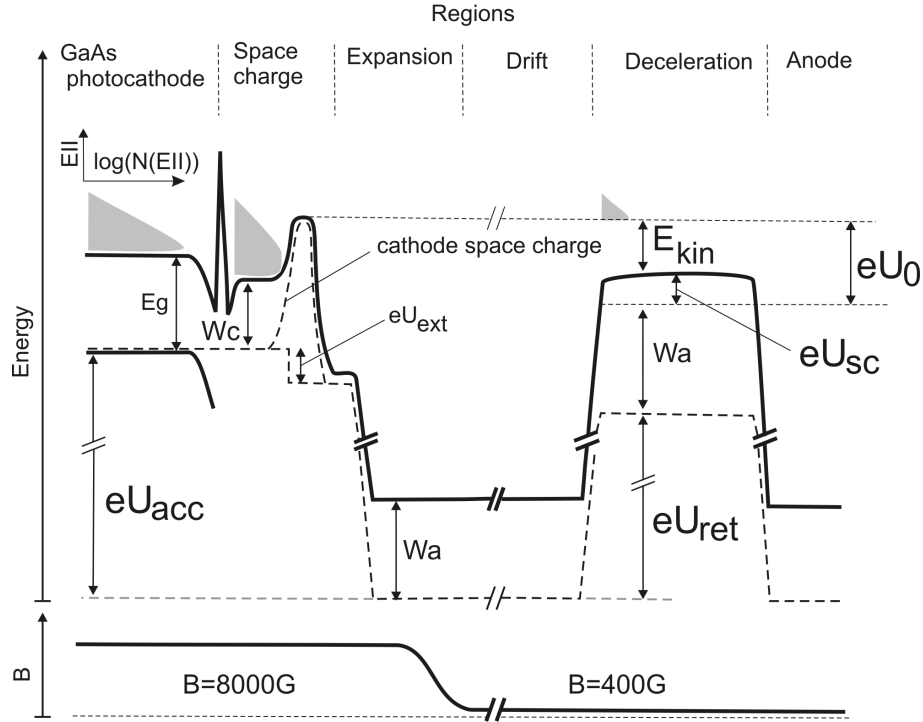


Figure 3.11: Potential diagram along the electron track. Where U_{acc} is the accelerating voltage U_{ret} is the retarding voltage, W_a is the work function of the drift tube and the anode, W_c is the cathode work function, U_0 is the potential difference between the electron source and the drift tube, U_{sc} is the space charge potential of the electron beam in the deceleration region and E_{kin} is the kinetic energy of the electron beam in the deceleration region.

and the cut Boltzmann-like distribution in the beam. In the further reported tests the photocathode was operated at room temperature, so the exponential tails have a $1/e$ decay constant close to the room temperature value of 26 meV. The extracted current is defined by the applied extraction voltage and the perveance of the gun. The potential U_{pierce} of the Pierce electrode was constant and has been chosen experimentally such as to provide the most uniform current density distribution across the beam.

In all the experiments the electron beam has been guided towards the interaction region and then the retarding voltage U_{ret} was increased while monitoring the properties of the electron beam after the deceleration. Fig. 3.12 shows the current measured at the collector anode as a function of the retarding potential. Hereafter plots of this type are denoted as deceleration curves. In addition to the integral final electron current I_f , the current density distribution across the beam was measured by a profile analyzer, where a small part of the beam I_p is cut out by a pinhole in the center of the collector cup. The current distribution is measured by applying steering magnetic fields in the collector section, which tilt the electron beam in both directions perpendicular to the beam axis. Each profile measurement took about 15 minutes.

Up to a certain value of the retarding potential (point A in fig. 3.12) the integral transmitted current is constant and the distribution of the current density across the beam is flat and circular (profile A in fig. 3.12). Upon rise of the retarding potential above this threshold, the current drops because of partial electron reflection. This

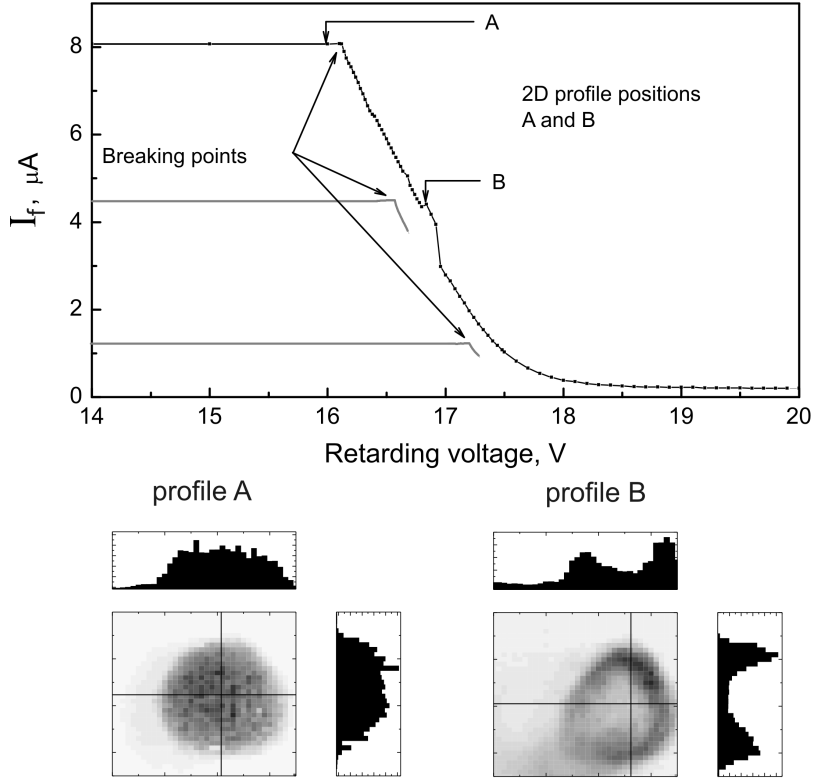


Figure 3.12: Deceleration curve of a 8 μA electron beam. The curve breaks at at 16.12V retarding voltage. Profile A, measured 50 meV before the break, is still flat. In profile B, measured at 16.8 V, the current density in the beam center is strongly reduced due to enhancement of the space charge in this area. The grey curves demonstrate how the breaking point shifts at lower currents.

threshold is found to be very sharp, hereafter we refer to it as the breaking point of the deceleration curve. In case of low total current, the reflection is caused mainly by the retarding potential. For high integral current, the stopping potential is a superposition of the retarding potential and the beam space charge potential. The latter is strongly enhanced by the low beam kinetic energy. Since the space charge potential is higher in the center of the beam, reflection occurs in the central area first. This can be clearly seen in current profile B of fig. 3.12, where the integral electron current has been cut by a factor of two because of reflection. The small rise near point B in the otherwise smooth deceleration curve is caused by enhanced efficiency of the collector after a beam steering that was performed prior to the profile measurement at B. The subsequent drop of the current at higher U_{ret} is the result of a cathode degradation due to pollution by residual atmosphere molecules desorbed from surrounding area under influence of the backscattered electrons during the profile measurement.

Values of $(U_{ret})_B$ at the breaking point were obtained for a series of deceleration curves for varying current set by U_{ext} . Conversion from applied voltages to the actual potential difference between electron source and the drift tube (U_0) as well as the effective perveance of the beam can be found in the following way. For each breaking point we need to eliminate the contribution from the changing extraction potential and the DCP in order to obtain U_0 . The conversion algorithm is illustrated in fig. 3.13. The

left side of the picture shows the breaking voltage $(U_{ret})_B$ as a function of the extracted current. For currents less than 10 nA, where the space charge of the expanded electron beam in the drift tube is negligible, the breaking point corresponds to equal potentials of the source (i.e. the effective potential barrier in front of the cathode) and the drift tube. Previous work [67] has shown, that (at the applied laser power of 600 mW and extracted less than 100 μ A) only electrons from the exponential Boltzmann tail of the electron energy distribution in the GaAs conduction band are extracted from the cathode. The expected exponential dependence of the emission current on the extraction potential is visible in the low current region of fig. 3.13, and corresponds to a longitudinal electron temperature of $k_B T_{||} = 30$ meV (as also reported in [67] the exponential constant is found to be slightly above the actual temperature of the bulk crystal). At higher emission currents the electron space charge in the drift tube starts to play a role, resulting in lowering of the breaking point below the potential of the electron source. The potential of the latter can be found by extrapolating the exponential trend $U_s = \frac{k_B T_{||}}{e} \ln I_0/I$ found for current values of less than 10 nA (dashed blue line in fig. 3.13). The difference U_0 between the extrapolated source potential and the measured breaking point represents the minimum voltage difference $(U_0)_{min}$ between the source and the drift tube at which the current I can be transferred. The DCP contribution is excluded, as shown in fig. 3.13, while the space charge contribution is still included in U_0 .

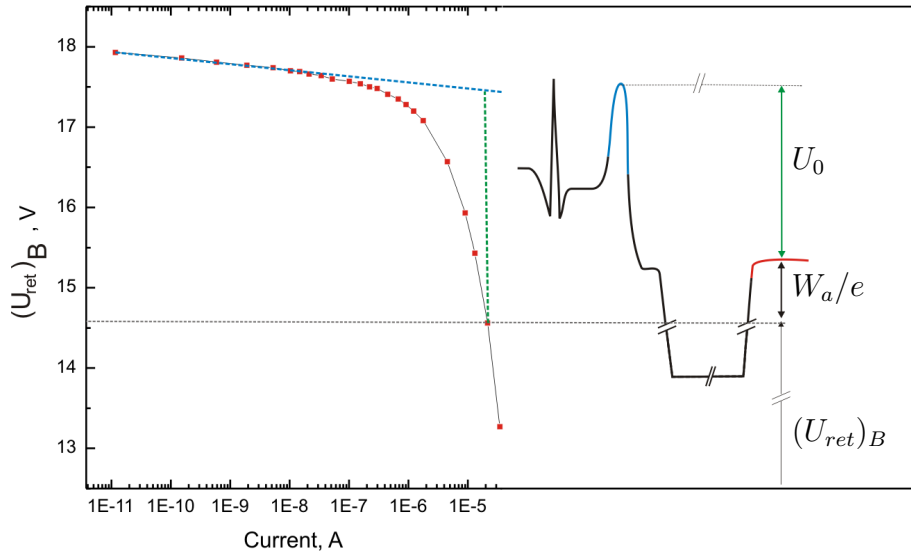


Figure 3.13: Rescaling from the retarding voltage at the breaking point $(U_{ret})_B$ to the actual potential difference between the electron source and the drift tube U_0 .

The transmitted electron current I measured at the collector as a function of the potential difference U_0 between the source and drift tube defines the maximum perveance p of the setup, defined as $p = I/U_0^{3/2}$. The currents at the various values of $(U_0)_{min}$ are shown in fig. 3.14. The fitted perveance value $p = 4.1 \mu\text{perv}^1$ is much higher than the

¹the unit μperv is defined as $10^{-6} \text{AV}^{-3/2}$ (1 μA at 1 V)

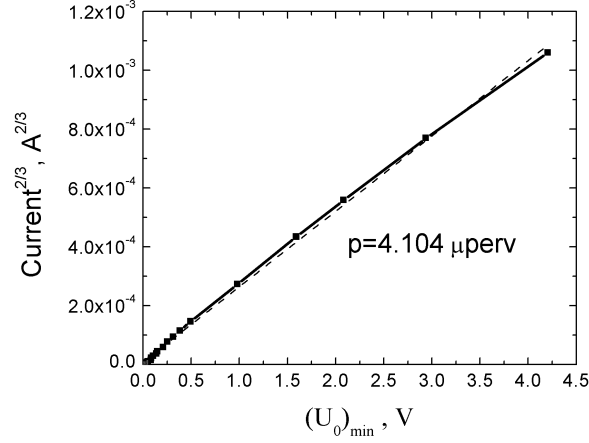


Figure 3.14: The maximum experimental perveance is found to be 4.1 μperv .

gun perveance. It approaches to the maximum perveance of the deceleration scheme of 5.4 μperv , but stays somewhat below it. This can be explained by the observation that the current profile is not completely flat, but shows slightly higher current density near the the middle of the beam, as visible in the measured current density profiles (see fig. 3.12). The maximum perveance gives us the maximum extractable current at given energy $E_{kin} = (1 - x)U_0e$ where x can be found from U_0 and the set current I via the perveance law and fig. 3.9.

An illustration of the procedure for setting a specific energy E_{kin} and current is given in fig. 3.15. Lines of constant kinetic energy E_{kin} in the coordinates x and U_0 are hyperbolic curves $x = 1 - E_{kin}/U_0$. We can choose a point (U_{0ex}, x_{ex}) on such a curve of a specified energy and find a corresponding perveance $p_{ex} = p(x_{ex})$ on the lower left plot. Taking this perveance we can plot the current I as a function of U_0 as $I = p_{ex}U_0$, and find $I_{ex} = I(U_{0ex})$. The maximum current is defined by our effective perveance of 4.1 μperv . Operation without drift tube deceleration corresponds to 0.58 μperv . At the kinetic energy of 1 eV, the deceleration scheme thus enhances the current density by a factor of 14.

The measurements discussed have also shown that a proper value of the retarding voltage U_{ret} can be found for the desired U_0 . As illustrated in fig. 3.13, U_{ret} must be lowered with respect to the extrapolated low-current limit U_s by the value U_0 . This way, electron beam energies E_{kin} in the of eV or less can be adjusted in a controlled way.

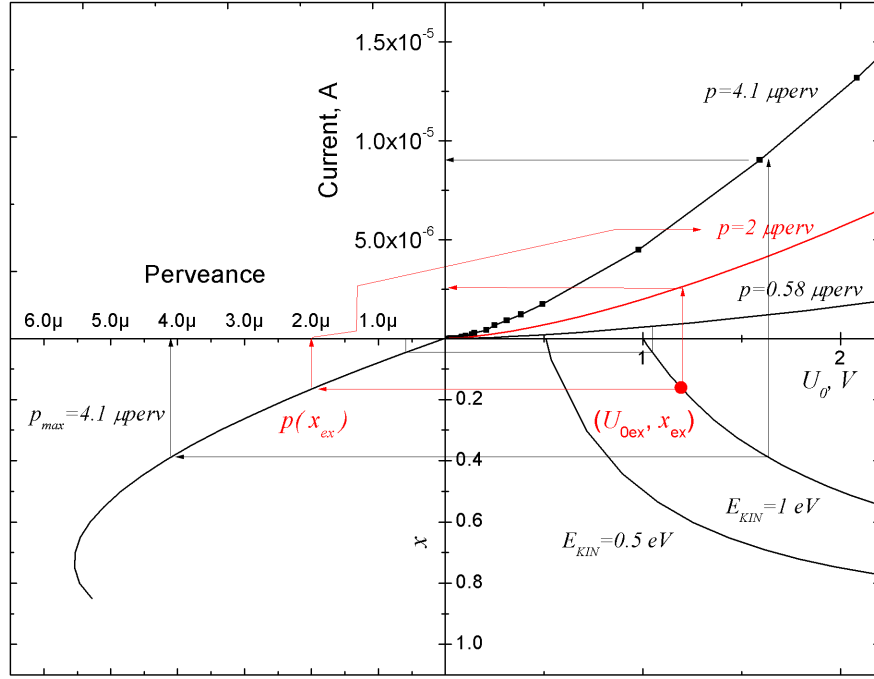


Figure 3.15: Current enhancement due to beam deceleration. Comparison of maximum extractable current (perveance $4.1 \mu\text{perv}$) with normal operation mode (perveance $0.58 \mu\text{perv}$) for 1 and 0.5 eV kinetic energies. The plot in left bottom corner is fig. 3.9. The bottom right gives the curves of constant kinetic energy in the coordinates U_0 and x , the top right corner shows the current I as a function of U_0 according to $I = pU_0^{3/2}$ for the normal and maximum values of the beam perveance.

3.3 Parameter ranges

In this section we outline the ranges of parameters relevant to the ultra-low energy electron beam and the ion beam at the CSR. The CSR is able to store ion beams of energy E_i ranging from 20 to 300 keV/q. The energy of a velocity matched electron beam for electron cooling scales as $E_e = E_i m_e / M_i$ where m_e and M_i are the electron and the ion masses. The electron cooling is more effective at higher energies, therefore in *all* further consideration it is always assumed that the ion beams of different masses have the kinetic energy of 300 keV. The highest energy for electron cooling is 163 eV corresponding to protons. It is obvious that for most of the species with mass-to-charge ratio over 16 a.m.u./q only ultra-low cooling energies below 10 eV are relevant. Thus in the further discussions we will pay more attention to either low electron energies if talking about the electron beam, or high ion masses if discussing combined phenomena. The lowest limit of the electron energy was set to 1 eV, as the available current gets low, the precision of the voltage settings starts to be important and the cooling time is expected to reach unacceptably high values. Yet the reader should keep in mind that this boundary is in some sense arbitrary. Thus in the further section when talking about electron cooling we will *always* assume the electron energy range of 1-160 eV and the ion mass range 1-160 a.m.u. for singly charged ions. We also will be more concentrated on electron energies below 10 eV and the ion masses above 20 a.m.u., apart from some

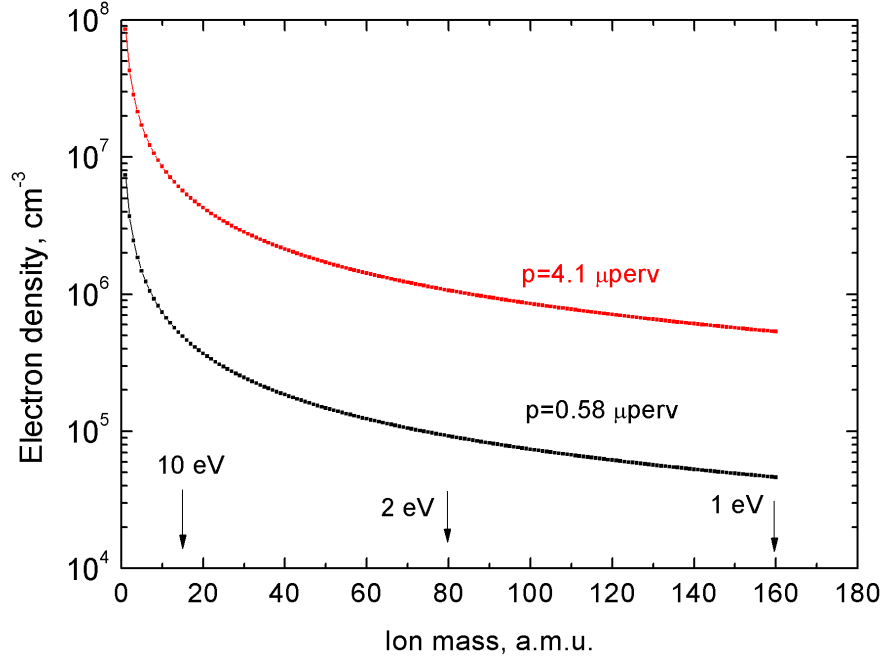


Figure 3.16: Density of the velocity matched electron beam of 0.58 and 4.1 μperv perveance as a function of the ion mass.

minor topics where it will be mentioned explicitly. The electron densities achievable in the experimentally relevant conditions can be calculated for the specified electron kinetic energy corresponding to the ion mass and the chosen space charge parameter x (see fig. 3.15) defining both the perveance $p(x)$ and the necessary voltage U_0 . These two define the extractable electron current as shown in the previous section. The known kinetic energy, the current, the cathode diameter of $d = 3$ mm and the expansion factor $\alpha = 20$ give us the density of the electron beam in the interaction section. The electron densities available for the electron cooling of ions of varying masses are shown for the cases of the two beam perveances of 4.1 and 0.58 μperv in fig. 3.16. These values are used later to calculate the longitudinal electron temperatures and cooling times of the ions.

3.4 Performance and modeling of an ultra-low energy cooling device at CSR

The performed experiments demonstrate that an ultra-low energy electron beam in the parameter range required for the CSR is feasible. In the present section we derive the performance that can be expected at the CSR and develop a suitable magnetic beam guiding system compatible with the conditions at the CSR. We start with a calculation of the longitudinal electron temperature based on the electron densities experimentally obtained in the previous section. Knowing this, we proceed with calculation of the expected cooling times for heavy ions at the CSR to assure the principal feasibility

of such experiments. Then we proceed with the design and the numeric simulations of the magnetic system for the CSR electron cooler. The design is also based on the parameters of the CSR lattice and ion sources given in section 2.2.

3.4.1 Longitudinal temperature and relaxation mechanisms

The last key parameter of the electron beam crucial for the calculation of the cooling force, not yet considered above, is the longitudinal temperature. The longitudinal beam temperature consists of contributions originating from the source-dependent initial energy spread and from varying interactions of the electrons in the beam. After the electrons are emitted from a cathode of temperature T_C , adiabatically expanded so that the transverse energy is mostly transferred to the longitudinal motion and accelerated to the energy W , the average kinetic energy of thermal longitudinal motion, $\frac{3}{2}k_B T_C$ is reduced in the co-moving frame [74] so that the energy spread ΔE_{\parallel} is then equal to

$$\Delta E_{\parallel} = \left(\frac{3}{2} k_B T_C \right)^2 \frac{1}{4W} = \frac{9(k_B T_C)^2}{16W}. \quad (3.30)$$

There is also potential energy of electrons in the beam due to Coulomb interaction which contributes in the longitudinal temperature via a mechanism called longitudinal-to-longitudinal relaxation (LLR) [75, 74]. In an acceleration at low electron temperatures the electron beam will internally arrange in such a way, that the electrons will have the lowest possible potential energy; in this process the potential energy of initially disordered beam will be transferred into kinetic energy. To take this into account one needs to know the dependence of correlation energy of the electron beam on its temperature. An empiric formula for the correlation energy satisfying both extremes of high- and low-ordered plasmas as well as all intermediate cases is proposed in [75]:

$$E_{corr} \approx -\frac{e^2(\pi n)^{\frac{1}{3}}}{4\pi\epsilon_0} \sqrt{\frac{e^2(\pi n)^{\frac{1}{3}}}{e^2(\pi n)^{\frac{1}{3}} + 4\pi\epsilon_0 k_B T_{\parallel}}}. \quad (3.31)$$

Thus the full internal energy of the magnetized electron gas at thermal equilibrium is

$$E_{int} \approx \frac{k_B T_{\parallel}}{2} - \frac{e^2(\pi n)^{\frac{1}{3}}}{4\pi\epsilon_0} \sqrt{\frac{e^2(\pi n)^{\frac{1}{3}}}{e^2(\pi n)^{\frac{1}{3}} + 4\pi\epsilon_0 k_B T_{\parallel}}}. \quad (3.32)$$

Assuming that the internal energy right immediately after the acceleration is equal to that after thermalization one obtains

$$\frac{9k_B T_C^2}{16W} = \frac{k_B T_{\parallel}}{2} - \frac{e^2(\pi n)^{\frac{1}{3}}}{4\pi\epsilon_0} \sqrt{\frac{e^2(\pi n)^{\frac{1}{3}}}{e^2(\pi n)^{\frac{1}{3}} + 4\pi\epsilon_0 k_B T_{\parallel}}}. \quad (3.33)$$

For the typical CSR energies and current densities (section 3.3) the equilibrium longitudinal temperature is shown in fig. 3.17a. The contribution of the LLR mechanism is

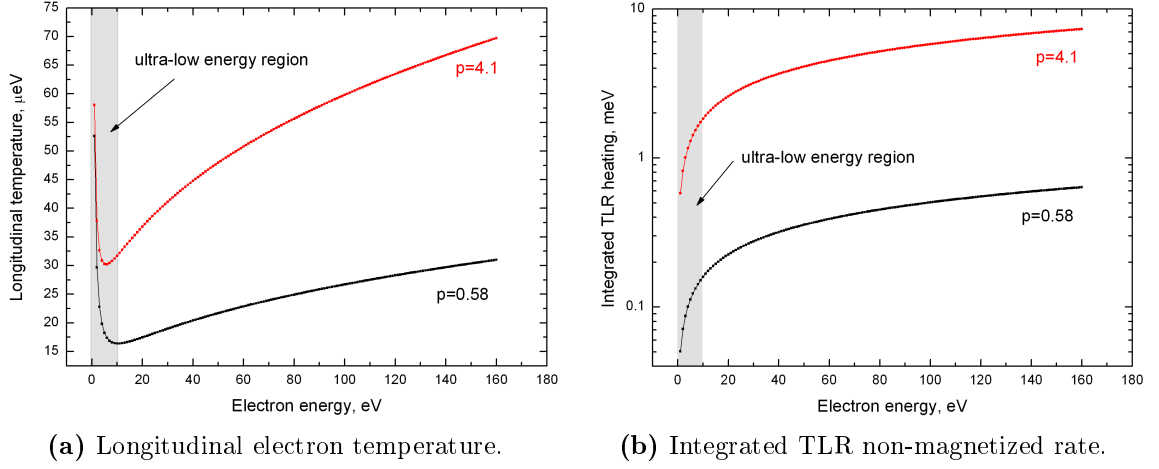


Figure 3.17: Longitudinal electron temperatures (left) and integrated over 3 meters TLR rates in the absence of magnetic field (right) for the CSR electron cooler energy range (1-160 eV) for electron density values from normal (black) to maximally enhanced (red).

notable for higher energies above 20 eV, whereas the initial energy spread dominates in the ultra-low energy region relevant for cooling of heavy ions.

Another relaxation mechanism is the heat exchange between the longitudinal and transverse degrees of freedom. This process is called transverse-to-longitudinal relaxation (TLR) [76] and in the absence of a magnetic field is quite effective. The equipartition rate in the approximation of a *non-magnetized* plasma is given by [76]

$$\left(\frac{dk_B T_{\parallel}}{dz}\right)^0 = \frac{4e^4 n}{(4\pi\epsilon_0)^2 \sqrt{W} k_B T_{\perp}}. \quad (3.34)$$

The relaxation rates integrated over 3m length for expected electron densities in case of a non-magnetized electron beam are shown in fig. 3.17b. For electron energies above 40 eV at normal electron density and for any energy at maximally enhanced current the transverse and longitudinal degrees of freedom will be fully equalized, so that T_{\parallel} will rise by two orders of magnitude in the absence of a magnetic field. However TLR can be significantly suppressed by a magnetic field that decouples the transverse motion. An empirical formula proposed by Dikansky et al. [75] describes the influence of the magnetic field on the relaxation rate as an exponential dependency:

$$\left(\frac{dk_B T_{\parallel}}{dz}\right)^{mag} = \left(\frac{dk_B T_{\parallel}}{dz}\right)^0 \exp \left[-\frac{2.8e^2}{r_L (e^2 n^{\frac{1}{3}} + 4\pi\epsilon_0 k_B T_{\parallel})} \right]. \quad (3.35)$$

This empirical expression derived from experimental data takes into account that the interaction between two electrons depends on both the ratio of the mean inter-particle distance $d = n^{-1/3}$ to the Larmor radius r_L , which characterizes the interaction in the

perpendicular plane, and on the longitudinal temperature that adds to the relative motion.

As one can see in fig. 3.18 the TLR can be kept well below tolerable limits in the presence of a sufficiently strong magnetic field of 20-50 Gauss depending on used energy and effective perveance. This is for both perveances in the ultra-low energy regime and for the low perveance at high energies. The case of high perveance at high energy is not of practical interest.

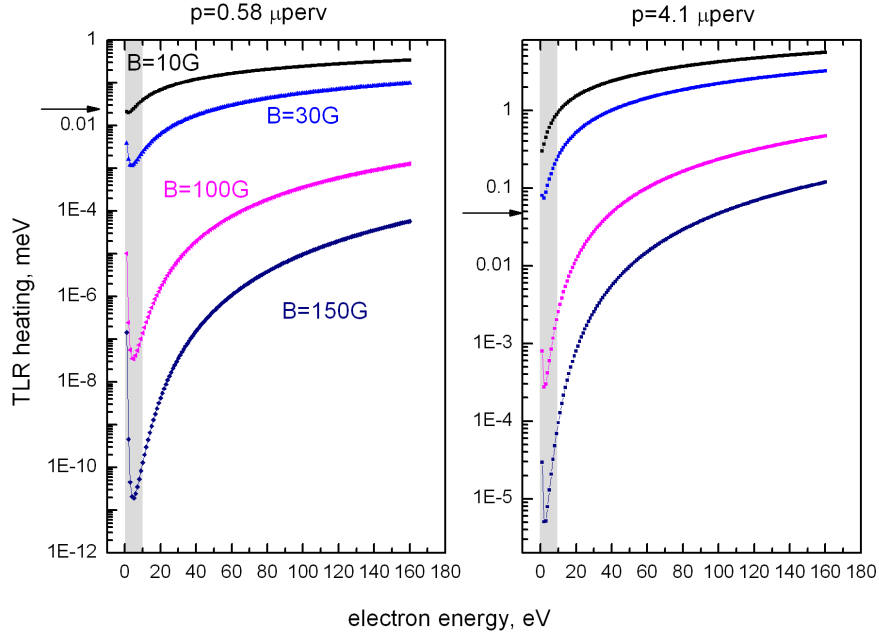


Figure 3.18: Integrated over 3 meters length TLR relaxation rates for the CSR electron cooler energy range (1-160 eV) for electron density values corresponding to normal (left) and maximum enhanced (right) perveance for magnetic field equal to 10, 30, 100 and 150 Gauss. Gray areas indicate the ultra-low energy region, corresponding to the most of the species to be researched at the CSR. The arrows show the values of the longitudinal temperature $k_B T_{||}$.

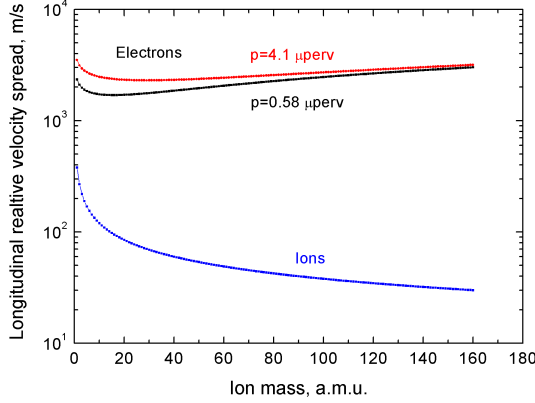
3.4.2 Cooling times of heavy ions

After we now obtained the ranges of the electron beam parameters such as T_{\perp} , $T_{||}$ and n (as summarized in table 3.1) we can make the necessary simplifications in the equation for the cooling force, eq. 2.25. If we look back to the section 2.2 we can see that according to eq. 2.10 and eq. 2.9 the ion transverse and longitudinal temperatures are 11.1 eV and 0.75 meV, respectively, independent on the ion mass for an ion beam with an emittance completely filling the ring acceptance. Comparing the velocity spreads of the electrons and the ions according to their transverse and longitudinal temperatures, we see that $\Delta v_{ion} < \Delta v_{el}$ for both directions and for ion masses above 25 a.m.u. (see fig. 3.19).

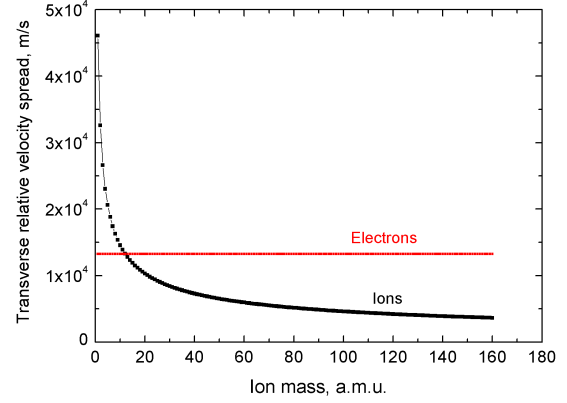
Thus, one can use asymptotic approximations of the cooling force for this special case for both transverse and longitudinal directions. These asymptotic approximations

Table 3.1: Parameters of the electron and ion beams used in the calculations

Parameter	value/source
$k_B T_{\perp, ion}$	11.1 eV, see sec 2.2 eq. 2.10
$k_B T_{\parallel, ion}$	0.75 meV, see sec 2.2 eq. 2.9
$k_B T_{\perp, el}$	0.5 meV, see sec. 3.1.1
$k_B T_{\parallel, el}$	15-60 μ eV, see fig. 3.17a depending on p for $E_{el} < 10$ eV
n_e	$3.4 \times 10^6 - 4.6 \times 10^4$ cm $^{-3}$ see fig. 3.16 for $M_i > 25$ depending on p
L_C	4.5-2.4 depending on n



(a) Longitudinal velocity spreads.



(b) Transverse velocity spreads.

Figure 3.19: Longitudinal and transverse velocity spreads of electrons and ions.

according to [75] are

$$F_{\perp}(v_{i\perp}) = -\frac{z^2 e^4 n L_C}{32 \sqrt{\pi} m_e \varepsilon_0^2} \frac{v_{i\perp}}{\Delta v_{el\perp}^3}, \quad (3.36)$$

$$F_{\parallel}(v_{i\parallel}) = -\frac{z^2 e^4 n L_C}{4\pi (2\pi)^{\frac{3}{2}} m_e \varepsilon_0^2} \frac{v_{i\parallel}}{(\Delta v_{el\perp})^2 \Delta v_{el\parallel}}. \quad (3.37)$$

These equations specify the $1/e$ cooling times τ defined as $F_i = dp_i/dt = -(1/\tau)M_i v_i$ where M_i is the ion mass. The effective time necessary to cool an ion beam is then $t = \tau L_{ring}/L_{cooler}$ where L_{ring}/L_{cooler} is the ratio of the ring length to the length of the interaction region of about 50. The calculated effective $1/e$ time to cool an ion beam of singly charged 300 keV ions of given mass for transverse and longitudinal degrees of freedom is shown in fig. 3.20a and 3.20b. The red lines of shorter cooling times correspond to maximum electron density using deceleration at an effective perveance of 4.1 μ perv, whereas the black lines show the times to cool an ion beam using non-enhanced current density. In all cases the ion transverse and longitudinal temperatures are 11.1 eV and 0.75 meV, respectively, obtained from the CSR lattice properties including acceptance for 300 keV beams in 2.2. The longitudinal electron temperatures from fig. 3.17 are used together with the electron beam densities from fig. 3.16. The transverse electron temperature is set to 0.5 meV.

As we see, cooling times even for the maximum electron density for heaviest ions are getting close to the expected ion lifetimes, and for not enhanced condition go far

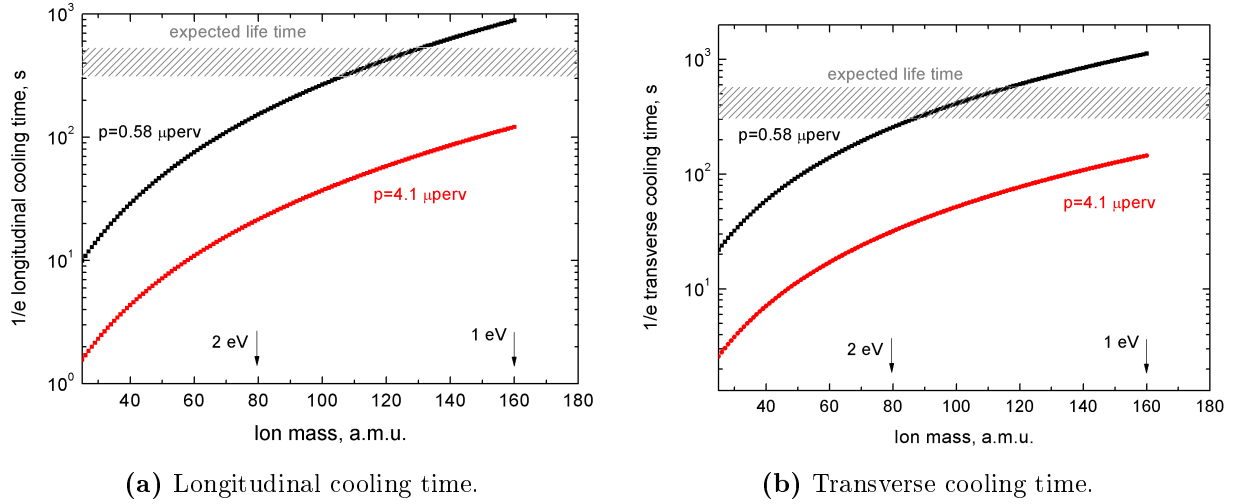


Figure 3.20: Transverse and longitudinal times to cool 300 keV ions, of 11.1 eV transverse and 0.75 meV longitudinal temperatures using enhanced (red) and not enhanced (black) electron beam.

beyond. Thus the electron beam densification by application of the deceleration technique is crucial for achieving phase space cooling. The mass of 160 a.m.u. corresponding to about 1 eV cooling energy seems to be a limit for the phase space cooling as the time to reach thermal equilibrium reaches ~ 500 s ($3 \times$ the $1/e$ cooling time) even for the electron beam of maximum density. Moreover the accuracy of the energy calibration as well as rising longitudinal temperatures will make operation at lower energies questionable.

3.4.3 Magnetic system for the cooler

It was already mentioned that for the operation of the CSR electron cooler a sufficiently strong magnetic field must guide the electron beam. The requirements to the field strength originate from a variety of processes that are suppressed by the guiding field, like the TLR process already discussed. Generally, a stronger magnetic field improves all aspects of the electron beam regarding the cooling process. On the other hand manufacturing of stronger magnets is more complicated and expensive. Even more important is that the magnetic field also affects the ion beam. In the regions where the ion and the electron beams are merged or separated, there is a component of the magnetic field perpendicular to the ion velocity causing deflection of the ions by an angle $\gamma = \Delta p_{\perp}/p_{\parallel} = q \int B_{\perp}(s)ds/\sqrt{2EM_i}$. The deflection can be managed by a proper compensation, eliminating the zero order effect, but there are residual effects due to the inhomogeneity of $B_{\perp}(x, y)$ and varying $\int B(s)ds$ depending on the perpendicular coordinates x, y of an ion in the beam. Therefore the guiding field magnitude should be chosen high enough to provide a high quality electron beam, but as low as possible to ease the design of magnets and minimize the distortion of the ion beam.

Apart from suppressing the TLR, there are two more conditions to be fulfilled by the guiding field. First, the electron beam must be kept from blowing up due to Coulomb

repulsion of the electrons in the beam. Second, in all curved parts of the electron track the field must be strong enough to keep the mean electron velocity always parallel to the magnetic field lines.

To find the minimum magnitude of an axially symmetric guiding field confining a beam of electrons with a certain charge density and velocity we use the approach of Busch [77]. In cylindrical coordinates one can write the equation of electron motion in the radial direction as

$$\ddot{r} = -\frac{\partial}{\partial r} \left(\frac{e^2}{2m^2} A_\phi^2 + \frac{e}{m} U \right), \quad (3.38)$$

where A_ϕ is the azimuthal component of the magnetic vector potential and U is the electric potential. For a solenoidal magnetic field the vector potential has a ϕ -component only and is given by $A = rB/2$. The electric potential close to the middle of the beam can be taken as parabolic $U = ner^2/4\epsilon_0$. As a result, equation 3.38 turns into

$$\ddot{r} = -r \left(\frac{e^2}{4m^2} B^2 - \frac{e}{2m} \frac{ne}{\epsilon_0} \right), \quad (3.39)$$

which has either an oscillating or an exponential solution, depending on which term dominates. For maximum electron densities of $1.6 \times 10^5 - 8 \times 10^7 \text{ cm}^{-3}$ ($p=4.1 \text{ } \mu\text{perv}$, 1-160 eV) the oscillation frequency gets imaginary and the electron beam blows-up at $B = 1.8 - 40 \text{ Gauss}$ (0.6-13 G for $p=0.58 \text{ } \mu\text{perv}$). This is automatically fulfilled by the requirements for TLR suppression. Same as for the TLR case (see fig. 3.17), fields above 30 Gauss are necessary only for a combination of enhanced beam density and high energy which is not of practical interest, because at such energies the electron density is sufficient even without the beam deceleration and is much higher than that available at lower energies at any practically possible value of perveance.

The criterion for curved parts of the track is in fact the criterion of adiabatic electron transport. In the same way as previously for the field magnitudes the field orientation should change in a way, that the field gradient is small compared to the electron ‘‘Larmor length’’ λ_L (see sec. 3.1.3). Introducing adiabaticity parameter ξ the criterion is

$$\xi = \frac{\lambda_L}{B} \left| \frac{\partial B}{\partial s} \right| \ll 1. \quad (3.40)$$

Setting $\xi = 0.1$ and estimating $\partial B/\partial s \sim B/R$ where R is the bending radius (assuming $R=200 \text{ mm}$ practical for the CSR space limitation) the field B estimation is

$$B = 10 \frac{2\pi}{qR} \sqrt{2Em}, \quad (3.41)$$

as shown in fig. 3.21. This is the strongest requirement on the magnetic field magnitude so far. Unlike the previous two requirements where only the averaged magnitude of the magnetic field is important, the adiabaticity depends on local properties of the trajectory and thus must not be violated even in a single point on the track where the

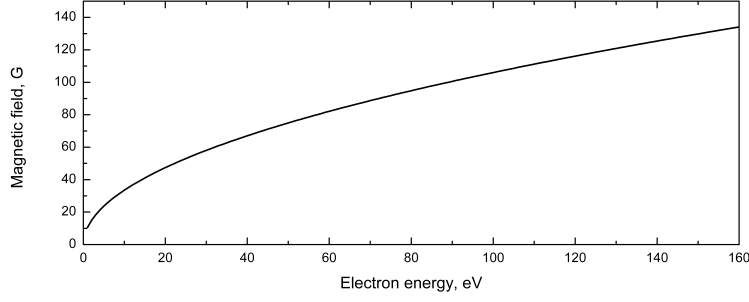


Figure 3.21: Guiding magnetic field providing an adiabatic transport as a function of the electron energy.

electron beam experiences a sharp bend. Therefore the adiabaticity parameter must be checked in a complete numerical field model by particle tracking, as described later in this chapter. As a summary of this subsection one can say that the guiding magnetic field sufficient for adiabatic transport of high quality electron beam is about 120 Gauss for 160 eV electron beams, and as low as 30-50 Gauss for the heavy ions cooled at much lower electron energies of about 10 eV.

The *upper* limit on the magnetic field strength for the CSR application is defined mainly by distortions of the *ion* beam caused by the magnetic field in the merging regions. Preliminary design studies done before this work by Fadil [78] showed that a generic toroidal merging scheme, with discrete coils letting the ion beam pass through a gap between coils, is inadequate for the CSR. In a toroidal field the field strength has a gradient inversely proportional to the radius such that

$$B(R) = \frac{B_0 R_0}{R}, \quad (3.42)$$

where B_0 is the field on the central toroid radius R_0 and

$$R = \frac{R_0 - x}{\cos \phi} \quad \text{so} \quad B_{\perp} = \frac{B_0 R_0}{R_0 - x} \cos \phi \sin \phi. \quad (3.43)$$

Then the deflection angle $\delta(x)$ of an ion as a function of the transverse coordinate is

$$\delta(x) = \frac{p_{\perp}}{p} = \frac{\int q \vec{v} \times \vec{B} dt}{p} = \frac{\int q v B_{\perp} dt}{p}. \quad (3.44)$$

Using eq. 3.43 and

$$\phi(t) = \arctan\left(\frac{R_{max} \sin \phi_{max} - vt}{R_0 - x}\right) \rightarrow dt = \frac{-(R_0 - x_0)}{v} \frac{d\phi}{\cos^2 \phi} \quad (3.45)$$

the deflection along a particle track can be integrated in eq. 3.44 and one gets $\delta(x)$ as

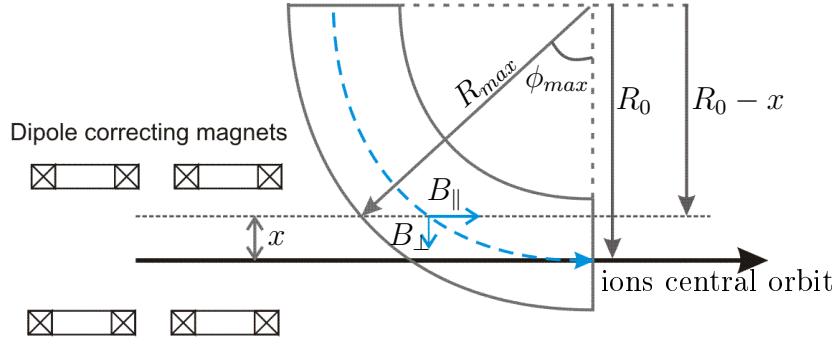


Figure 3.22: Influence of the toroidal field on ions.

a function of transverse coordinate (see fig.3.22)

$$\begin{aligned} \delta(x) &= \frac{qB_0R_0}{p} \int_{\phi_{max}}^0 \frac{-\cos \phi \sin \phi d\phi}{\cos^2 \phi} = \frac{qB_0R_0}{p} \int_{\phi_{max}}^0 \frac{d \cos \phi}{\cos \phi} = -\frac{qB_0R_0}{p} \ln \cos \phi_{max} \\ &= -\frac{qB_0R_0}{p} \ln \frac{R_0-x}{R_{max}} = -\frac{qB_0R_0}{p} \left(\ln \frac{R_0}{R_{max}} - \frac{x}{R_0} + O(x^2) + \dots \right) \end{aligned} \quad (3.46)$$

Such a deflection is inevitable in devices relying on toroidal merging of the beams. As a common practice to compensate both angle and coordinate mismatch two pairs of dipole correcting magnets are installed before and after the toroidal merging region (see fig. 3.22). But a uniform dipole field compensates only the term of order $n = 0$ in the x^n dependence of $\delta(x)$ (eq. 3.4.3) whereas the $n = 1$ and higher order terms cannot practically be compensated. In case of the CSR the deflection gets more prominent because the $n = 1$ term rises due to the low ion momentum p and small bending radius R_0 which is comparable to the beam width. The contribution of the $n = 1$ term was shown to cause significant beam distortions, making it impossible to store the lightest ions [78]. To solve this problem, a new toroid-free merging scheme has been proposed [78]. In this scheme, discussed in more details later, the bending of the electron beam and the merging process are separated. The electron beam is launched perpendicular to the ion beam in a plane elevated above the ion orbit plane. Then the electron beam is bent by a toroidal field in a screened volume such that the ions do not interact with the curved field. After this toroidal bending the electron and ion beams are parallel to each other. The parallel beams are merged in a field created by a horizontal solenoid and a set of coils producing a vertical field component. Such geometry provides a B_{\perp} with respect to the ion beam direction which is better suited for compensation than a toroidal field as it is more uniform.

The theoretical calculations of the cooling times assume the mean ion and electron velocities are equal. In the real apparatus however the electrons follow the magnetic field lines, while the ions are affected only by the merging field, and are either not deflected if they have a position close to the central orbit, or get a minor deflection due to the field inhomogeneity. In order to achieve proper velocity matching, the guiding field in the interaction region must be parallel to the ion beam axis with a certain

accuracy for the entire volume occupied by the electron beam. A practical criterion for the field tolerance is that the ratio of the transverse field to the longitudinal field B_{\perp}/B_{\parallel} must be less than the angular divergence of the ion beam due to betatron oscillations (1)

$$\frac{B_{\perp}}{B_{\parallel}} \leq \sqrt{\frac{\varepsilon_{x,y}}{\beta_{x,y}}} \approx 10^{-2} \quad (3.47)$$

and less than the divergence of the electron beam due to its transverse temperature.

$$\frac{B_{\perp}}{B_{\parallel}} \leq \sqrt{\frac{k_B T_{e\perp}}{E}} \approx 1.7 \times 10^{-3}. \quad (3.48)$$

3.4.4 Model of the optics

To proceed with the design, a 3D field model of the CSR electron cooler has been created and analyzed by means of the finite element analysis (FEA) software package Opera-3D by Vector Fields Software (Cobham CTS Limited). The purpose of the numerical simulations was to elaborate magnet geometries providing the magnetic field of strength and quality specified in this chapter and which fit, with all their components, into a 2600 mm long 800×800 mm² CSR linear chamber. The conductor geometries resulting from the model were used later to prototype first magnets and specify the requirements of auxiliary equipment such as the cooling system for the magnets.

The schematic view of the model is shown in fig. 3.23. The coils are shown in red, the magnetic screens in light green, the dark green area is the high resolution volume outside of the cooler included to track the ion beam in an extended region. The electron track is shown in black (b, later in this section indexing according to fig. 3.23) and the ion track in blue (c). Only half of the cooler was simulated in order to reduce the problem domain. The central plane (i) is set to normal magnetic field conditions $\vec{B} \times \vec{n} = 0$ where \vec{n} is the unit vector normal to the surface. As active elements the model includes a set of conductors and iron magnetic shields represented as 2-mm sheets of material with non-linear magnetic properties governed by the B vs. H curve of soft magnetic, SS400-grade steel. The background volume was created by requiring a tangential field boundary condition $\vec{B} \cdot \vec{n} = 0$ at the box outer surface lying 200-300 mm outside of the magnetic shields. The key ideas of the model are: use of toroid-free merging as described above, minimization of stray fields affecting the ions and use of the weakest possible magnetic fields.

In the following we outline the different elements of the magnetic optics along the flight path of the electron beam (see fig. 3.23). The electron beam starts at the cathode outside of the cryostat chamber and is guided in direction perpendicular to the ion beam in a plane elevated by 140 mm above the plane of the closed ion orbit in the ring. Then the electron beam (b), after acceleration and expansion, enters the transition section (a), where warm water-cooled magnets from the outside of the cryostat join the cryogenic magnets. This is the first part present in the model. The transition section is

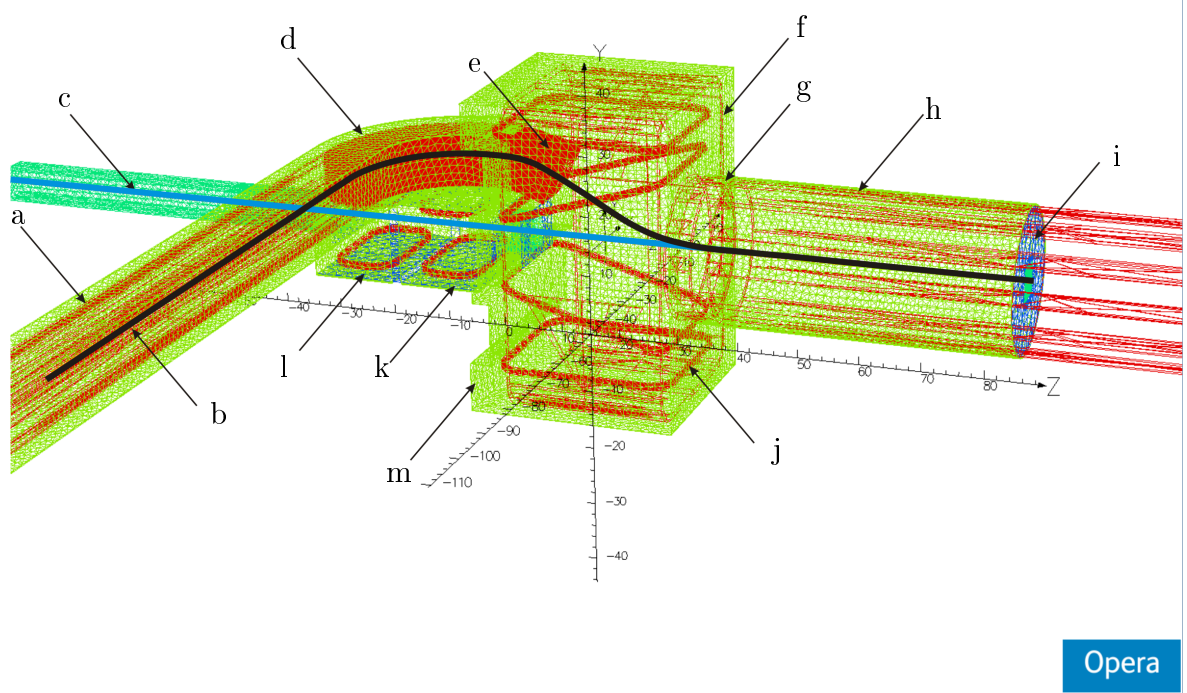


Figure 3.23: The optics of the electron cooler. Dimensions of the coordinate system is in cm, zero point is on the intersection of the ion axis and the vertical axis of the merging box. a) Transition region, b) black line - electron beam, c) blue line - the ion beam d) horizontal 90° toroid (toroidal solenoid horizontal - TSH) and toroidal arc compensators (TAC), e) 30° toroidal section (toroidal solenoid vertical - TSV), f) rectangular solenoid (RS) around the merging box, g) gap in the main solenoid for beam scrapers, h) main solenoid (MS) i) symmetry plane of the cooler, j) one of the 4 coils (MV) producing vertical field component in the merging box, k) second compensator pair (Comp2), l) first compensator pair (Comp1), m) shielded return of the lowest MV coil.

artificially elongated in the model to provide a highly parallel field as a start region for test particles and suppress fringe fields near the ion track (c). The next section is the 90° toroid (d) in the horizontal plane (toroidal solenoid horizontal - TSH) where the electron beam is bent to become parallel to the ion beam. The toroid is modeled as 84 discrete turns uniformly filling the arc length. The central bending radius of the toroid is $R = 200$ mm. Both the transition and the toroid sections are completely shielded by soft iron screens to provide a return path for the magnetic flux and minimize the stray field seen by the ions. This screen then joins the shielding box entirely surrounding the merging and interaction region.

Due to the field gradient in the toroidal section the electron beam is experiencing a drift motion with a drift velocity perpendicular to the bending plane equal to $v_d = mv^2/eRB$ [79] where v is the electron velocity and B the guiding field. To compensate the drift motion, two arc conductors (TAC) are placed in the toroidal section between the toroid turns and the electron beam line in planes above and below the electron beam axis. These coils provide a weak vertical field $B_\perp = mv/eR$ (which in the real setup will be provided by one of the steerer coils).

The next optical group on the electron track is a vertical 30° toroidal section (e, toroidal solenoid vertical - TSV) tilting the electron beam downwards. The purpose of this section is to provide a smooth junction of the two field regions. This vertical toroidal section is already inside of the iron cast and is not shielded separately. In this region, a lowering of the magnetic field takes place. Since the strongest limitation on the magnetic field originates from the adiabaticity condition in the bending toroids, the field strength downstream of the 90° horizontal toroid is lowered by a factor of 2. Hereafter, to keep consistence, the field magnitude always refers to the magnitude of the *toroidal field* although the actual field strength in the main solenoid (h) is lower.

The field in the merging region between the 30° toroid and the main solenoid is created by a superposition of the longitudinal field component produced by a rectangular 330×540 mm solenoid RS (f) surrounding the entire merging section over 290 mm length and a vertical component of the field produced by 4 coils (j) denoted as “merging vertical” (MV). The latter are placed inside of the RS and each consists of two racetrack-shaped conductors, which in the model represent a single coil with two parallel winding stacks. The MV coils are placed symmetrically in relation to the ion beam axis and the two inner coils are tilted by 17° to let the vacuum flange of the ion beam line pass through. On the back side of the merging box, the MV coils have shielded returns (m) to confine the magnetic flux and avoid disturbance of the ion and electron beams by the vertical field of the opposite direction outside of the coils area.

After the merging box, the electron beam enters the interaction region where the magnetic field is created by the main solenoid MS (h) of 1060 mm length and 240 mm inner diameter. It has 34 mm gaps (g) close to its entrance and exit. These gaps separate additional 47-mm-long parts of the solenoid on each side. The purpose of the

gaps is to provide access for rotational feedthroughs driving the beam scrapers foreseen for electron and ion beam diagnostics and other mechanical connections. The position for the scrapers is chosen such that electron and ion beams are already well merged and parallel to each other and the scraper can scan the ion beam as well as the electron to measure the beam overlap.

Separated from the electron track, two pairs of compensators (k,l) are placed in front of the merging region. The first pair (l) deflects the ion beam into the same direction as the vertical component of the merging field to create a position shift. The second pair (k) bends the beam into the opposite direction. If the correction fields are chosen correctly, they cancel the deflection caused by the merging field and the ion beam enters the interaction region on-axis and parallel to it (illustrated later in fig. 3.26).

The vertical positions of all coils are chosen to provide enough space for practical realization of the magnets and for the necessary thermal isolation layers between the beam line and magnets for cryogenic and room temperature operation, as well as during the bakeout of the ring. The longitudinal positions of the compensators have been chosen such that the last pair is as close to the merging box as possible to minimize the position deflection to be compensated and thus reduce the amperage of the magnets. The distance between the pairs is also minimized in order to have maximal space available for the interaction section. Both pairs have separate shields to minimize coupling of the magnets (among each other) and far-range stray fields. The model includes space for internal infrastructure and connections, which affects the field geometry. The main purpose of the modeling was to test whether this realistic field geometry can fulfill the specifications concerning adiabatic electron transport, compensation of the ion beam distortion and mutual influence of the magnets. The results are reported in the next section.

3.4.5 Field quality and tracking

In this section we evaluate the quality of the magnetic field produced by the optical system and the ion and electron transport provided by it.

Field quality. According to the field quality criteria 3.47 and 3.48, established in section 3.4.3 we can define which part of the interaction region provides a field fulfilling these conditions. The total length of the main solenoid is 1060 mm, continued on both sides by the 34 mm gap and the split-off 47 mm section of the same winding density. However not the entire length can be considered as a “good field” region, where electron cooling can be successfully performed. The region of good field can be estimated as 70 cm for the complete cooler using the following criterion: The ratio B_{\perp}/B_z must be below 2×10^{-3} locally and the averaged value of the field divergence $\gamma = \int \frac{\sqrt{B_x^2 + B_y^2}}{B_z} dl / L$ must be lower than 1.0 mrad within the cross-section area of the electron beam which

has a radius of 6.7 mm (see fig. 3.24a). If a local divergence up to 3 mrad (acceptable for low cooling energies) is tolerable, then a region of 80 cm length with averaged γ less than 1.3 mrad (see fig. 3.24b) is the “good field” region. Both parameters are close to the L_{ring}/L_{cooler} ratio of 50 used for the cooling time calculation in section 3.4.2

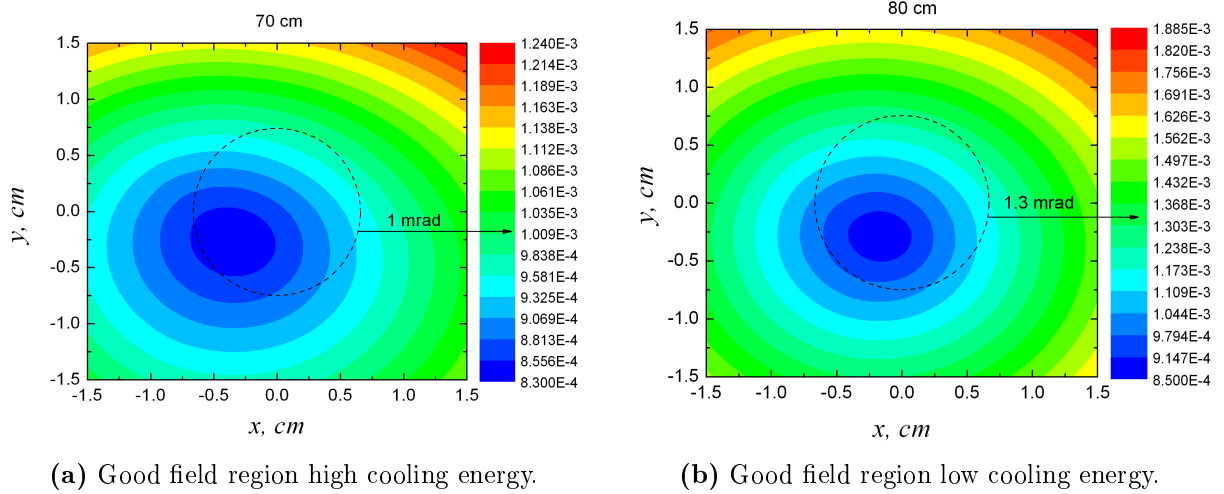


Figure 3.24: Weighted divergence of the magnetic field $\gamma = \int \frac{\sqrt{B_x^2 + B_y^2}}{B_z} dl / L$ in the plane perpendicular to the ion beam, the electron beam of 6.7 mm radius is shown by dashed circles.

Electron tracking. The next parameter to be defined using the field model is the appropriate scaling of the guiding field as a function of the electron energy. The search of the limiting field strength has been performed in the following way. An electron test particle of given energy was launched parallel to the axis with negligible transverse energy in the transition region 60 cm before the horizontal toroid, where $B_{\perp}/B_{\parallel} \sim 5 \times 10^{-5}$. The particle tracks were calculated with a step length of 1 mm. With properly-set toroidal compensation and settings of the MV magnets the beam, axially launched from the transition region, arrives matching to the vertical axis of the interaction region and has a horizontal shift of about 1 mm to the outside of the ring if no horizontal steering in the toroid is applied. The magnetic field was measured at each point of the track. The particle velocity was decomposed into components parallel (v_{\parallel}) and perpendicular (v_{\perp}) to the field at each point on the track, so that $\vec{v}_{\parallel} = \vec{B}(\vec{v}\vec{B})/|B|^2$ and $\vec{v}_{\perp} = \vec{v} - \vec{v}_{\parallel}$. The energy of the motion perpendicular to the local field is denoted as the transverse energy. To eliminate the influence of the phase, the transverse energy was averaged over 20 cm distance in the interaction region. For a constant guiding field strength, changing only the magnetic field strength of the toroidal compensators, a set of particle tracks of varying energies was calculated.

As expected, the transverse energy remained negligible until the particle energy reached a critical value for a given guiding field strength (see fig. 3.25). Exceeding this threshold energy causes exponentially fast transverse heating of the beam by transfer of energy from the longitudinal motion into transverse while bending the beam. From

the form of the adiabaticity criterion $\xi = \frac{\lambda_L}{B} \left| \frac{\partial B}{\partial s} \right| \ll 1$, where $\lambda_L = v_{\parallel} m_e / eB \propto \sqrt{E}/B$, if the guiding field B is scaled with a factor of a then the critical energy corresponding to the same value of ξ scales with a^2 . One can see this by comparing fig. 3.25a and fig. 3.25b. For the simulated geometry, the scaling rule for the critical energy can be defined as

$$E_C = 22 \left(\frac{B[G]}{32} \right)^2 [\text{eV}] . \quad (3.49)$$

The rule is aimed to define the field strength B_{max} corresponding to the maximum electron energy of 1 keV. $B_{max} = 215$, this value will be later used as the upper field limit for the realization of the magnets in section 4.1.2.

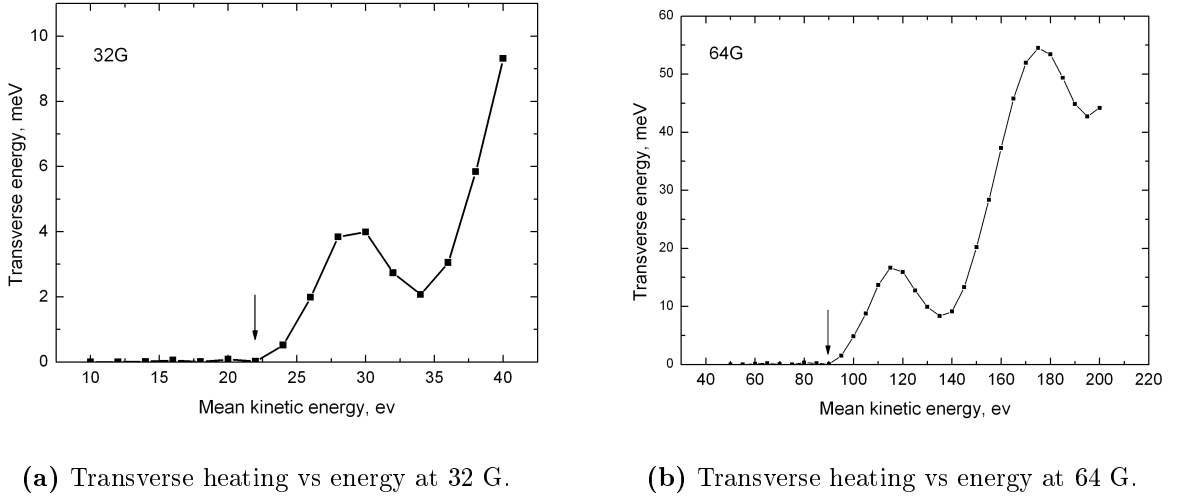


Figure 3.25: Transverse electron temperature as a function of the mean electron kinetic energy for guiding field in toroid region equal to 32 (3.25a) and 64 Gauss (3.25b), the critical energy E_C is indicated by arrows.

Ion tracking. Knowing the required B values we can see how the field necessary to provide a cold electron beam of a certain energy affects ion species of a given mass, assuming the electron energy for cooling this ion at an energy of 300 keV. The worst-case scenario is the cooling of protons. At high cooling energy, corresponding to the lightest species, a high guiding field is required. In addition, the light ions are more susceptible to the magnetic field. Thus, we take the proton beam as the most vivid illustration of the interaction between the ion beam and the guiding field. First of all let us take a look at the ion beam dynamics in the absence of correction elements. The beam entering the merging box experiences deflection by the vertical component B_0 of the merging field in the horizontal plane (see fig. 3.26, trajectory B). Assuming the deflection to be small, the angle and the shift are given by

$$\alpha = \frac{p_{\perp}}{p_{\parallel}} = \frac{eZ \int_{-\infty}^{+\infty} B_0(s) ds}{M_i} \text{ and} \quad (3.50)$$

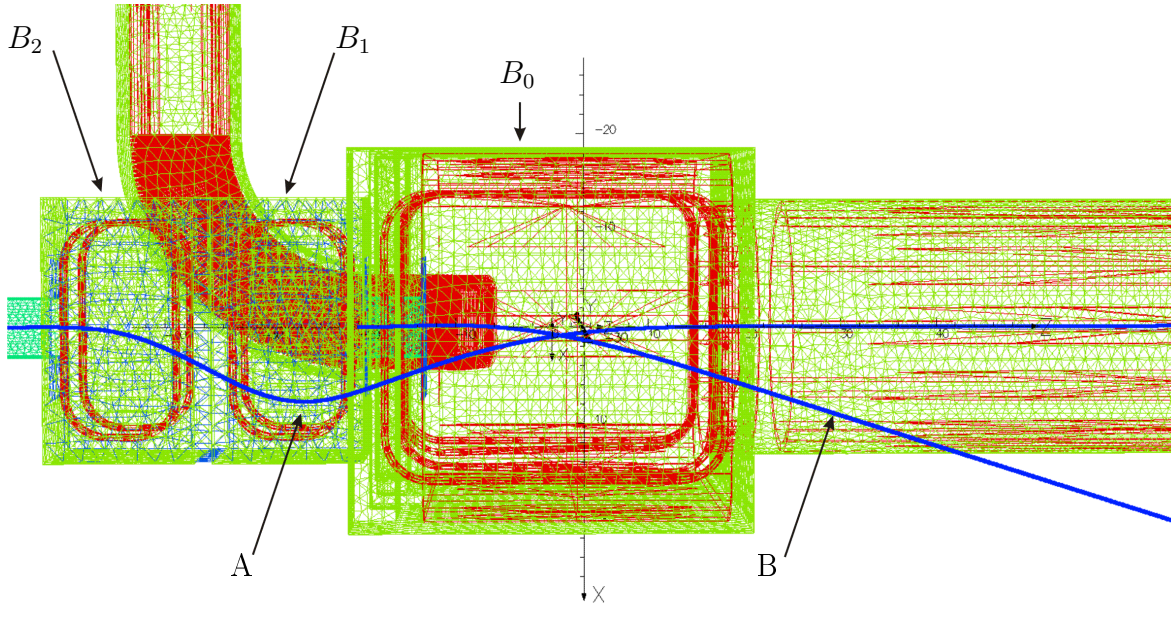


Figure 3.26: Trajectory of 300 keV proton beam in the 100 G equivalent field. Note that the amplitudes of transverse motion are magnified by a factor of 50. A - compensated beam. B - a paraxial beam entered the merging box under zero angle.

$$\Delta x = \int_{-\infty}^{+\infty} \frac{eZds'}{M_i v_{\parallel}} \int_{-\infty}^{s'} B_0(s) ds. \quad (3.51)$$

This yields the angle and the position mismatch at which the ion beam would enter the interaction region without correction (see fig. 3.26). Apart from compromising cooling performance and experimental results, an inclined beam not parallel to the field axis in the interaction region is also affected by the solenoidal field present there: the horizontal deflection gets transferred into a vertical one with no compensation available. Strong deflections causing coupling of vertical and horizontal motions are dangerous for the storage ring acceptance.

To eliminate both, deflection and position mismatch, one needs to introduce two pairs of dipole compensators before the merging box and two other after demerging. Having two distinct correctors, producing fields $B_1(s)$ and $B_2(s)$, one can find scaling factors A and C such that

$$\int_{-\infty}^{+\infty} B_0(s) + AB_1(s) + CB_2(s) ds = 0 \text{ and} \quad (3.52)$$

$$\int_{-\infty}^{+\infty} ds' \int_{-\infty}^{s'} B_0 + AB_1(s) + CB_2(s)(s) ds = 0, \quad (3.53)$$

which gives two linear equations. Perfect compensation is possible only for a single trajectory while for all trajectories having different coordinates in the plane perpendicular to the beam axis, these values of A and C give only partial compensation. As mentioned in section 3.4.3, in a toroidal merging field and with dipole compensators, the residual uncompensated deflection was unacceptable to conserve the ring accep-

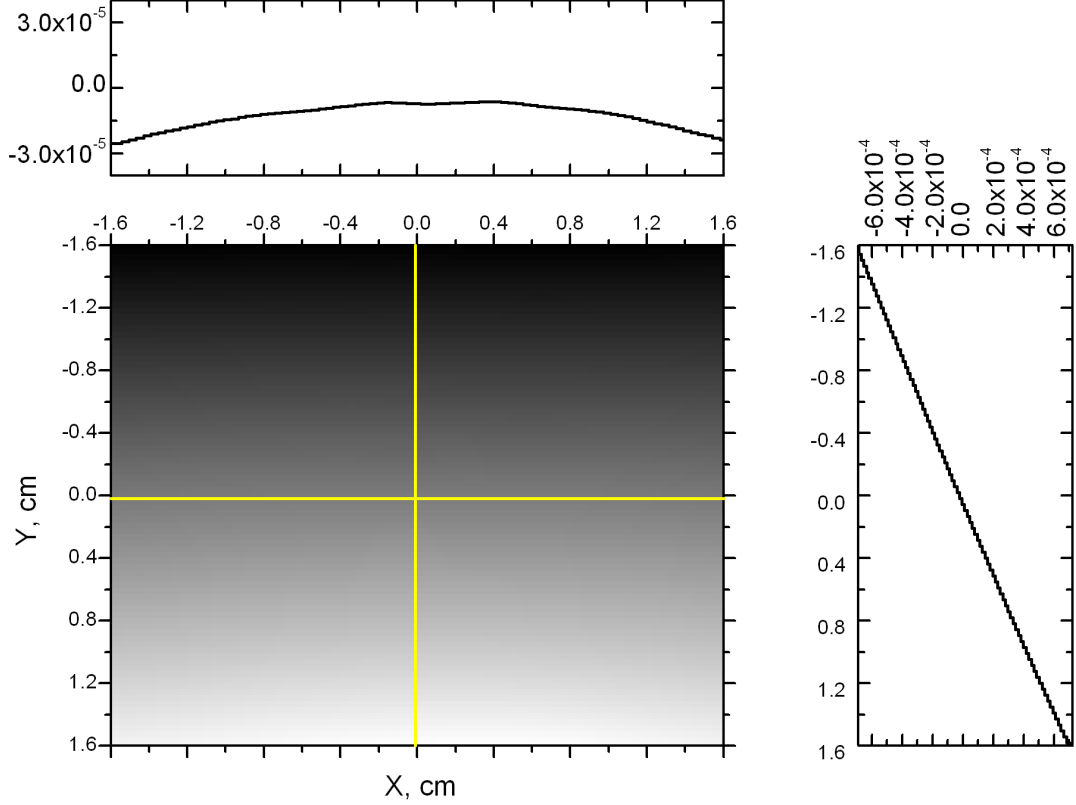


Figure 3.27: Angular spread of 300 keV proton beam in the middle of the interaction region in 100 G equivalent field.

tance for the lightest species. In the toroidal merging scheme at the CSR geometry the uncompensated field gradient in the toroid causes a vertical deflection [78]. Depending on the ion position relative to the beam axis in the horizontal plane, the deflection angle for a 300 keV proton in a 30 G magnetic field would change with a dispersion of 0.11 mrad per 1 mm distance from the beam axis. This yields a spreading parameter of 3.6×10^{-3} mrad/mm·G for the toroidal merging scheme.

In the toroid-free merging scheme the electron beam is approaching the ion beam not in the horizontal, but in the vertical plane. The field homogeneity along the horizontal axis perpendicular to the beam is much better than in the toroidal merging and, correspondingly, the field geometry is better compatible with the dipole compensators. Thus it is possible to compensate ions at different displacements from the horizontal axis almost equally. One can see in fig. 3.27 the deflection of 300 keV protons in the equivalent field of 100 G (sufficient for the electron transport at the corresponding cooling energy). The deflection changes along the horizontal axis from zero to 3×10^{-5} rad over 16 mm distance from the beam axis. This corresponds to a spreading parameter of 1.8×10^{-5} mrad/mm·G, two orders of magnitude better than in case of toroidal merging. The toroid-free merging is, however, not ideal. There is a field gradient depending on vertical position relative to the beam axis. As one can see in fig. 3.27 this gradient causes an angular spread of the ions scaling for protons as 3.75×10^{-4} mrad/mm·G.

This vertical spreading parameter is about 10 times lower than that in the toroidal merging scheme for the horizontal plane. In addition the vertical dispersion is less harmful to the beam as the ring acceptance at the relevant position is smaller in the vertical plane (± 14 mm) than in the horizontal plane (± 40 mm). Therefore the stored ions have positions closer to the axis in the vertical plane, than in the horizontal and the influence of the dispersion is less prominent.

The value of the angular spread of the ion beam in the toroid-free merging scheme is below the limits imposed by the divergence of the electron beam, so it should not affect the cooling performance. The deflection of the ion position in the middle of the interaction section for 300 keV protons and for a vertical position deviation within ± 16 mm amounts to ± 0.6 mm. For any higher mass compared to a proton, the magnetic field induced effects further reduce by a factor of $m_p q / 2M_i e$ since the required field strength is about 50 Gauss (enough to suppress TLR which defines the minimum magnetic field for cooling of heaviest ions). Thus, beam distortion due to magnetic deflection in the toroid-free scheme is within tolerable limits for all species, slightly affecting the experimental conditions for protons only.

3.5 Summary

In this chapter we have started from the basic parameters of the electron beam produced by the existing cryogenic photocathode electron source of the TSR electron target. We have demonstrated experimentally that an ultra-low energy electron beam can be realized using this electron source. In the beam deceleration experiments the density of the electron beam defined by its perveance was increased by an order of magnitude to make it sufficient for electron cooling at ultra-low energies. We have shown that efficient phase space cooling will be possible at the achieved values of electron density and temperatures. Finally we established a layout of the magnetic guiding system for the ultra-low energy electron beam that will be compatible with all conditions at the CSR. The next chapter will focus on the practical aspects of the developed magnetic guiding scheme. The general electron cooler design will be considered, emphasizing the mechanical realization of the magnets and the cryogenic operation of the system.

Chapter 4

Realization of the CSR electron cooler

4.1 Magnets design and construction

The previous chapter laid out the magnetic guiding field geometry necessary for the CSR experimental conditions. In this chapter we elaborate a design concept to realize this magnetic system. The mechanical and the field designs are not independent of each other, therefore the requirements of mechanical feasibility were partly already included in the phase of field modeling. The detailed mechanical design of the magnets also depends on conditions associated with vacuum and cryogenic operation as well as space limitations, work safety and construction costs.

4.1.1 Environment and general design concept

The CSR is a two-layer vacuum system (see sec. 2.1.2) with a 10^{-6} mbar vacuum cryostat surrounding the XHV beam line. One can see the cryostat chambers of the ring in fig. 4.1. The missing linear chamber in the middle of the picture will house the electron cooler and will be reintegrated into the ring when most of the internal components are built in.

All four linear chambers of the outer layer have the same design. Modifications are introduced during construction of the CSR by customizing the available flanges and mounting options to the needs of particular applications. The linear section offers a variety of flange sizes, providing flexibility in the construction of the inner parts of the cryostat and the various feedthroughs to the atmosphere (see fig. 4.2).

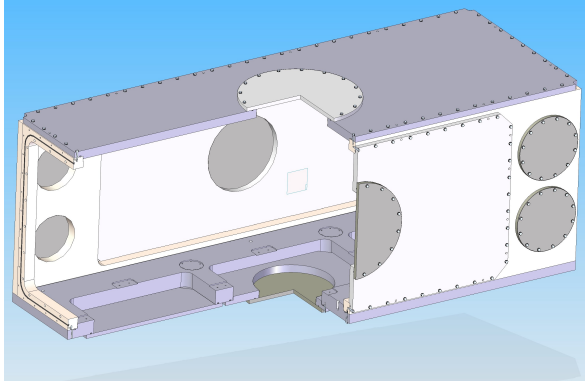
The magnetic system must surround the XHV beam lines in the cryostat volume. Therefore the materials and technologies used must comply with high-vacuum requirements. Since the magnets must stay close to the beam lines due to space limitations, it is important to manage heat emission resulting from magnet operation. Depending on whether the magnets are resistive or superconductive, this includes either Joule heat plus heat leaks through the current leads (resistive magnets) or heat leaks only (superconductive). The 40 K and 80 K thermal shields of the beam line require significant



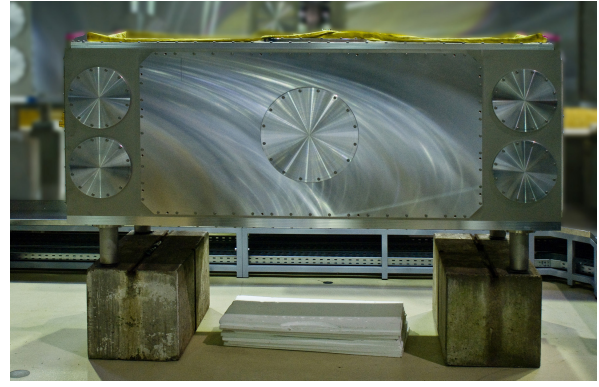
Figure 4.1: The CSR outer vacuum construction, the gap between the corner in the left and the rest of the ring in the yellow frame is the foreseen cooler position.

space. Therefore due to the space limitations, the magnets can be build only inside of them. Such an arrangement also allows to use magnetic shields as a mechanical support of adjacent thermal screens. The magnets operated inside of the 40 K thermal zone should have an operation temperature close to this value to avoid additional loads on the cooling system and complicated thermal decoupling of supporting structures. The general concept is to use cryogenic magnets operated at ~ 40 K and enclose them in a multilayer structure providing magnetic and thermal shielding of the interior. The magnets must be thermally isolated from the beam pipe to protect them from radiative heating during the beam line bakeout and in the case of RT operation. Multilayer floating isolation based on glass fiber and aluminum foil is bakeable up to 400°C and can serve for both high temperature and cryogenic isolation. The details of the XHV line construction are beyond the scope of this work. However, a preliminary design study has been taken into account in the layout of the magnet geometry. One can see the early design concept of the beam line in fig. 4.3. Later this early concept was reworked at the design office mainly by chief MPIK designer T. Weber. The detailed design of the merging section is described and discussed later in this section.

The electron cooler section is on both sides joined by vacuum chambers housing electrostatic quadrupole doublets (see fig. 2.1). Thus, the already limited vacuum conductance of the cooler section is reduced even further by these quadrupole electrodes and their housings, which obscure a significant part of the beam line cross-section. Moreover, unlike the other linear sections of the CSR, the cooler has direct connections between the cryogenic XHV beam line and the warm UHV electron gun and collector sections. Therefore the cooler section vacuum system cannot rely on pumping by the neighboring CSR pumping facilities, but must include its own 2 K cryocondensation



(a) A cut of the chamber as a 3-d model



(b) The chamber of the electron cooler

Figure 4.2: The model, and realized linear chamber for the electron cooler showing a variety of options to bring the outside infrastructure in contact with the inside environment by use of ISO-K 250 side flanges (4 on each side) side and bottom ISO-K 400, top ISO-K 500, as well as by means of front and back doors of 800×800 mm, the side doors of 800×1700 mm, and the three bottom 500×700 hatches.

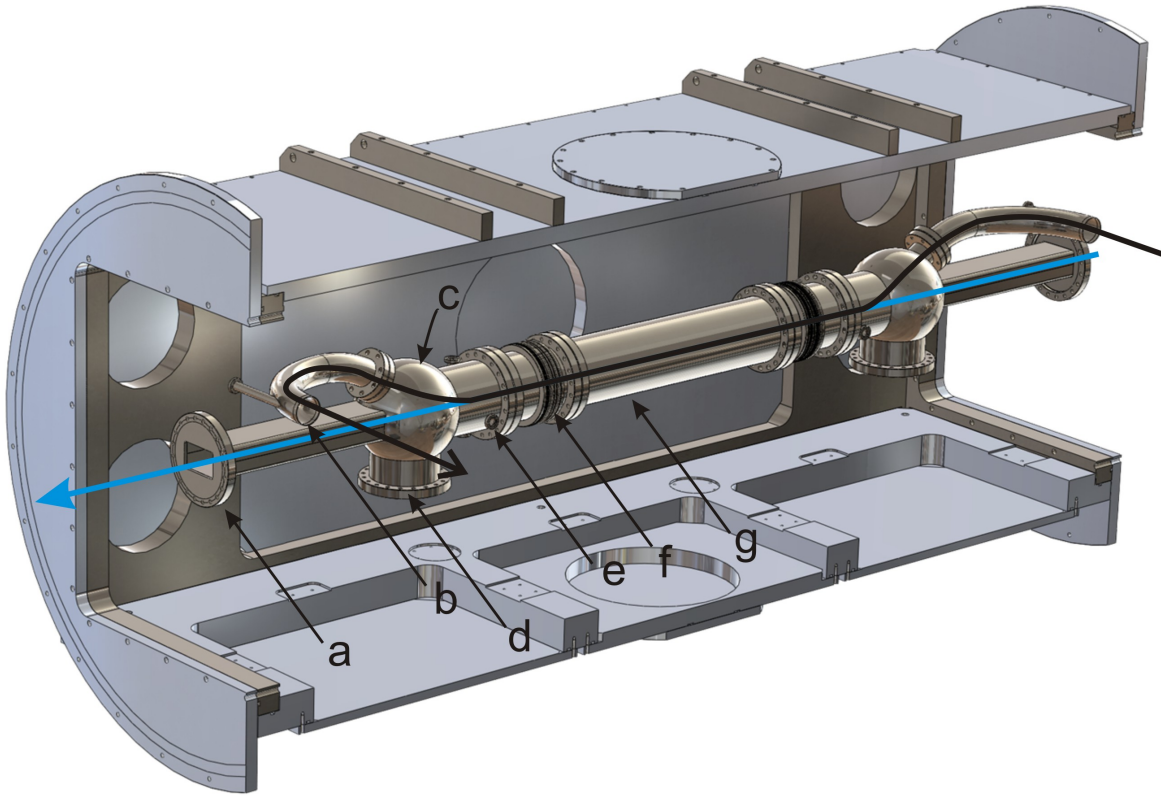


Figure 4.3: Preliminary design of the XHV beam line in the cooler section. The section on both ends is connected by 150 mm Helicoflex flanges (a) to the neighboring quadrupole sections further continued by rectangular vacuum ducts, through which the ion beam (blue line) reaches the merging chamber (c), the electron beam (black line) arrives to the merging chamber and leaves the separation chamber through the toroid tube bent in two dimensions (b). The merging chambers have large bottom flanges (d) to mount the 2 K cryoadsorption units. Between the merging chamber (c) and the interaction chamber (g) a rotating beam scraper driven by a mechanical feedthrough (e) is foreseen. The three main parts of the vacuum system (merging, interaction, separation) are mechanically decoupled from each other by means of the edge welded bellow sections (f) to compensate thermal shrinking of the chambers and enable their independent support.

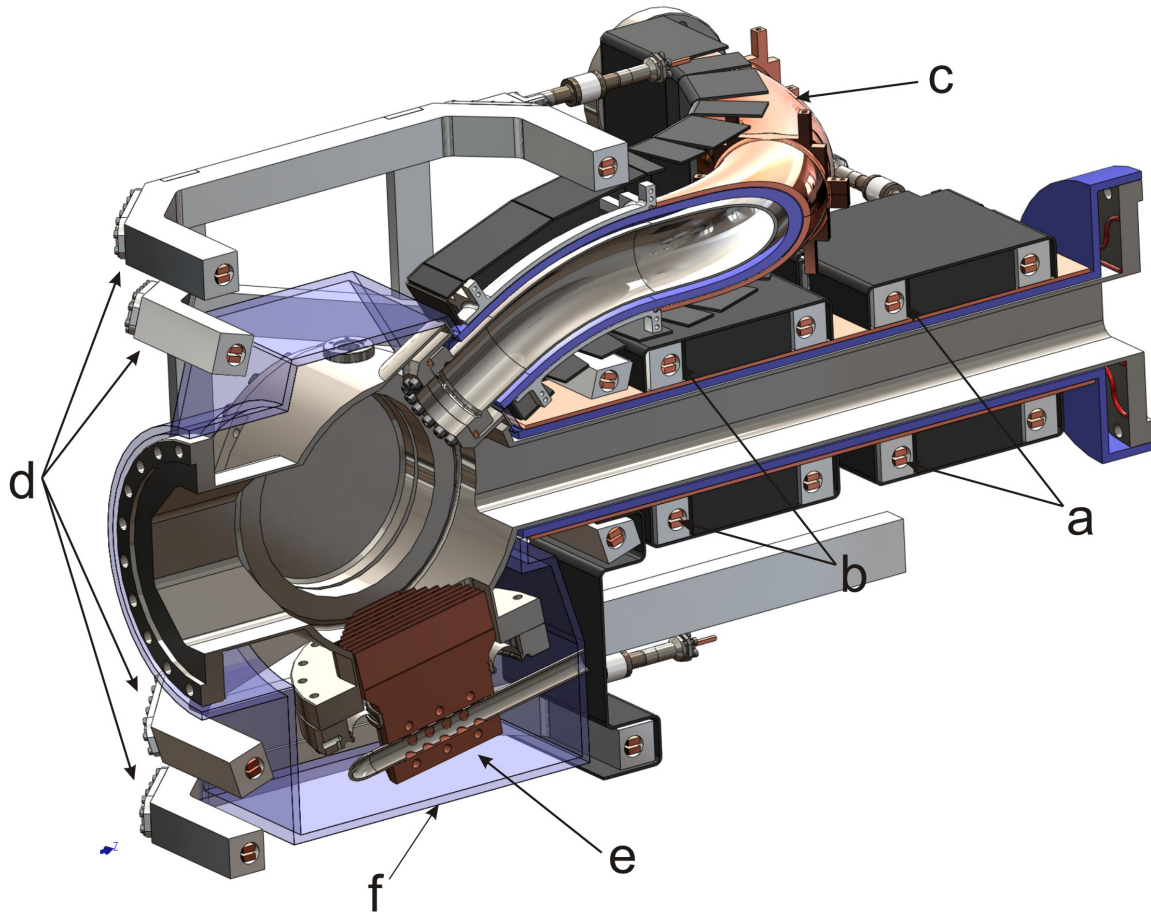


Figure 4.4: Layout of the CSR merging chamber showing the magnets arrangement around the merging chamber. a) Comp1 coils, b) Comp2 coils, c) thermally conductive support for the toroidal solenoids TSH, TSV d) MV coils e) 2 K cryocondensation unit, f) bakeable thermoinsulation.

units for cold operation and cryopumps for the RT mode. These units will be mounted on dedicated vacuum flanges of 150 mm diameter. The volume enclosed by the magnets must be spacious enough to fit these pumping units and their cryogen supplies. The vacuum chambers of the beam merging regions, on the junction of the electron and the ion beam lines demand for significant volume anyway, are thus ideal location for the pumps. It is also important that the pumping surfaces are placed close to the outlet of the electron beam line where significant gas load arrives from the room temperature UHV vacuum chambers outside of the cryostat. The general layout of the beam lines in the merging section, including the MV, TSH, TSV and Comp magnets is shown in fig. 4.4

The mechanical layout of this section is as follows. The merging region is connected to the quadrupole chambers by a $60 \times 100 \text{ mm}^2$ rectangular duct with correction coils placed on top and underneath of it. A 2 cm gap between the duct and the coils in the vertical direction allows to wrap thermal isolation and heating elements on the duct. The electron track is formed by a $\varnothing 50 \text{ mm}$ tube bent in two planes to follow the electron track and connected to the merging chamber by means of an inversed Helicoflex flange. The merging chamber features an inclined bottom flange to mount

a 2 K cryocondensation pump and two side flanges. One of the latter is used for a cryopump while the other one provides mounting access and houses NEG modules. The transition to the interaction region is made by an octagonal protrusion terminated by a \varnothing 150 Helicoflex flange. Some smaller flanges are placed on the merging chamber for the electric feedthroughs for drift tubes and NEG modules. Rotational feedthroughs driving the beam scrapers will be placed on the octagonal protrusion. The vacuum system of the interaction region is made of a \varnothing 150 mm tube with edge-welded bellow sections on both sides to compensate the thermal shrinking of the beam line (by 7.8 mm for the entire cooler section). The merging sections and the interaction segment are supported independent of each other by thermally decoupled support structures from below. The magnet system rests on its own support independent of the chambers.

As already mentioned, one of the key points for the magnet design is their cryogenic operation. Depending on geometry and amperage of a particular magnet it can be realized in different ways. We will investigate the optimal realization options in the next section on the basis of magnet parameters used in the field simulation.

4.1.2 Magnets data

In this section we will summarize the technical data of the conductors present in the field model. The parameters of interest are the dimensions and the number of ampere-turns required to produce the field. One additional remark needs to be done before we specify the amperage of the coils. In the previous section 3.4.4 the field geometry has been developed to provide the electron beam of energies required to cool ion beams of 1-160 a.m.u. mass. The magnets however must be designed to be also suitable for operation of the electron beam as a projectile in electron impact ionization experiments. This high energy operation mode however sets the upper limit of the coils field. For the proposed electron energy of up to 1 keV, using the scaling rule 3.49 we can establish the maximum magnetic field of 215 Gauss to which all the conductors in the model need to be scaled. The magnet properties are summarized in table 4.1.

Table 4.1: Parameters of the CSR electron cooler magnets for the complete assembly at 215 G nominal field for 1 keV electrons. Naming MS - main solenoid, RS - rectangular solenoid, MV - merging vertical coil, TSH - toroidal solenoid horizontal, TSV toroidal solenoid vertical, TAC - toroidal arc compensator, Comp1 - compensator one, Comp2 - compensator two. The naming is explained in fig. 4.4 and fig. 3.23.

Name	Amperage, AT	Length per turn, m	Comments
MS	9111.3	0.75	main section and two 47 mm end pieces
RS	4223.5	1.67	two sections
MV	5232.6	1.10	8 coils
TSH	10999.2	0.29	horizontal part, two sections 84 coils each
TSV	1836.0	0.29	vertical part, two sections 30 coils each
TAC	98.9184	0.77	2 loops on each side
Comp1	4741.0	0.57	2 coils on each side
Comp2	7680.7	0.57	2 coils on each side

4.1.3 Magnet realization

Using the numbers from table 4.1 we can now consider realization of the magnets. As the produced fields and required currents are moderate, the magnets can be both superconductive or resistive. For the temperature and field range of interest the superconductive option assumes the use of high temperature superconductor (HTS) composite wires. For the resistive magnets, wire bar copper of 164 p.p.m. purity is well suited for temperatures of about 40 K, where commercial cold-heads can provide significant cooling power and one would profit from the large decrease of copper resistivity with temperature (see fig. 4.5).

Each option has its advantages. Resistive magnets are more robust in construction and made of cheaper material. Superconductive magnets allow more compact design (a single HTS 4.2×0.3 mm wire carries about 100 A of current) and demand less cooling power. In both cases, the multilayer structures require special care. In case of a copper winding one needs to provide good cooling contact to the inner winding layers beneath the coil surface and avoid any local rise of the temperature due to the exponential dependency of resistivity on temperature as shown in fig. 4.5, which introduces a positive feedback in the system.

In case of superconductive magnets the multilayer windings need special design efforts because the inner layers (surrounded from both sides by other HTS layers) must be cooled below the transition temperature, but heat transfer in the wire itself is poor compared to copper. As reported by Schwarz et al. [81] for 1-st generation Bismuth-based HTS tapes, the thermal conductivities at 30 K are 45 W/mK and 1.4 W/mK along and through the wire, respectively. This is orders of magnitude lower than the $\sim 10^3$ W/mK thermal conductivity of copper at the same temperature. Thermal conductivity of second-generation Yttrium-based wires is not better than that of the first-generation because the highly conductive silver matrix containing the HTS ceramic is no longer used in the wire structure. Additional thermal resistance is unavoidable

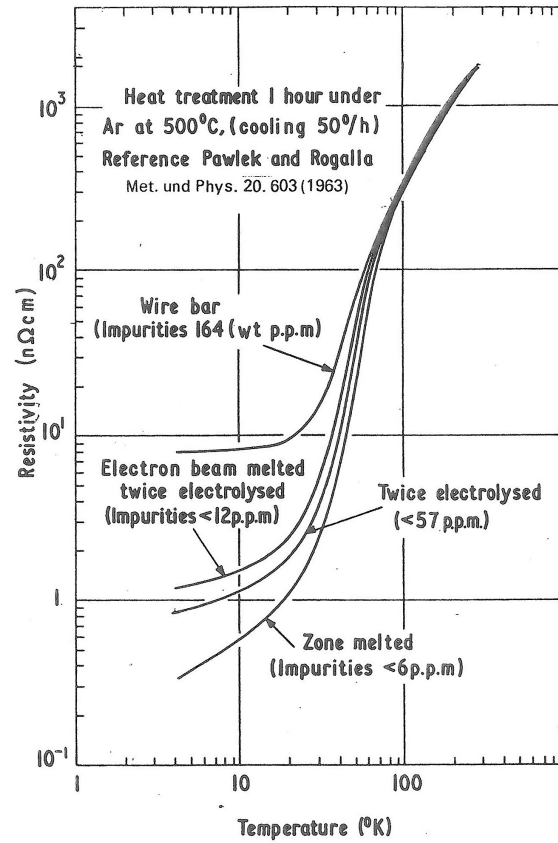


Figure 4.5: Electrical resistivity of copper at cryogenic conditions, by Cryogenic Data D.H.J. Goodall A.P.T division Culham laboratory, 1970 [80].

at any transition between the layers.

Nevertheless, the lack of Joule heat and huge tolerable temperature deviations, from a working point near 40 K to the transition temperature of 120 K, make HTS the best option for multilayer coils. Thus the first step to choose the proper winding option for a particular magnet is to define how many layers of winding must be stacked on top of each other. There are two groups of magnets in the system. The longitudinal magnets such as MS and RS produce a field along a certain distance and provide enough surface area to place the wire. Their windings must have an even number of layers wound as spirals going in opposite directions to compensate the tilting of the magnetic field. The latter is equal to d/D where D is the diameter and d the spiral pitch which can be greater or equal to the wire width (for HTS and MS magnet $d/D > 1.5 \times 10^{-2}$). The transverse magnets, i.e. the compensators and MV coils, produce a field comparable in strength to the longitudinal magnets. However the transverse magnets have to be compact. The toroids are an intermediate case as they have sufficient surface area for winding, but must also produce higher field than the rest of the longitudinal magnets. Moreover they must be thin enough to fit in between the MV magnets and leave enough space between the toroid and the ion beam line for the compensators.

In the case of HTS winding the Ampere-turns from table 4.1 can be translated into the number of turns by simply assuming a current of about 70 A which is close to the

Table 4.2: Number of turns and heat emission of the coils at 215 G field for 1 keV electrons. The heat emission includes emission from *all* magnets of the type for the *complete cooler*. Total heat emission of about 20 W can be taken as an estimate of heat load in case of resistive realization.

Name	items	HTS turns @ 70 A per coil	Total heat emission copper @ 40 K, W
MS	1	130	2.96
RS	2	30	2.80
MV	8	10	2.32
TSH	2	79	3.59
TSV	2	14	0.23
TAC	4	0.3	0.03
Comp1	4	17	1.95
Comp2	4	28	5.11

minimum amperage of available HTS wires on the market, assuming a safety margin of 30%. For the resistive option there is no unique translation. One can either reduce the heat emission by increasing the number of turns while lowering the current, or keep the system mechanically more simple using a minimum number of layers. The heat emission calculations in table 4.2 assume dense winding of $\varnothing 5$ mm copper wire in two layers with 70% filling of the available surface for MS, RS, TSH, TSV and comparable to HTS magnets by space requirements 5×5 wire batch for MV, Comp1 and Comp2.

The coils with the highest number of winding layers are the MV, the Comp1 and the Comp2, requiring 10, 17 and 28 layers, respectively. To keep them compact the better option is clearly build them as superconductive coils. The problem of poor thermal conductivity of the wire and between the layers can be solved by immersing the entire winding into a cryogen. This solution is however not envisaged for the RS, the toroids and the MS because construction of pressurized vacuum-tight vessels of such volume and complex shape would be an extreme effort. The superconductive option still remains attractive for them because of the saving in the heat emission (see table 4.2) moreover there is much less additional cost for this option if at least some of the magnets are already designed superconductive. To test the feasibility of the superconductive option for the longitudinal magnets an experimental study on conduction-cooled HTS wire, with sparsely distributed thermal contacts, is needed. Such a study is reported at the end of this chapter. In the following section we will discuss the design and test of the first superconductive magnet. It serves as a prototype for the MV and compensator (Comp1, Comp2) magnets where superconductive realization is imperative due to the space limitations and multilayer structure.

4.1.4 Superconductive coils design

To ensure proper cooling through many layers of HTS material it has been decided to build the compensator and MV magnets as conductors placed in a cryogen-filled volume. Because the magnets are designed to be used in the environment of the

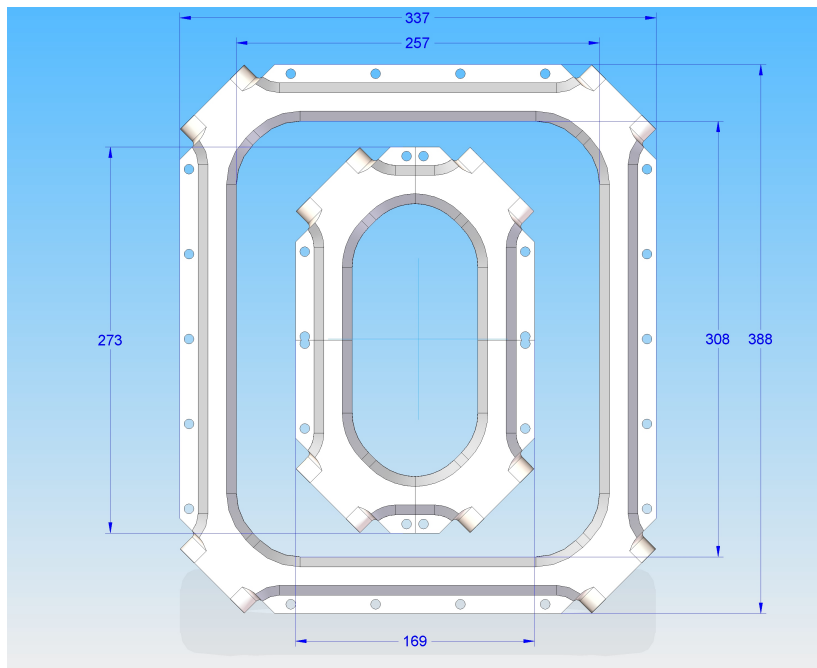


Figure 4.6: Juxtaposed compensator (Comp1, Comp2) and MV coil bodies as 3d models, dimensions in mm.

isolation vacuum the cryogen-filled volume should be only in a small manifold of the winding, as it would otherwise create significant deformations in the coil due to the pressure difference between the inside and the outside. The MV coils must have large free areas in the middle to allow mounting them around the merging vacuum chamber (see fig. 4.4). The design thus resembles a toroidal tube closed around the wire winding. However, this shell must provide access to wind the coil and guide the electric contacts and cryogen connections to the outside.

It must also be considered that the sealing methods involving high temperature procedures, such as welding or brazing, cannot be used as the HTS material must not be exposed to temperatures above 180°C even for short times. Welding seams in stainless steel are also potentially dangerous as the magnetic permeability of the steel tends to rise during welding. Therefore, following the general CSR guideline to minimize use of magnetic materials, especially close to the ion beam and in high magnetic field regions, the best material choice for the shell is aluminum. The material is non-magnetic, inexpensive compared to other options (e.g. titanium) and easily workable. The mounting flanges can be closed by sealings using materials softer than aluminum such as gold, indium or Helicoflex seals. Indium sealings require less space for the flange compared to Helicoflex and are more widely used in vacuum and cryogenic equipment than gold, making them the first choice option. In spite of the difference in dimensions between compensators and MV magnets, almost the same design, based on the considerations just given, can be adopted for both types of coils, scaling only the lengths of the straight tube-like sections forming the coil body (see fig. 4.6).

The design concept of the compensator (Comp1, Comp2) coil is shown in fig. 4.7

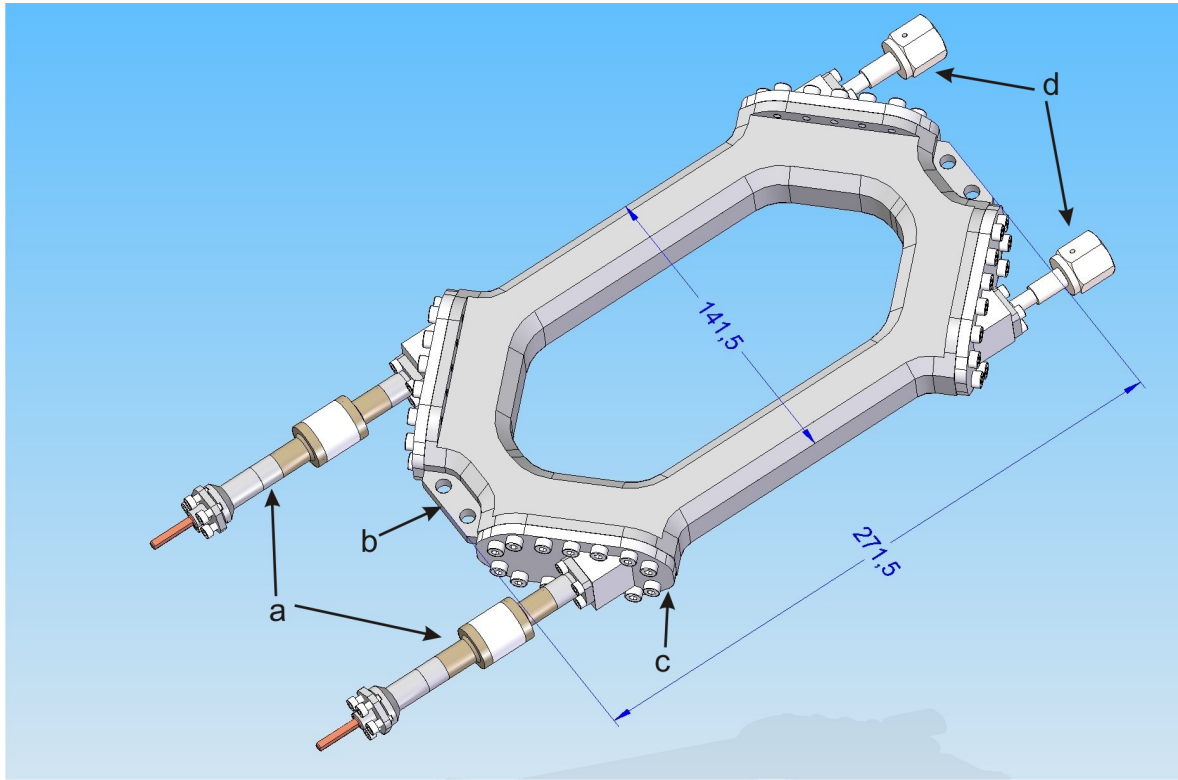


Figure 4.7: Test HTS coil assembly. a- current feedthroughs, b - alignment hold, c - mounting corner flange, d - cryogen couplings, dimensions in mm.

and a cut view of it in fig. 4.8. Hereafter this coil is referred to as the test coil or the prototype coil. The coil body is machined out of an aluminum block with the internal volume created by drilling $\varnothing 20$ mm channels along the coil bars and milling the interior of the corners, where the channels intersect. The HTS wire is guided inside of the coil by PTFE profiles of E-shaped cross-section (see a in fig. 4.8), which create two vertically separated planes to resolve HTS terminals in the vertical plane like in a generic pancake coil. The winding is performed by pulling the complete wire length through the open corners.

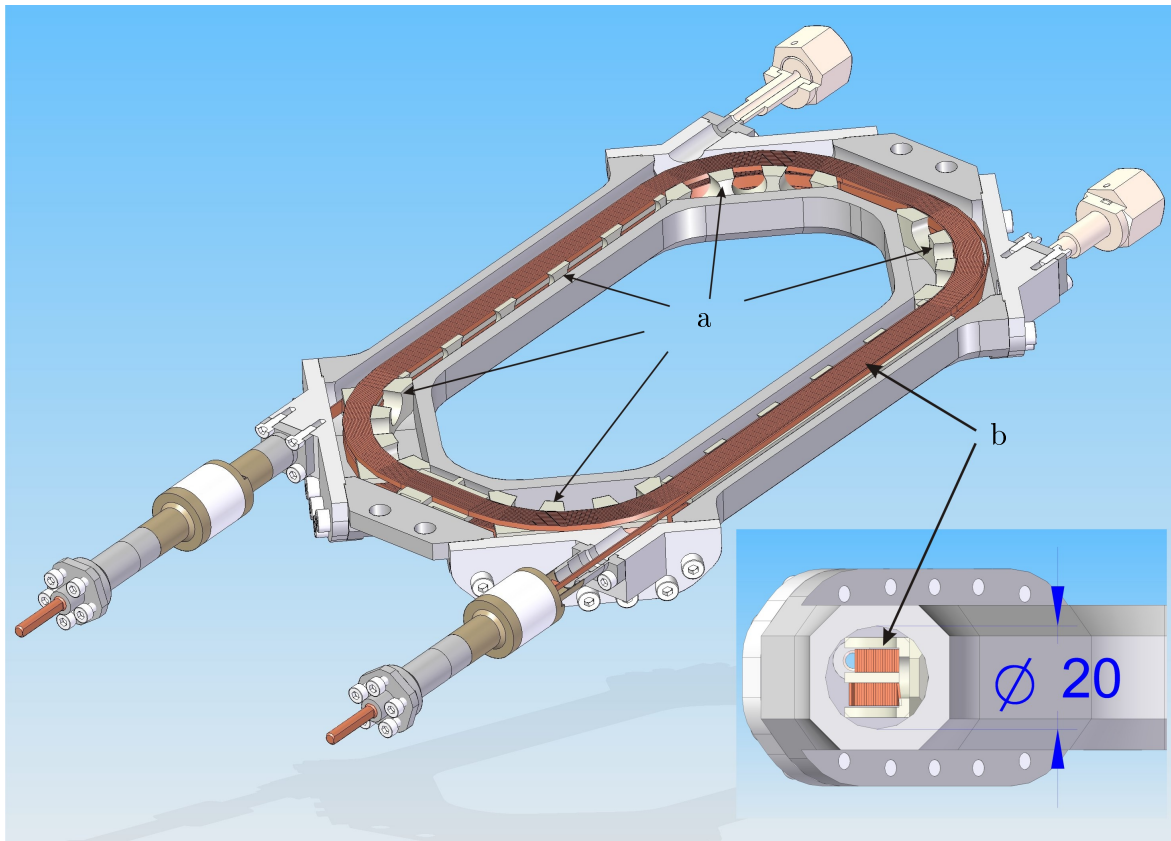


Figure 4.8: Test HTS coil section view, a - guiding PTFE profiles, b - HTS winding.

After the winding is complete, the HTS wire is soldered to a feedthrough and the corner flanges are sealed. The principle of mounting is shown in fig. 4.9. First the wound wire (a, labeling acc. to fig. 4.9) is soldered to the copper pin with an overlap of 50 mm (e). Then the isolator structure is put over the joint. The isolator has sealings on both sides. The coil side has an indium wire sealing (h), between the aluminum corner flange and the steel end of the isolator which is pressed by 4 screws. The opposite sealing lies between a conical surface on the copper pin (d) and a conical cutout inside of the isolator body (f). The sealing pressure is applied by a special collar (j) mounted on the pin. The pin close to the isolator end is threaded (c) to allow fixation of the collar on the pin. The collar has 5 threaded holes for screws (i) pushing the isolator. By tightening of these screws the pin is pulled and the isolator is pushed so that sealing pressure is created on the conical surface.

The corners opposite to the current feedtroughs are used for the cryogen connections (see fig. 4.10). The connections are metal-gasket 1/4-inch VCR couplings. The VCR glands are welded to end pieces tightened by 4 screws to the aluminum flange by indium rings. In the channel between cryogen connections a special PTFE plug is installed to block the flow and prevent coolant short circuit. The additional indium sealings between the VCR connections and flanges and isolators and flanges are introduced to be able to make corner flanges out of aluminum. This solution is preferable compared to welding of the VCR couplings and isolators to a steel flange because in case of a large

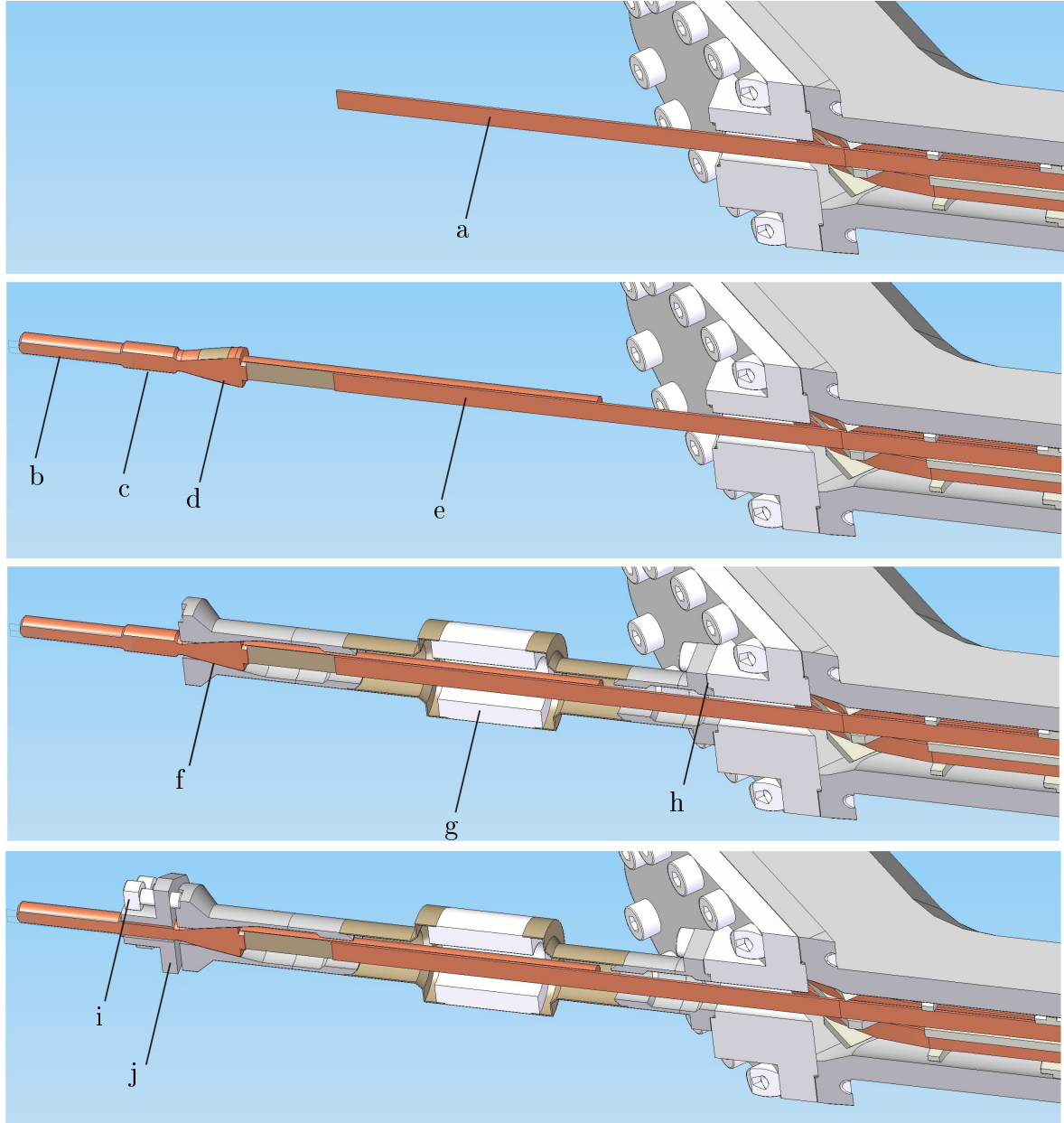


Figure 4.9: HTS coil current feedthrough, a - end of the HTS wire, b - copper contact surface, c - thread on the copper pin, d - conical sealing surface of the copper pin, e - soldering overlap of the HTS wire and the copper pin, f - conical sealing on the isolator tube, g - ceramic isolator, h - indium wire sealing, i - pressing screw, j - pulling collar on the copper pin.

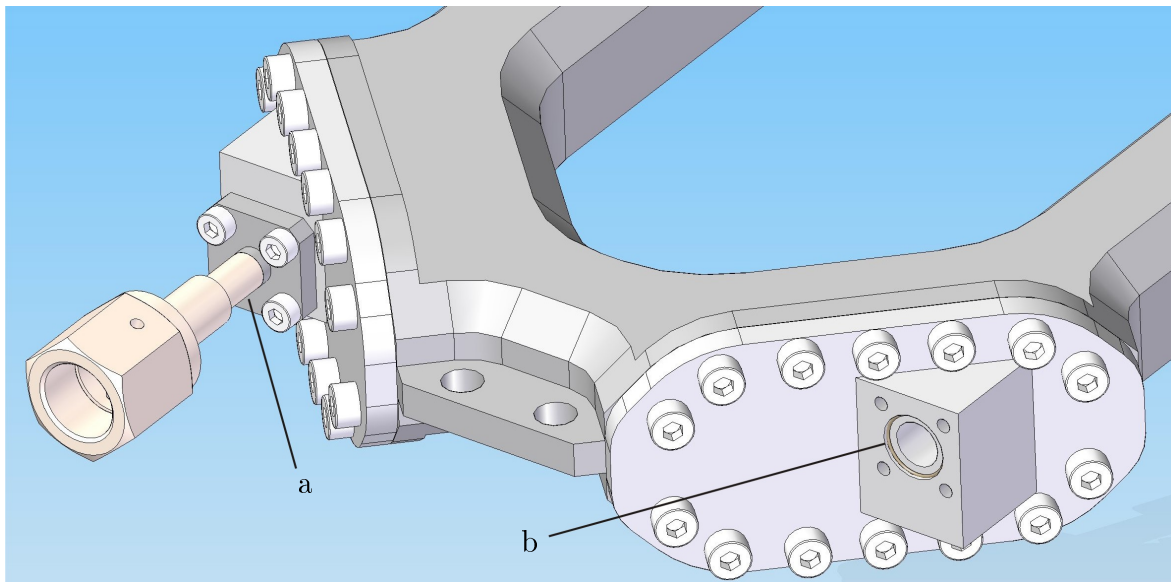


Figure 4.10: HTS coil cryogen couplings, a - mounted VCR coupling, b - indium sealing for the VCR coupling.

steel flange the significant relative difference of thermal expansion coefficients between steel and aluminum ($\sim 1.25 \times 10^{-3}$) is potentially dangerous for the vacuum tightness.

The design for the Comp1,2 and the MV coils are almost identical with the only difference in the size (see. fig. 4.6). A test coil of the compensator type according to this design was manufactured and tested to prove the feasibility of the concept. The construction process is described in more details in the following section.

4.1.5 Construction of the test coil

To prove the design concept, a full-size model of a compensator coil has been constructed and tested. The purpose of the test coil was to confirm feasibility of the winding process, the sealing properties and to serve as a test load of the newly developed cryogenic cooling system. The test coil was wound with 19 turns of American Superconductor High Strength Plus stainless-steel-reinforced 1-st generation Bismuth-based wire. The wire has a cross-section of $4.2 \times 0.3 \text{ mm}^2$ including a Kapton isolation. The used wire is specified to carry, at liquid nitrogen temperature, a current of at least 145 Amperes. The wire is mechanically rigid and cannot be bent in the plane of the tape or be twisted over short lengths. Perpendicular to the wire plane the minimum double bend diameter is 38 mm. If bent with smaller radii the wire is permanently damaged, which strongly reduces its current carrying capabilities. Even sharper bends cause cracking and breaking. Thus special precautions were taken to avoid sharp bending while winding the coil.

The winding procedure is as follows. The wire is introduced in one of the corner flanges on the cryogen couplings side along the short bar of the coil. In this region the PTFE guiding profile has no separation between the top and the bottom planes.

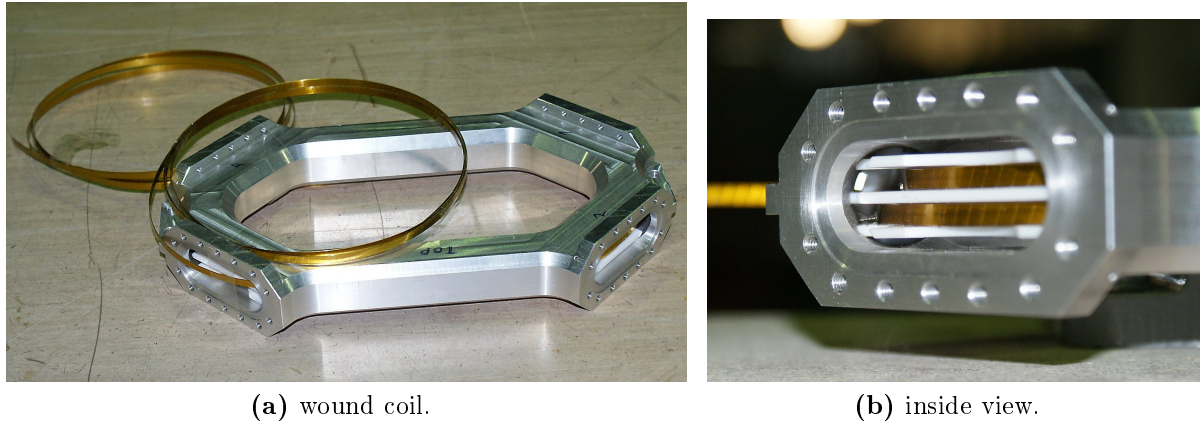


Figure 4.11: Wound HTS test coil (left), inside view through a corner flange prior to insertion of the flow blocking plug (right).

The wire introduced on the bottom is guided upwards and exits the section at the top level. Half of the complete winding length of the coil is pulled through such that the mid-point all the conductor length is at the middle of the coil bar. Then the two ends are wound each in its own plane such that the wire terminals are at the top layer in both the bottom and the top planes. This winding was done by guiding the wire tip through a half of the coil, then pulling the entire length to the outside and introducing the wire tip back for the next half of the turn. To retain the tension in the wire, the end not used for winding was fixed in a jaw vice. After completion of the winding, a small PTFE plug was inserted to block the cryogen flow from a short cut between the cryogen lines. The wound coil is shown in fig. 4.11a.

The next step was to solder the superconductor to the current feedthroughs and close the corner flanges. According to the manufacturer's service note for soldering and splicing, a proper soldering joint should have an overlap of about 50 mm [82, 83]. The HTS wire structure contains a soldered joint of stainless steel tape, which reinforces the composite wire structure, made with a solder material melting at 179°C. Therefore to avoid delamination the wire should not be exposed to temperatures above 175° [83]. The recommended soldering materials are pure indium (melts at 157°C) or eutectic In-Sn Indalloy 1E (118°C). In this work pure indium was used. Prior to soldering, both surfaces (HTS and copper) were wetted with indium using non-activated rosin soldering flux. The soldering process is shown in fig. 4.12. For final soldering the wire and the pin were covered with rosin flux, aligned in jaw vices and pressed together by two aluminum soldering plates (a). The plates have two electric heaters (b) of 25 W power mounted on each of them. The temperature control during the soldering process was performed by a PT1000 resistive thermo sensor (e). In order to apply the pressure uniformly, the plates were pressed together by 6 screws (d) with spring washers. The soldering procedure includes heating of the plates from room temperature to 168°C within 8 minutes, maintaining this temperature for 3 minutes as recommended by the manufacturer and fast cooling down with an air fan. The temperature during the hot

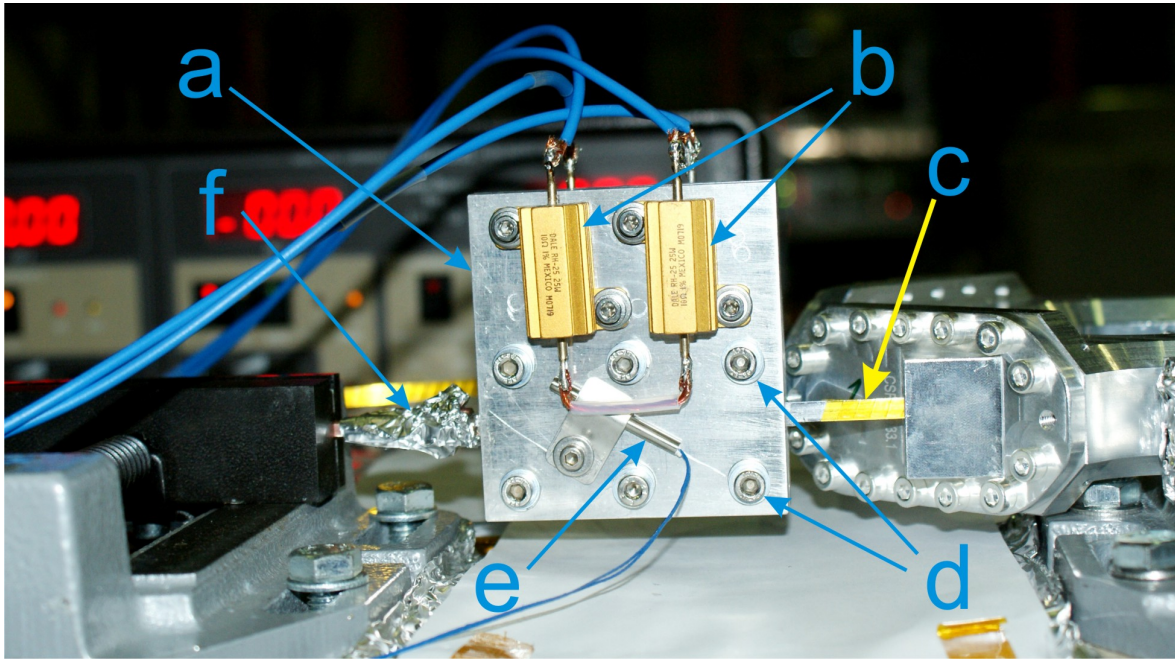


Figure 4.12: The soldering process. The aluminum plate (a) with mounted heaters (b) presses the HTS wire (c) by 6 M4 screws (d) with spring washers to the copper pin (f). The conical sealing surface of the pin is covered with foil to protect from scratches. The temperature during the process is monitored by a PT100 sensor (e).

phase of the soldering process was kept within $\pm 2^\circ\text{C}$ by adjusting the heating current.

The soldering joint exhibited good mechanical stability and the electric contact seemed to be established through the entire overlap surface. After both soldering joints were complete the corner flanges were sealed. For the cryogen flanges the VCR couplings were pre-mounted on the flanges. The sealing was done using 0.5-mm indium wire cleaned in ethanol. The o-rings were formed in place by putting the indium wire into the sealing cut-out (see fig. 4.13b). The wire ends were overlapped over a few millimeters distance one on top of the other and gently pinched (see fig. 4.13a). The VCR connections were then installed and tightened with four M3 screws. Following the literature recommendations [84] the tightening was performed in two steps: After a first pre-tightening with 0.2 Nm torque on each screw the joint was left to rest for about an hour to let the indium creep. The final tightening was done by applying torque of 0.4 Nm and resulted in contact of the stainless steel and aluminum surfaces.

The corner flanges were sealed using 1 mm indium wire. In a similar way o-rings were formed in place in the inner corner of the sealing cut-out. Thicker 1 mm wire allowed to use more reliable inclined-cut technique (see fig. 4.13a) to bound the two wire ends, as freshly cut indium surfaces stick to each other much better than air-exposed ones. After placing the wire, the flange was positioned by means of two rods (see fig. 4.14) mounted diagonally in the screw threads. The rods are manufactured with small tolerances so the flange can slide along them only if parallel to its counterpart. This assures the parallelism of surfaces before pressing of the In wire. The tightening is performed in a similar two-step procedure as described above. The flanges were

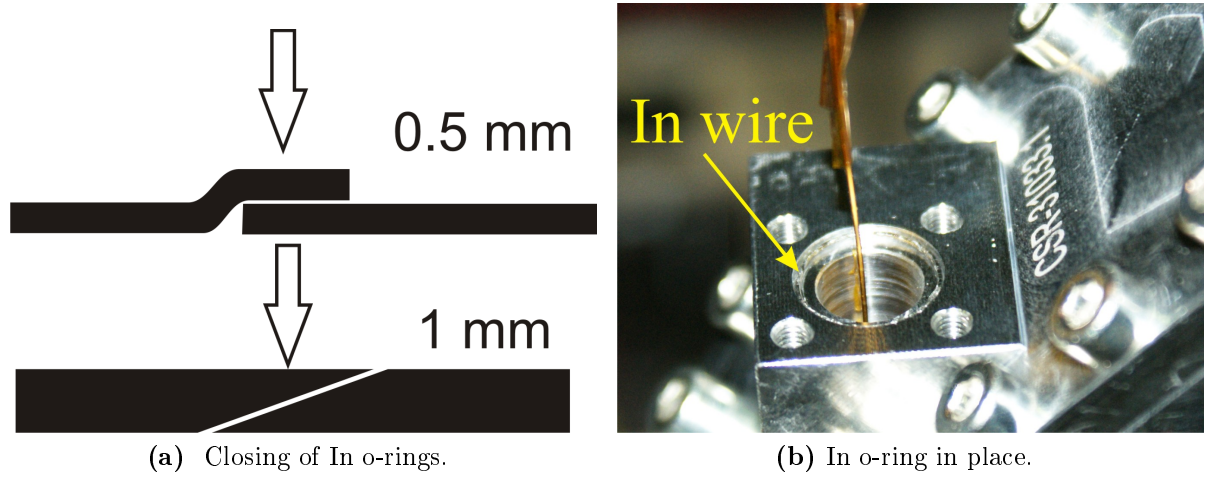


Figure 4.13: Indium sealing technique. Wire overlap methods used for 0.5 and 1 mm In wires, the arrows show the tightening pressure (left). Indium ring in place to seal the cryogen coupling (right).

pre-tightened with a torque of 0.3 Nm, rested for an hour and were finally tightened in steps with 0.4, 0.5, 0.6, 0.7, 0.9 and 1.1 Nm torque, until metal-to-metal contact of aluminum surfaces was reached.

The last step was the mounting of the isolator tubes (see fig. 4.9). Prior to sealing the back side of the isolator (h), the conical surfaces on both the copper pin (d) and the inside cone on the isolator tube (f) were cleaned with ethanol. The conical surface of the pin was greased with HV high-temperature grease Apiezon H. The conical sealing was done in two steps to properly distribute the grease. The pre-tightening was done at 0.2 Nm and final sealing with 0.4 Nm. The indium sealing on the back was done in the same way as for the cryogen couplings.

After sealing the coil was underpressure-leak-tested with a helium leak-detector. The leak-detector showed no leaks above its sensitivity limit of 10^{-9} mbar·l/s. As a pre-operation test, the coil was tested in a liquid nitrogen bath to ensure that the manufacturing procedures had inflicted no damage to the HTS wire. This was done by measuring the resistance of the coil in 4 point method while applying high current to the wire. To connect the current lines, pressed copper-to-copper contacts shown in fig. 4.15 were used. The current leads (a) were also used to place the voltage transmitting wires (b) of the 4-point measuring scheme. Thus the measured resistance includes the resistances of the copper pins, the soldered copper-HTS contacts and the pressed contacts to the current lines. The measurement therefore gives a result corresponding to practical operation of the coil. In order to ensure a HTS temperature below the transition point the coil was immersed in liquid nitrogen, with the VCR connections (d) open letting the liquid in. The coil was slowly cooled down within about 3 hours in nitrogen vapor in a heat isolated bath, the level of nitrogen being raised slowly when approaching the coil. After the coil was fully immersed in the liquid and the thermo sensor (c) on the coil body showed 77 K temperature of the coil body, the resistance measurements were carried out.

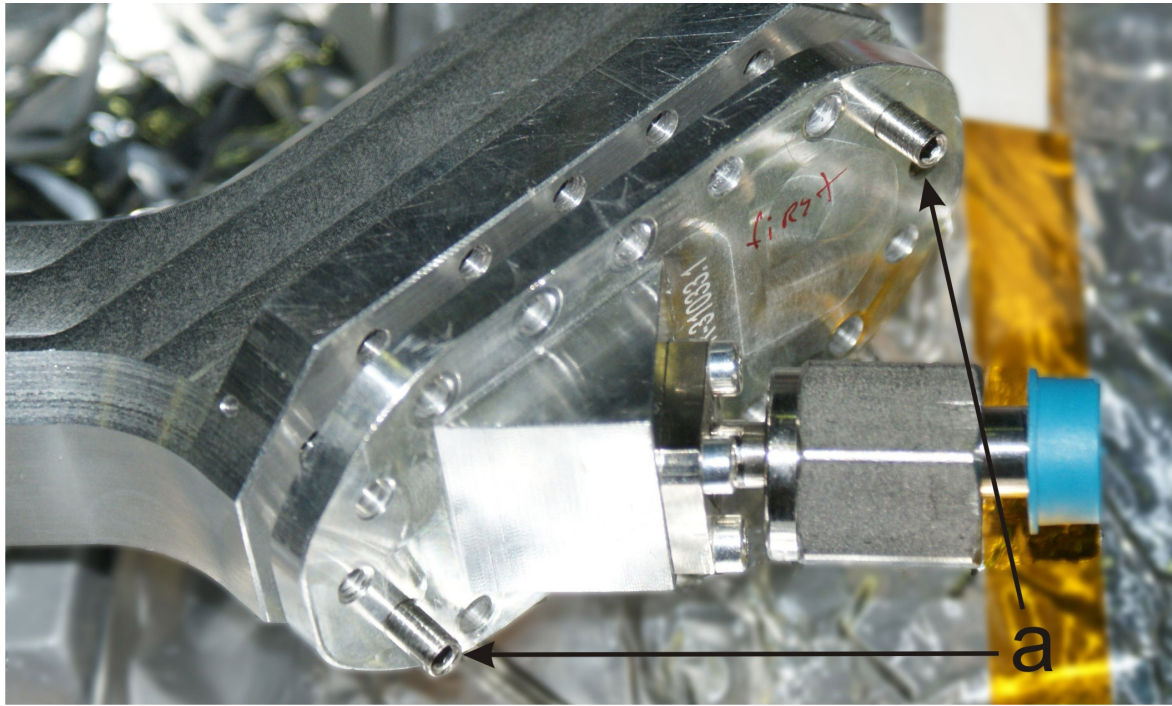


Figure 4.14: Mounting of a corner flange with a pre-installed VCR coupling. The guiding rods (a) provide parallel placing of the flange and the body.

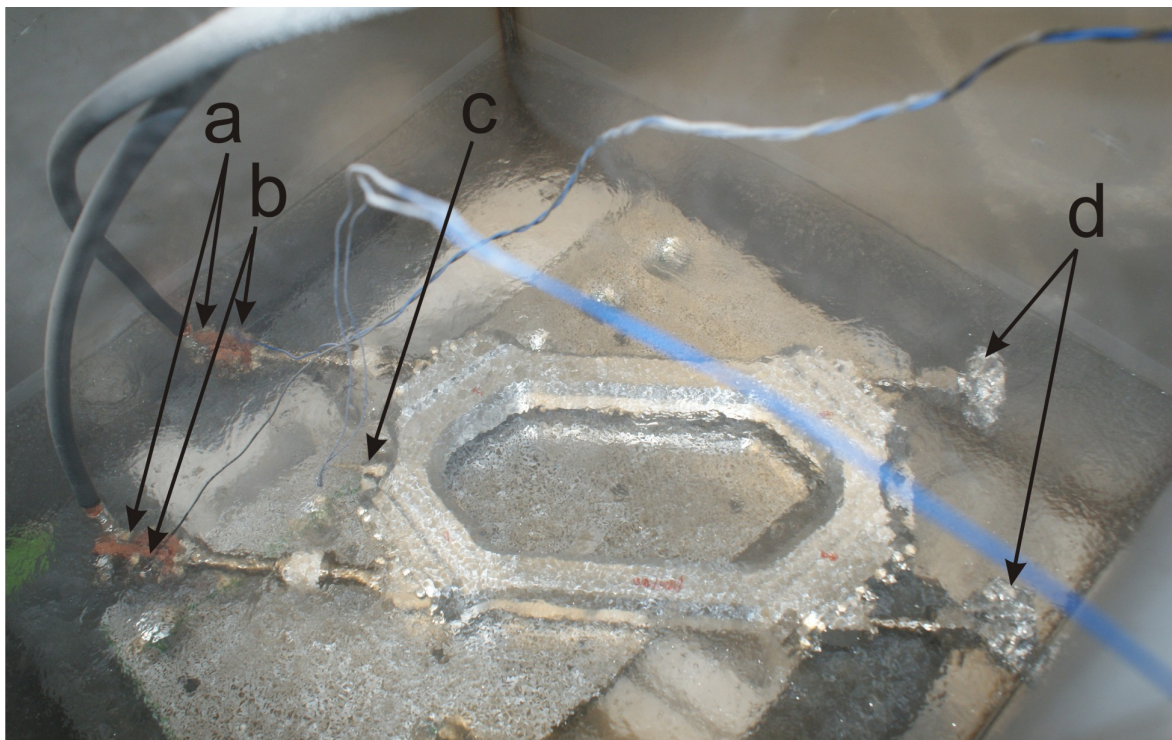


Figure 4.15: Test coil in the LN bath. The current leads (a) used to provide up to 60 A current, voltage contacts (b) showed the voltage of 0.9 mV at 60 A current, the temperature was controlled by a PT1000 sensor mounted on the coil body (c), the VCR connections were left open to let nitrogen in, but covered with perforated foil to filter small bits of Styrofoam presented in liquid.

Using a power supply providing up to 60 A current, a resistance of $15 \mu\Omega$ was measured. The measured resistance exceeds the resistance of soldered joint between HTS and copper, which according to the manufacturer is in best cases about 100-200

n Ω . The main contribution to the total resistance seems to be due to the pressed copper contacts. For a square inch contact, this resistance of polished copper surfaces reported to be in the range 1-67 $\mu\Omega$ [85] under cryogenic conditions. After the liquid nitrogen test, the coil was left to slowly warm up and later tested once again with the leak-detector, which yielded the same positive result.

After these successful preliminary tests the final commissioning test requires operating the coil in real conditions carrying design current with overpressure inside and the cryostat vacuum outside at a cryogenic temperature. Such a test was performed with the actual cooling circuit built for the electron cooler magnets. Design and construction of the cooling system are reported in the following sections.

4.2 Cryogenic cooling system

4.2.1 Concept of the cryogenic cooling system

As a part of the electron cooler a cryogenic cooling system was developed in the frame of this work. On the basis of the magnet data summarized in sections 4.1.2 and 4.1.3 one can define the design parameters of this system. In case of resistive copper coils it must deliver ~ 20 W of cooling power (see table 4.2) at a temperature of 30-40 K. This temperature is a compromise between the resistivity of copper, dropping strongly in the region from the room temperature down to 20 K (see fig. 4.5), and the cooling capacity of cryocoolers, which also decreases with temperature (see used later fig. 4.17). For a single-stage cryocooler the cooling power drops sharp below 30 K reaching zero at temperatures of about 15 K. The cooling system should also fulfill the requirement of immersing the HTS in the Comp1, Comp2 and MV coils in an efficiently cooling cryogen medium.

To provide cooling power at a stable temperature and to be able to remove significant heat with low mass flow, a cooling system with a phase transition is preferred. In such a system the heat Q is absorbed by a phase transition from liquid to gas phase, $Q = m\Delta H$, where ΔH is the specific transition enthalpy and m is the mass of evaporating liquid. If only a limited temperature difference ΔT is tolerated the value of ΔH is much higher than the sensible heat $c_p\Delta T$ for all suitable cryogens. Thus, a two phase system allows to use much lower mass flows \dot{m} compared to gas phase cooling. For the magnet cooling system one needs a suitable medium with a phase transition in the region around 30 K. In cooling setups of this temperature range hydrogen, with a liquid-gas transition at 20.3 K, was rather widely used [86, 87, 88, 89], but its application is now restricted due to safety concerns. An attractive alternative is neon [90], whose use in closed cycle cryogenic systems is rapidly growing after progress in the HTS technology [91, 92, 93, 94, 95]. Its liquid-gas transition point at 27 K [96], its chemical stability, and the high value of its transition enthalpy make it a perfect can-

didate to use in our system. The need to distribute the medium in a complex system makes forced circulation a preferable option compared to natural convection systems such as thermosyphons [97].

The developed layout of the system can be represented as follows (see fig 4.16). The neon is supplied by a room-temperature operated compressor (Comp) under a certain overpressure. The compressed gas is pre-cooled and fed to a condensation unit, where it is brought in contact with a cold surface cooled by a cold-head cryocooler. In the condensation unit the gas is partly liquefied and then transported to the thermal load. In the load the liquid fraction evaporates removing the heat from the load. The return flow is then fed to the compressor closing the cycle. To save the cooling capacity of the cold head this scheme needs a heat exchanger designed in a way, that the cold return flow is cooling the direct flow from the compressor to a temperature close to the boiling point of neon. The heat exchanger as well the condensation unit and the cold head must be installed in a vacuum cryostat. In order to be able to service the cold head without breaking the CSR cryostat vacuum, the cooling system cryostat should be independent of the CSR vacuum.

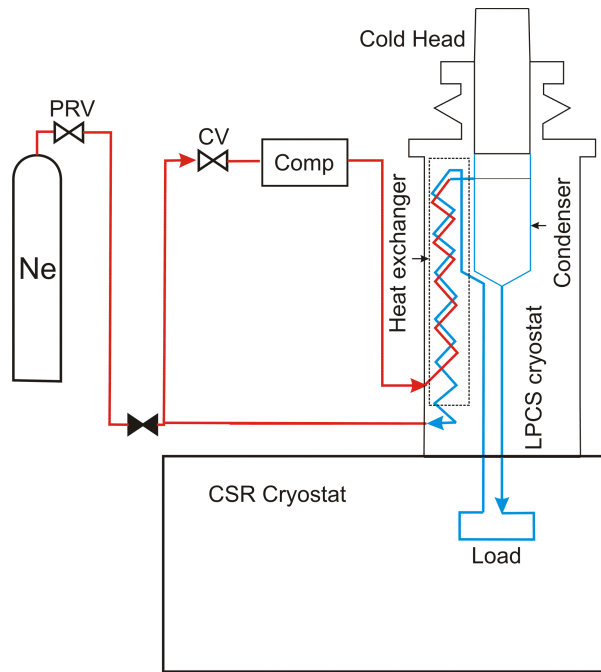


Figure 4.16: Scheme of the closed cycle cryogenic cooling system. The circulation is forced by a compressor, the warm gas from compressor gets pre-cooled in a counterflow heat exchanger. Pre-cooled gas enters the condenser cooled by the cold head. The gas-liquid mixture is the transported to the load installed in a separate cryostat. The medium converted to gas is then transported back and as a return stream cools down the direct flow. Warmed in the exchanger, the return flow is fed to the compressor, the flow is regulated by the control valve (CV).

As the pressurized medium is pumped through the magnets the working absolute pressure of the system was designed to be of about 3 bar. This is much lower compared to the pressure of up to 20 bar in the main CSR cooling system, thus greatly simplifies the mechanical design. Hereafter the cooling system is therefore referred to as the

Low Pressure Cooling System (LPCS). To build such a system one needs to choose a proper cold head; the condensation unit, the heat exchanger and the cryostat must be specifically designed as no suitable commercial alternatives exist. This development will be reported in the following section.

4.2.2 Cryogenic cooling system design studies

The first design step is to find a proper cryocooler for our needs. We have specified a thermal load of about 20 W at 30 K temperature for the electron cooler magnets. We also need to foresee pre-cooling of the medium, even after the heat exchanger, and some heat leaks which may occur in the system. Thus a rather powerful single-stage cold head is needed. The best suited one amongst the available options is the Leybold 140 T Coolpower cryocooler by Ćerlikon whose power diagram is shown in fig. 4.17.

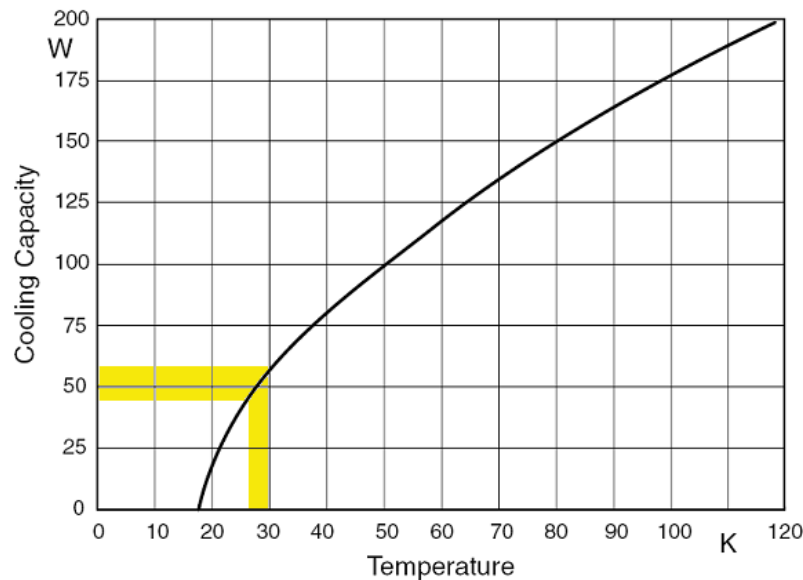


Figure 4.17: Cooling capacity of the Leybold 140T Coolpower cold head, data sheet by Ćerlikon. The yellow area shows the temperature range of interest and the available cooling capacity at these temperatures.

The design of the condensation unit (see fig. 4.18) was developed in cooperation with L. Kochenda and M. Vznuzdaev from the group of A. Vasilev (PNPI, Gatchina). It follows a common approach in building of cryogenic condensers, where a vacuum vessel hosts a condensation body made of thermally highly conducting material coupled to a cold head, with the body surface increased by fins or ribs [98]. The condenser (see fig. 4.18) is a vacuum vessel with two VCR connections (c,h) on its ends. The condensation body (a) as well as the top flange (b), where the condenser is coupled to the cold head, are made of copper. The flange has an axial cut through which the top part of the copper body passes and is brazed (d) to the flange. The inlet connection (c) is brazed to the flange and continued by a channel drilled into the flange. The gas flow is then spread around the condenser body in the azimuthal direction (e) and

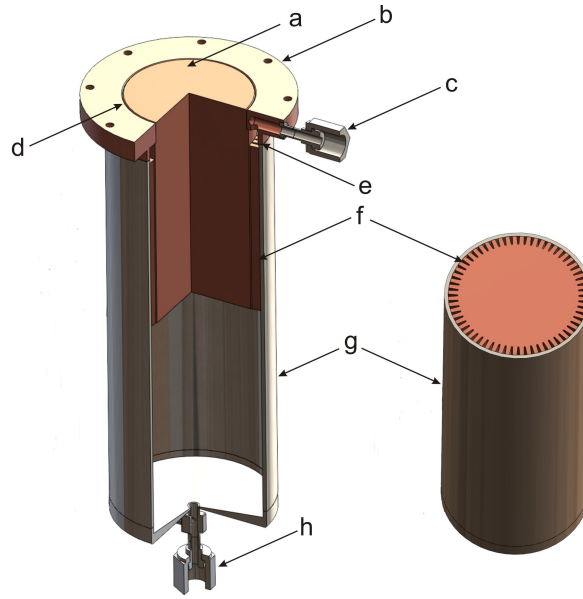


Figure 4.18: The condenser of the LPCS. a) Copper condenser body, b) copper flange for coupling with the cold head, c) VCR gas inlet coupling, d) brazing seam, e) azimuthal distribution channel, f) cooling channels formed by ribs on the copper body and the outer steel shell, g) external steel shell, h) VCR outlet coupling.



Figure 4.19: A schematic counter-flow heat exchanger.

distributed amongst the 100 mm long channels (f) formed by the ribs on the copper body and the external stainless steel wall of the vessel (g). The total surface of the copper body is 0.1 m^2 , the outer diameter of the condenser unit is 89 mm and its length from the top flange surface to the bottom is 254 mm.

The design of the heat exchanger (see fig. 4.16) requires some calculations to be done. The only scheme which can provide low temperature difference between the cold end of the return flow and the cold end of the incoming flow is the counterflow scheme. In this scheme two gas flows in thermal contact with each other are heading in opposite directions as shown in fig. 4.19. The common technical realization of this scheme providing the maximum contact between the flows is the tube-in-tube scheme, where one flow is enclosed in a tube, surrounded by a concentric outer shell. The other stream flows in between of the inner tube and the outer shell.

The design parameters in such an exchanger are the mass flow, the cross-sections of the tubes, and the desired temperature difference between the direct and return flows on the cold side $T_{app} = T_1^C - T_2^C$ (the approach temperature), where $T_{1,2}^C$ are explained in fig. 4.19. The mass flow is defined by the specified load and the transition enthalpy

of neon. The tube cross-sections are dictated by available manufacturing options. Our free parameter is the approach temperature T_{app} , which defines the exchanger length with all other parameters being set. The mass flow can be set as $\dot{m} = W/\Delta H$ where W is the cooling power of the cold head at neon boiling temperature and ΔH is the transition enthalpy of neon of 8.58×10^4 J/kg [96]. According to the available cooling power of 48-55 W (see fig. 4.17 at 27-30 K) $\dot{m} = 0.56-0.64$ g/s.

To define the flow regime one needs to know the Reynolds number $Re = GD_h/\eta$ where η is the viscosity, D_h is the effective hydrodynamic diameter, $D_h = 4 \times A/l$ where A is the cross-section area, l is the perimeter exposed to the stream, and $G = 4\dot{m}/A$. The neon viscosity changes from $\eta = 31.6 \mu$ Pa·s at 300 K and 1 bar to 6.8μ Pa·s at 40 K and 1 bar with no significant dependence on pressure in the range 1-10 bar at temperatures above 40 K [96]. Taking practical dimension of the inner tube as 10×1 mm and the flow rate of 0.64 g/s one gets Reynolds numbers of 3200-15000 depending on the local temperature which is above the transition to turbulent flow at about 2000. Thus the theory of turbulent heat exchangers can be applied.

For a turbulent heat exchanger, if one neglects the resistance of the metallic tube wall and the heat transfer along the tube, one derives from the energy conservation law the length of the exchanger as [99]

$$L = \frac{\alpha}{\gamma} \left(\frac{T_1^H + \beta/\gamma}{T_1^C + \beta/\gamma} \right), \quad (4.1)$$

$$\text{where } \alpha \approx \dot{m}_1 c_1 \left(\frac{1}{h_1 S_1} + \frac{1}{h_2 S_2} \right), \quad \beta = \left(\frac{\dot{m}_1 c_1}{\dot{m}_2 c_2} T_1^C - T_2^C \right), \quad \gamma = 1 - \frac{\dot{m}_1 c_1}{\dot{m}_2 c_2}. \quad (4.2)$$

The notations $T_{1,2}^{H,C}$ are clarified in fig. 4.19, $S_{1,2}$ are the perimeters of the respective flows, $\dot{m}_{1,2}$ are the mass flows and $c_{1,2}$ are specific heats. The coefficients $h_{1,2}$ are the heat transfer coefficients, defined such that the rate of heat transfer from the gas to the tube per unit area is $\dot{Q} = h\Delta T$. In case of a closed-cycle counterflow exchanger, the specific heats c_1 and c_2 are equal as well as the mass flows \dot{m}_1 and \dot{m}_2 . So the equation 4.1 turns into

$$L = \frac{\alpha}{\beta} \left(T_1^H - T_1^C \right) \quad \text{where } \beta = T_1^C - T_2^C. \quad (4.3)$$

The coefficient h depends on the viscosity η , the thermal conductivity κ , the specific heat c_p of the medium and the effective tube diameter D_e . Introducing Nusselt number $Nu = hD_e/\kappa$ (the ratio of convective heat transfer coefficient to the conductive heat transfer coefficient) one can use the Dittus-Boetler correlation (see [100])

$$Nu = 0.023 Re^{0.8} Pr^{0.4}, \quad (4.4)$$

where Pr is Prandtl's number $Pr = \eta c_p/\kappa$, h is expressed in W/m²K, κ in W/mK, c_p

in J/kgK, D_e in meters, G in kg/m²s and η is in Pa·s. Then substituting the definitions of Nu , Re and Pr in equation 4.4 one gets

$$h = \frac{0.023}{Pr^{0.6}} c_p \frac{G^{0.8} \eta^{0.2}}{D_e^{0.2}}. \quad (4.5)$$

The effective diameter for the direct flow is equal to the actual inner diameter of the direct tube of 8 mm so $G_1 = 4\dot{m}/\pi D^2 = 12.8$ kg/m²s. For the return flow formed by a tube with minimum inner diameter $D_2 = 16$ mm and inner tube of $D_1 = 10$ outer diameter the effective diameter D_e is 6 mm, and the $G_2 = 4\dot{m}/\pi (D_1^2 - D_2^2) = 5.2$ kg/m²s. The specific heat c_p is almost constant in the temperature range of interest changing from 1.062×10^3 J/kgK at 40 K to 1.031×10^3 J/kgK at 300 K [96], with no significant dependence on pressure. In the same way, the heat conductivity does not depend strongly on pressure [96], thus the reference data for 1 bar pressure can be used. According to [101] for neon at 1 bar pressure κ is equal to 9.908×10^{-3} W/mK at 40 K and to 4.953×10^{-2} W/mK at 300 K. Using these numbers one gets Pr for both temperature extremes as $Pr(40 \text{ K}) = 0.667$ and $Pr(300 \text{ K}) = 0.75$. Now one can get the heat transfer coefficients for both direct and return streams and finally the required length of the heat exchanger based on the reference numbers for neon at 300 K and 40 K as upper and lower limits for the real length. The heat transfer coefficients for direct stream are $h_1(40 \text{ K}) = 6.64 \times 10^{-3} c_p G_1^{0.8} = 52.4$ W/m²K and $h_1(300 \text{ K}) = 2.3 \times 10^{-2} c_p G_2^{0.8} = 76.6$ W/m²K. The same holds for the return stream $h_2(40 \text{ K}) = 6.64 \times 10^{-3} c_p G_2^{0.8} = 27.1$ W/m²K and $h_1(300 \text{ K}) = 2.3 \times 10^{-2} c_p G_2^{0.8} = 37.5$ W/m²K. The perimeters $S_{1,2}$ of the heat transfer from the respective streams according to the given above dimensions are $S_1 = \pi D_{inner} = 25.1$ mm for the direct and $S_2 = \pi D_{outer} = 31.4$ mm for the return flow. Setting the approach temperature of 10 K, such that $T_1^H = 300$ K, $T_1^C = 40$ K, $T_2^H = 290$ K and $T_2^C = 30$ K, finally one gets $L(300 \text{ K}) = 23.5$ m and $L(40 \text{ K}) = 33.2$ m.

Taking the latter as an upper limit one can set a length of 35 meters as suitable to get required approach temperature. According to [99] the pressure drop for a gas of density ρ , viscosity η flowing at rate \dot{m} in a pipe of diameter D and length L is

$$\Delta p = \frac{1}{2} \psi \frac{L G^2}{D_e \rho}, \quad (4.6)$$

where the dimensionless factor ψ for a turbulent flow is given by $\psi = 0.316(GD/\eta)^{-0.25}$ [99]. For direct flow $\psi(300 \text{ K}) = 0.042$, $\psi(40 \text{ K}) = 0.028$. For the neon density at 2 bar absolute pressure, the given flow rate and the length of 35 meters the frictional pressure loss is between 8.3×10^{-2} and 7.5×10^{-3} bar assuming a flow with the uniform temperatures of 300 K and 40 K, respectively. The actual value is between these limits due to the temperature gradient in the exchanger, but both of them are small compared to the pressure difference created by the compressor.

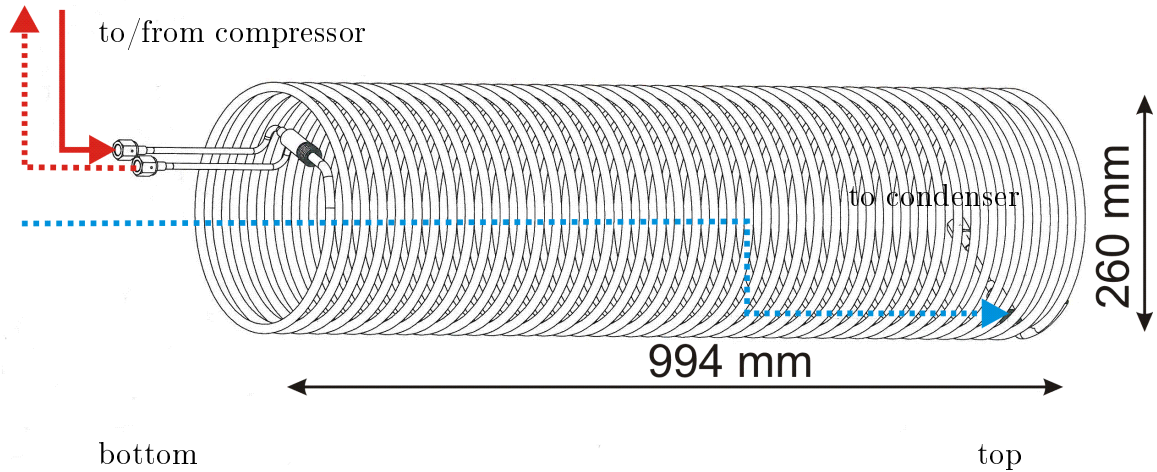


Figure 4.20: The circulation scheme in the heat exchanger: The cold return flow (blue dashed) comes from the electron cooler through the transfer flange, goes to the top of the exchanger in a dedicated connection line and after reaching the top starts to descent in the outer layer (the hose is not shown) of the exchanger slowly heating to room temperature at which it leaves the exchanger towards the external part of the circuit (dashed red). The direct flow comes from the compressor at room temperature, and after getting into the cryostat enters the exchanger at the bottom part (solid red), it gets cooled while ascending along the inner layer of the exchanger and leaves the exchanger at the top (solid blue) to immediately get into the condenser. After the condenser the line goes down parallel to the cryogenic return line (not shown).

4.2.3 Design of the heat exchanger and cryostat

The heat exchanger length of 35 meters requires it to be folded in some way to fit in a compact cryostat. The design developed for the LPCS has the heat exchanger wound in a spiral of 260 mm central diameter (see fig. 4.20). The spiral has 44 turns. Part of the space inside of the spiral is used to install the condensation unit and the cold head.

The exchanger and the condenser are fitted inside of a vacuum cryostat (see fig. 4.21, later in this section the indexes in brackets are related to fig. 4.21) made of a vertical tube equipped with ISO-K 320 flanges on the top and bottom and 4 ISO-K 200 flanges arranged in a cross for outside connections, external equipment and mounting access. The entire internal structure is suspended on the top flange (c). The cold head (a) is fitted with an ISO-K 160 flange and is mounted on the top flange via a vibration damping collar (b). The heat exchanger (j) is suspended by a system of 7 rings (h) connected to each other by 3 bars (g). All the rings and bars are made of 2 mm stainless steel sheets and have multiple cuts to reduce the effective heat transfer cross-section. The support system is attached to the top flange (c) by 6 chains (e). To increase the distance between the room temperature top flange and the cold parts the chains are attached to the third ring from the top having the length of 42 cm. One of the side flanges at the bottom cross is used to feed through the gas lines between the heat exchanger and the compressor (o). The cryogenic gas line vacuum-to-vacuum feedthroughs for the connections to the heat load (s) have been specially designed.

The feedthroughs thermally decouple the cryogenic lines from the room temperature bottom flange (r) which separates the LPCS cryostat from the CSR linear chamber. The complete tower is then installed on top of the CSR linear chamber on an ISO-K 320/ISO-K 500 reduction flange (r) fitting the top of the CSR cryostat chamber. Details on the construction of the LPCS are reported in the next section.

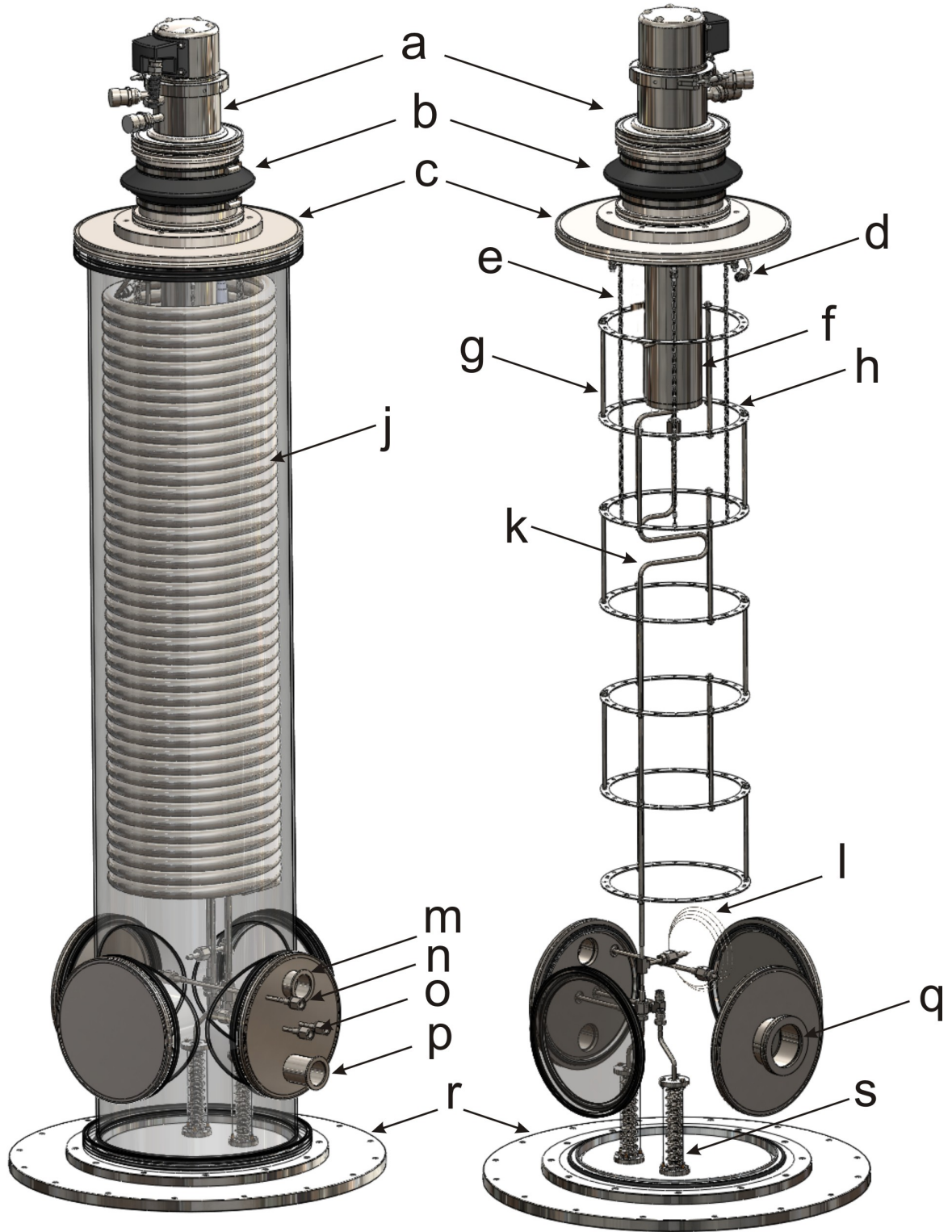


Figure 4.21: Design of the LPCS. a) cold head, b) elastic collar, c) ISO-K 320/160 reduction flange, d) connection of the heat exchanger and the condenser, e) stainless steel suspension chain, f) condenser, g) interring bar, h) suspension ring, j) heat exchanger, k) direct flow cryogenic line, l) capillary pressure transmitting line, m) pressure gauge flange, n) VCR coupling of the pressure capillary, o) VCR couplings for in and out gas lines, p) flange for electrical feedthroughs, q) ISO-K 63 turbo pump flange, r) transition flange to the CSR linear chamber, s) cryogenic feedthroughs.

4.2.4 Construction of the LPCS

The heat exchanger was realized by Pink GmbH using a 10×1 copper tube as the inside tube and a stainless steel corrugated flexible tube of 16/22 mm diameter as

the outer shell. To keep the inner tube centered in the outer shell a 3mm copper wire was wound on the inner tube with the spiral pitch of 70-80 mm. The exchanger was then terminated with welded end pieces. The complete exchanger was bent by winding on a bobbin and delivered to MPIK in the spiral form. The supporting ring structure of the heat exchanger was assembled plane by plane and shifted inside the exchanger spiral. The individual exchanger turns were attached to the support by 0.3 mm steel wires passing through the holes in the inter-ring bars (see fig. 4.22 right B). The assembled structure was attached by suspension chains to the top flange of the LPCS cryostat which was installed on a temporary mounting frame (see fig. 4.22, left). On the frame the heat exchanger was isolated both inside and outside with 30 layers of Mylar-based multilayer isolation (Coolcat from RUAG Space GmbH, later referred to as superisolation) to suppress radiative heat transfer.

The condenser unit (see fig. 4.18) was manufactured and quality tested at the MPIK mechanical workshop. The complete assembly is shown in fig. 4.23 and the indexes in brackets are related to this figure. To couple the condenser (1) to the cold head (3) and provide space between the condenser and the top flange for connections to the heat exchanger, a transition copper bloc (2) of 40 mm thickness was introduced in between the cold head and the condenser unit. In order to improve the thermal contact between the surfaces (c) Apizenon N cryogenic grease was used. The copper bloc was also used to mount a heating element (d) to be in direct contact with the cold head as a tool to control the cooling power remaining for to the downstream part of the cooling circuit. To precisely measure the temperature of the cold head a DT-670 silicon diode sensor (f) was mounted on the cold head flange. Additional PT1000 thermo sensors (a,b) were placed as shown in fig. 4.23. Just like the exchanger all the cold surfaces were isolated with 30 layers of superisolation.

The complete assembly of cold head and condenser was mounted to the cryostat top flange through a collar of elastic neoprene. The purpose of the collar was to reduce the transfer of vibration from the cold head to the CSR cryostat chamber and the parts inside of the cryostat. The membrane itself was found not to be rigid enough to sustain the atmospheric pressure on the evacuated setup. To prevent metal flanges from contact, 4 PTFE separators were installed between the upper and lower parts of the collar (see fig. 4.24).

From the connection between the heat exchanger and the condenser an additional gas line was guided downwards to reach a safety valve on one of the flanges at the bottom part of the tower. The top flange was then put in place. To decouple the two vacuum cryostats cryogenic vacuum-to-vacuum feedthroughs based on thermal decoupling by 110 mm long bellow sections were used. The outer bellow surface as well as the top flanges were isolated with 30 layers of superisolation and the cryogenic lines inside of the bellow sections with 10 layers.

To monitor the pressure in the cryogenic region the cold line from the condenser

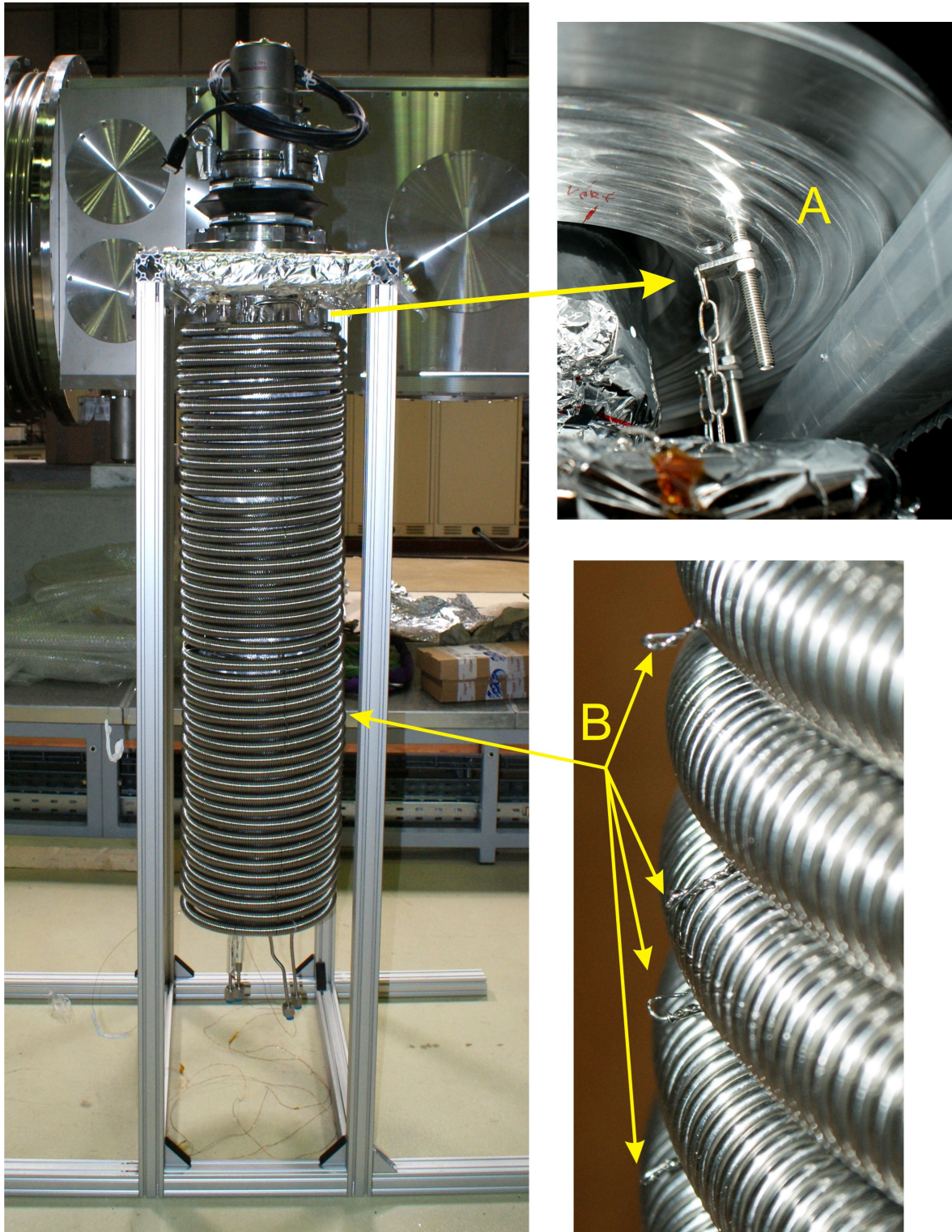


Figure 4.22: The heat exchanger suspended to the cryostat top flange by 6 chains (A) with the cold head on the construction support. The fixation of individual turns by steel wires is shown on the right (B). In between of the exchanger turns the inside superisolation is visible.

to the load is equipped with a T-piece where a 1×0.1 mm capillary tube of 1 m length is attached. The capillary transfers the pressure from the cryogenic region to a room temperature pressure sensor installed outside of the vacuum cryostat. For a more detailed temperature control additional thermo sensors are installed on both direct and return lines feedthrough top flanges and on the return line 20 centimeters

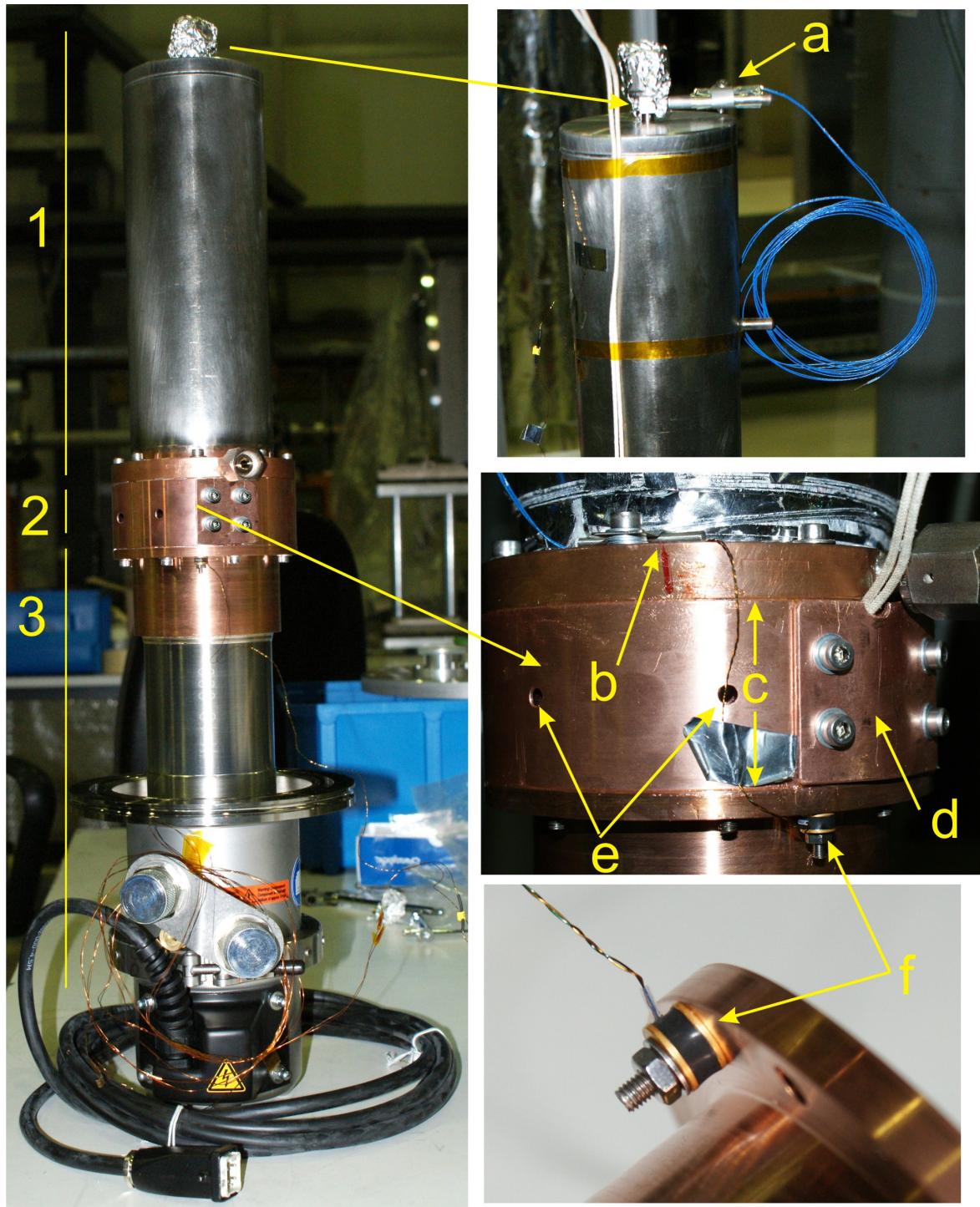
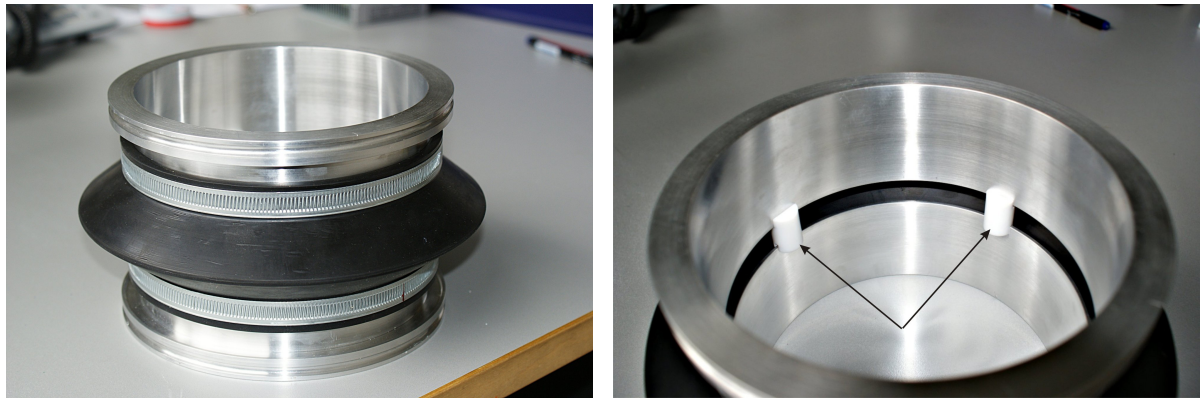


Figure 4.23: Construction of the condenser assembly. The complete assembly on the left consists of the condenser itself (1), the transition piece (2) and the cold head (3) screwed together. On the close-ups on the right one can see a) the PT1000 sensor on the blind tube at the bottom of the condenser b) PT1000 on the top flange of the condenser c) to copper-to-copper interfaces greased with Apiezon N for better thermal contact, d) a cover which presses the heating module to the transition piece e) venting holes to pump the air out of pockets inside of the transition piece, f) silicon diode mounted on the cold head for precise temperature control.

above the feedthrough flange. The complete set of connections is shown in fig. 4.26 and the mechanical layout is shown in fig. 4.25.



(a) Elastic element of the cooling tower.

(b) The inside view with spacers installed.

Figure 4.24: Elastic collar of the cold head.

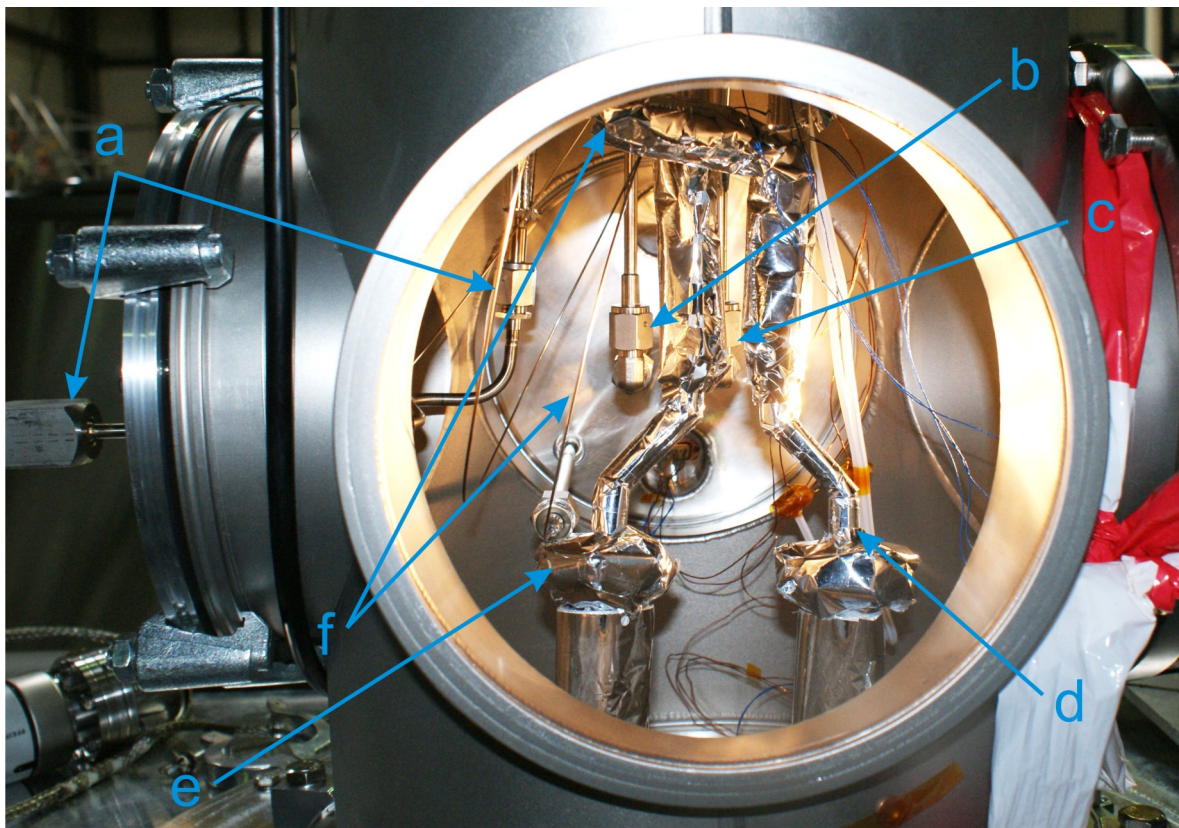


Figure 4.25: Connections in the cross region of the LPCS cryostat. a) The line from the condenser to the relief valve, b) the warm end of the return line, c) the warm end of the direct line, d) the cryogenic feedthrough of the direct line, e) the cryogenic feedthrough of the return line, f) pressure transmitting capillary leaving the cryogenic region from T-piece on the direct line and reaching to the outside.

4.2.5 Gas circulation and control system

For operation and control of the LPCS some additional equipment must be introduced into the simplified scheme given in fig. 4.16. The complete scheme of the LPCS is shown in fig. 4.26. In this scheme the LPCS was operated during its commissioning and further use. The abbreviations in brackets later in this section are related to the labeling in fig. 4.26.

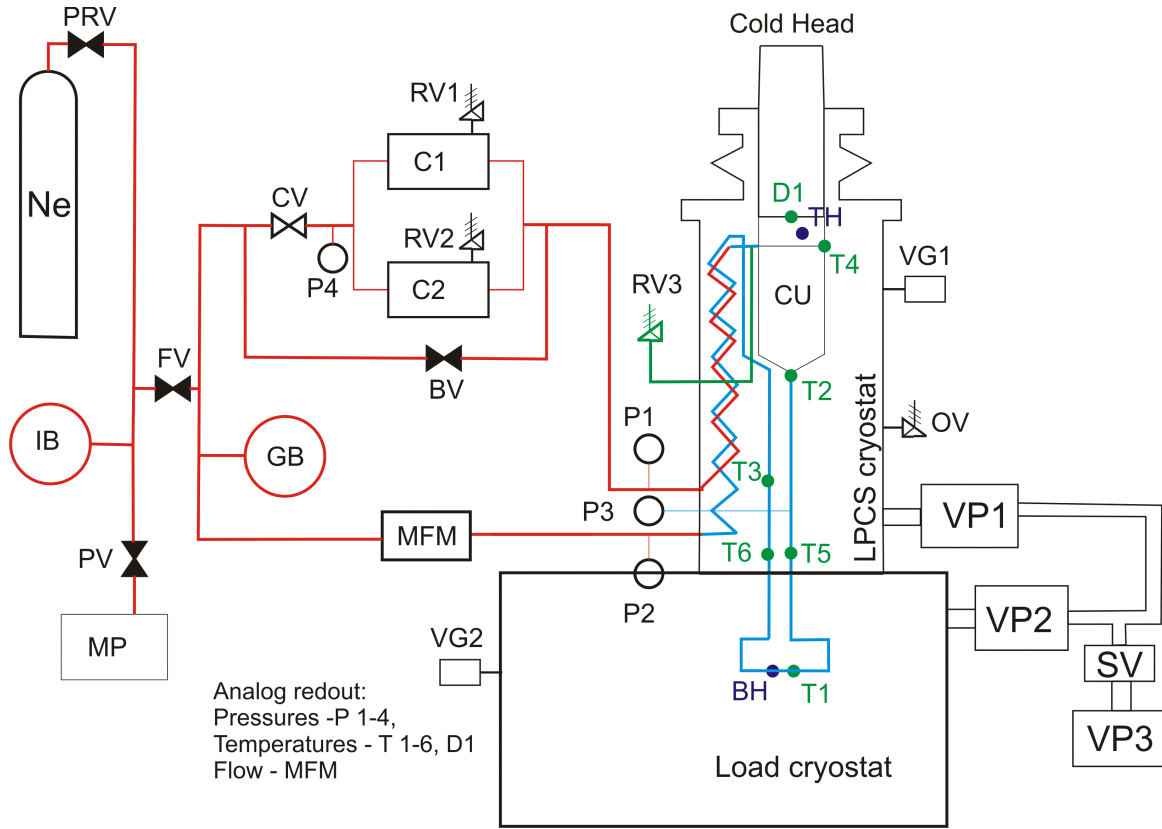


Figure 4.26: Control and diagnostics scheme of the LPCS. The condenser unit is denoted as CU, the main gas buffer by GB, and the injection buffer by IB. The room temperature/warm lines are shown in red, cold lines in blue and the safety relief line in green. The valves closed in normal operation are painted out. These valves are the filling valve FV, the purging valve PV, the bypass valve BV (not used) and the pressure reducing valve PRV. The system is purged by means of the membrane pump MP. The flow is forced by the two parallel compressors C1 and C2, with only one normally in use. The flow is regulated by the control valve CV and measured by the mass flow meter MFM. The diagnostics consists of pressure transmitters P1-4, silicon diode thermo sensor D1, PT1000 thermo sensors T1-6. The cooling power is counterbalanced by the top heater TH on the cold head, and the bottom heater BH on the load. Operation safety is provided by the small relief valves on the compressors RV1, RV2, the main relief valve RV3, vacuum overpressure valve (flange) OV and the electropneumatic vacuum safety valve SV. The vacuum in the cryostats is created by the turbo pumps VP1,2 and the dry scroll pump VP3, the vacuum pressure controlled by the vacuum gauges VG1,2.

The forced circulation is provided by two membrane compressors (C1, C2) Vakuubrand ME 4R NT creating an overpressure at the entrance of the circuit of up to 3.2 barg (hereafter relative to atmospheric pressures are given using the unit barg (bar gauge)). For the operation at pressures below 2.5 barg only one pump is used. The flow in the system is regulated by means of a manual needle control valve (CV) which defines the pressure at the inlet of the pumps. The inlet pressure can have values from 100 mbar to 1.1 bar. The lower boundary depends on the pressure at the pump exhaust and, for pressures of 2 barg, reaches up to 400 mbar. The upper limit is set by the construction of the valves inside of the pump which are unable to close completely if the entrance pressure exceeds 1.1 bar, which strongly degrades the flow rate, as a part of the gas is pushed back to the entrance. Each pump has an adjustable built-in relief valve (RV1, RV2) which limits the maximum pressure at the exhaust. If the pressure exceeds the set value the cooling gas is released to the atmosphere. The

valves were set to open at the maximum pressure of 3.2 barg which can be produced by the pumps themselves. The built-in relief valves are not certified as safety devices and the operational safety is based on another certified relief valve (RV3).

The flow in the circuit is monitored by a thermal mass flow meter (MFM). The MFM is calibrated in Argon by the manufacturer for the flow range up to 100 standard liters per minute and delivers an analog voltage signal to the data acquisition system (DAQ) controlling the LPCS. The circuit includes two buffer volumes. The main 4 liters gas buffer (GB) is connected to the circuit by a T-piece between the MFM and the control valve. It is foreseen to mitigate pressure and flow oscillations in the system. The small 2 liter injection buffer (IB) is used to add controlled amounts of gas in the system during operation. For the rest of the time the injection buffer is cut off by the filling valve (FV). The filling valve is used for initial filling, purging and refilling of the system.

The initial filling is performed by introducing gas from a 200 bar 50 liter neon gas bottle through a pressure reducing valve (PRV). As the system is operated at temperatures below the freezing temperature of nitrogen, it is necessary to remove air from the closed circuit before filling neon in. To purge the system it is first pumped down using the membrane pump (MP) able to reach 1 mbar pressure. Then prior to operation, the system is filled with neon and purged a few times before cooling down so that any contaminations are diluted to harmless concentration.

To control the cooling power used at the load there are two heating modules (TH, BH) in the system each of 100 W nominal power. The top heater (TH) is used to partly or completely counterbalance the cold head by putting thermal load directly onto it. The bottom heater (BH) at the load is used to simulate the actual heat load while operating the system.

The DAQ is based on a National Instruments NI 6036E ADC card which collects analog voltage signals from pressure sensors, MFM and temperature sensors. The flow diagnostics includes 4 pressure sensors measuring relative pressure at the pumps entrance after the control valve (P4), at the pump exhaust on the exchanger entrance (P1), the pressure in the cryogenic region between the condenser and the load (P3) through a capillary pressure transmitter and at the exit of the exchanger (P2). The temperature is monitored in several points of the system. The diode sensor (D1) on the cold head is controlled by a dedicated Lakeshore 211 control module which delivers an analog signal to the DAQ. The rest of the thermo sensors (T1-6) are PT1000 resistive thermometers connected to the ADC through resistance-to-voltage converters developed in house.

The vacuum equipment of the system consists of an ISO-K 63 size Varian turbo pump (VP1) and Leybold CF 100 turbo pump (VP2) on the linear chamber. Both turbo pumps are backed by a single Edwards XDS 5 dry scroll pump (VP3). For protection in case of a power failure an automatic electropneumatic safety valve (SV)

is installed between the turbo pumps and the fore-pump. Two additional points concern the safety aspects of the system operation. First, to protect the system from damage in case of a sudden warming up (as a consequence of a cryostat vacuum failure) the system is equipped with a relief valve Leser type 439 (RV3), which opens at 3.5 barg. Another safety precaution was taken to protect the cryostat from overpressure in case of a line rupture within the vacuum volume. The only ISO-K 200 flange not in use on the cross at the bottom of the LPCS tower was replaced by an ISO-F flange which is pressed by screws instead of clamps (g in fig. 4.27). After reaching fore-vacuum pressure the screws are loosened such that the flange can pop if pushed by overpressure from the inside, but cannot fly away and cause secondary damage (denoted as “overpressure valve” OV in fig. 4.26).

The external gas circuit was mounted on an aluminum plate installed on top of the CSR linear chamber which was used as a load cryostat. The gas lines outside of the cryostat are made of 8 mm steel tubes with Swagelok conical fittings. A view of the assembled outer circuit is shown in fig. 4.27.

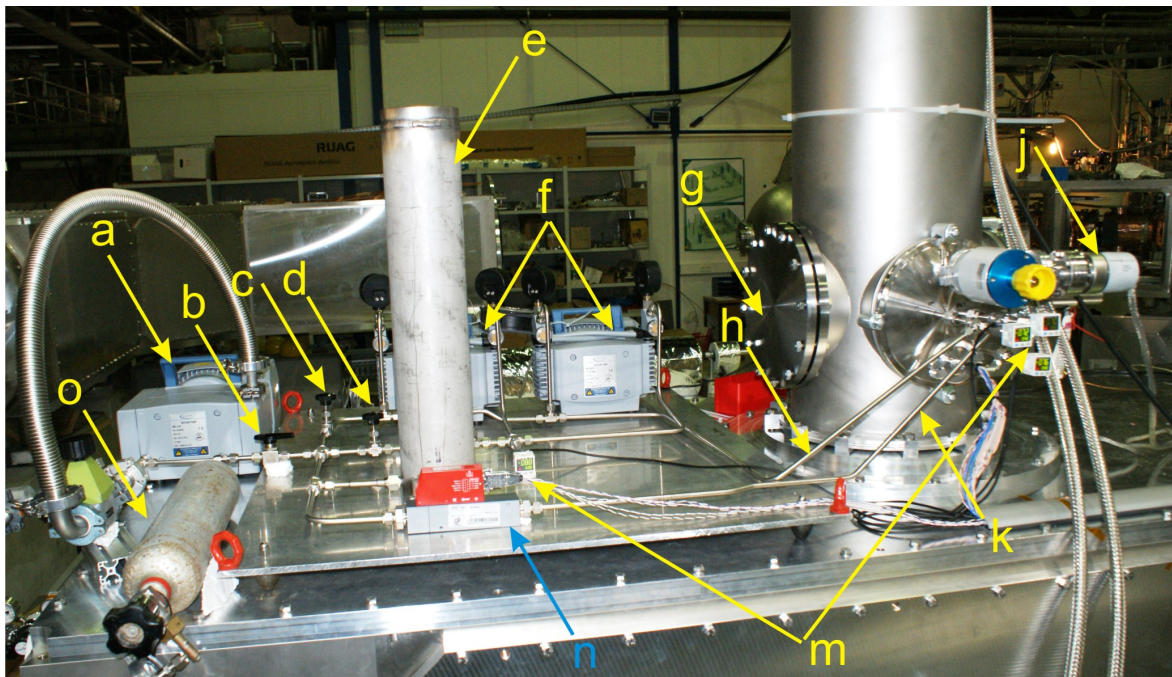


Figure 4.27: The external gas circuit of the LPCS. a) purging membrane pump, b) filling ball valve c) bypass needle valve d) control needle valve, e) main buffer volume, f) compressors, g) ISO-F 200 popping flange, h) direct line, j) vacuum pressure gauge of the LPCS cryostat, k) return line, m) pressure sensors, n) mass flow meter o) injection buffer.

4.3 Commissioning of the LPCS and the test magnet

4.3.1 Pre-operation tests of the LPCS

Before the LPCS was operated for the first time a few pre-experimental tests were carried out. First, the LPCS was tested to satisfy the pressurized vessel safety reg-

ulations. The LPCS with dismantled safety valve and cut off external circuit was pressurized with nitrogen to 5.5 barg pressure and held without any changes for an hour as required by TÜV regulations. The tightness of the internal parts was assured by surveying the vacuum pressure in the cryostat. The external parts were checked with a sniffer device. The LPCS was filled with helium and the external circuit was checked focusing on fittings and welding seams. The test revealed minor leaks on the compressors. These leaks on the pumping heads are of about 3×10^{-3} mbar·l/s and caused by the use of PTFE sealings in the compressors. Our measurements are consistent with the leak rates provided later by the manufacturer. Such leaks are tolerable for short time operation cycles, but in a continuous operation will cause small loss of cooling medium. Apart from that the system was found to be tight.

The main safety valve (RV3 in fig. 4.26) used in the system to provide emergency relief from the cryogenic volume was also tested experimentally. The valve itself has a discharge capacity of 43 l/s at 5 barg pressure, which exceeds our needs by a factor of 10. This discharge capacity however assumes that the valve is installed in a line with inner diameter not smaller than the valves most narrow inner diameter of 10 mm, while in the LPCS design all the internal connections have 1/4 inch VCR couplings. As the manufacturer has no information on the valve performance in such conditions the discharge capacity was tested experimentally. The following test was carried out: The inner parts of the LPCS were connected to a nitrogen gas bottle, the pressure was set above the valve threshold and the flow rate was derived from the measured decrease of the pressure in the nitrogen bottle over time. The obtained value of 3.4 l/s at 3.5 barg (5.1 l/s at 5 barg) exceeds the estimation for the amount of liquid neon which can be evaporated in the condenser in an emergency warm-up. The test also showed that the safety valve must be used only in case of an emergency and not as a mean of regular system control. The reason is that the valve tightness after an emergency opening is not guaranteed and some repair of the valve might be needed.

4.3.2 Taking the LPCS in operation

After these preliminary tests were done, the LPCS was approved as a safe device and its cryogenic operation was allowed. In the first series of tests the LPCS was run with a shortcut in the load cryostat. This shortcut is a U-shaped 6×1 mm steel tube with each segment of about 10 cm length; a copper block of 3 cm length is mounted on the tube to couple a heater and a thermo sensor. For the first cool-down the LPCS was purged (see sec. 4.2.5), filled to 2.1 barg with neon and the cold head was started.

After 136 minutes the temperature of the outgoing line experienced a sharp drop from 60 to 30 K within less than a minute and stabilized at the same temperature as the cold head and the condenser flange. Shortly after, the load shortcut and the return line showed the same behavior. This is a clear sign of heat transfer in a two phase

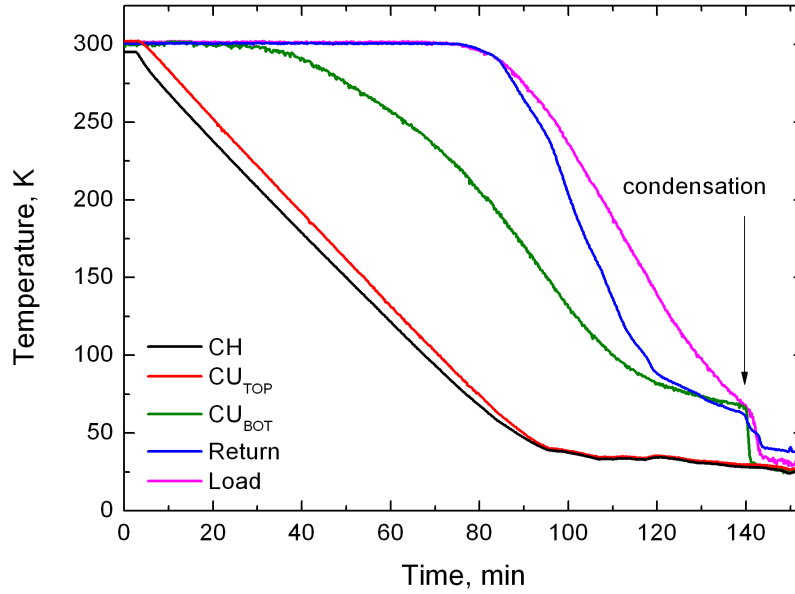


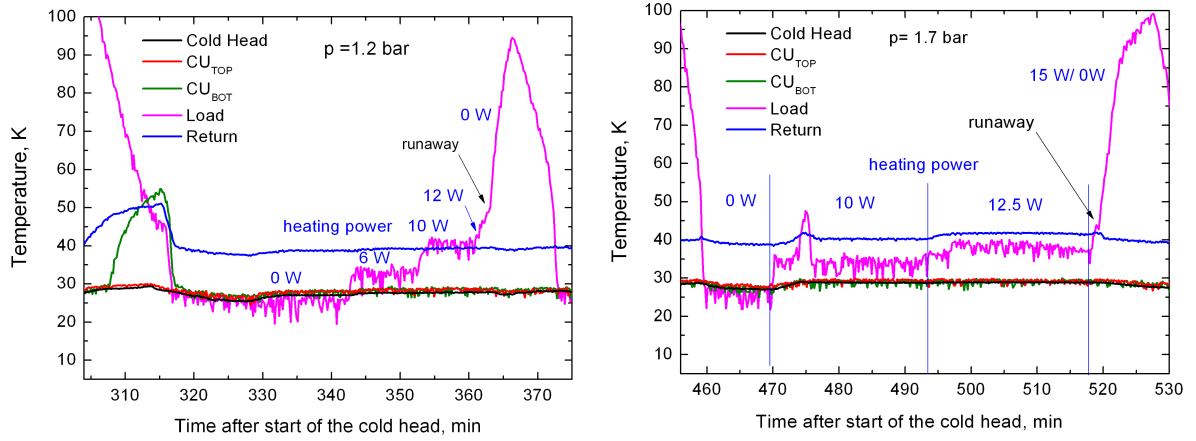
Figure 4.28: First observed condensation of neon. The top of the condenser (CU_{TOP}) follows the temperature of the cold head (CH), after ~ 140 minutes the bottom of the condenser (CU_{BOT}), load and the return line reach the temperature of 28 K.

cooling system, where the temperature remains the same across the system as long as a liquid phase present in the mixture.

After the condensation was demonstrated, the rate was measured at which liquid neon can be produced in the condenser. The idea of the measurement is the follows: If under a certain thermal load from the bottom heater the temperature of the load remains constant and close to the temperature of the condenser unit, this means that the introduced heat is removed by means of the phase transition in the cooling medium. If, however, the temperature of the load rises under increased heating power, it means that the power is partly absorbed by heating of the gas after complete evaporation of the liquid component. The threshold between the two cases defines the maximum acceptable load which the LPCS can take while still providing stable temperature conditions of 30 K.

While the LPCS is loaded by the bottom heater not to its full power, care must be taken to balance the residual cooling power by the top heater (TH) directly coupled to the cold head. Otherwise, if the system is off balance and the cooling power is not completely used, the condenser surface will be cooled down below the boiling point and reach the freezing point of neon at 24.5 K. In such a situation neon freezes on the cold surface, the gas flow stops and the load starts to heat up under the applied electric power as no coolant is circulating.

In the following test the LPCS was cooled down and stabilized at about 30 K by the combination of the heating powers from the gas flow alone and the electric heating from the top heater. The power of the top heater was then reduced and the power of the bottom heater increased. In experiments with normal operating pressure of the cryogen of 1.2 bar (see fig. 4.29a), the system was reacting normally up to the bottom



(a) Cooling power transfer to the load at $p = 1.2$ bar. (b) Cooling power transfer to the load at $p = 1.7$ bar.

Figure 4.29: Transfer of cooling power to the short cut load, runaway of the system occurs above 10 W of heating power at 1.2 bar neon pressure and above 12.5 W at working pressure of 1.7 bar.

heater power of 10 W. In experiments at elevated cryogen pressure of 1.7 bar (by injection of the gas from injection buffer) the maximum power of the bottom heater properly handled by the LPCS was 12.5 W (see fig. 4.29b). In both cases the total available cooling power was significantly higher and an additional power of 12 and 16 W, respectively, was applied to the cold head by the top heater simultaneously.

A temperature difference between the load (violet trace in fig. 4.29) and the medium (black, orange and green lines) was observed, depending on the applied heating power. This is likely to be caused by the temperature sensor being in direct contact with the copper block, where the heater is mounted. Therefore, direct heat transfer from the heater can be more effective than cooling by the flow. Thus the temperature difference itself is of less interest. More important is that when the load at the bottom exceeded the threshold of 10/12.5 W the system demonstrated unexpected behavior. The load was warming up, while the cold head and the condenser further cooled down, together with significant decrease of the flow rate. One can see the runaway event in more details in fig. 4.30. The decrease of the flow was developed further unless interrupted by applying more power to the top heater. Without rising the top heater power, the cold head was running to the freezing point of neon, cutting the circulation completely off by trapping neon on the cold surface. The load was continued to warm up if the applied heating was not reduced.

This behavior shows that the limitation originates not from the production rate of the cryogen and the overall cooling power of the system, but rather from the distribution and heat transfer at the load. As mentioned above, the shortcut, and especially the copper block where the bottom heater is installed, are rather short. The contact surface of the stream and the heated surface along the entire length of the copper block is only 4 cm^2 which, at the applied heating power, results in a heat flux up to $2.5\text{--}3 \text{ W/cm}^2$.

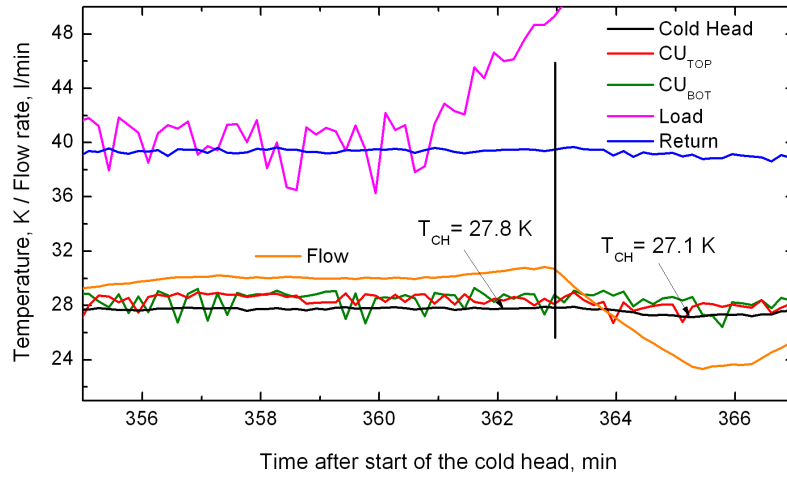


Figure 4.30: Runaway of the cooling system. After applying of excessive heating to the load it gets warmed up, while the flow rate and the temperature of the cold head decrease.

High heat flux can cause formation of an isolating gas layer between the solid surface and the cooling medium such that the cooling medium has no good thermal contact with the tube wall (similar to the Leidenfrost effect). This causes a sharp rise of the temperature difference between the solid and the cooling stream and degrades the heat transfer. The value of the critical heat flux reported for bath boiling of neon is 6 W/cm² [102] which is close to our measurements. Such a problem is encountered in both boiling bath and low-inventory cooling systems. For the low-inventory cooling systems like thermosyphons, which operate under conditions similar to the LPCS the problem is known as dry-out [97]. In the case of the LPCS it means that the cooling medium passed through the load region without significant heat transfer but caused excessive cooling in the heat exchanger. The consequences are warming up of the load and cooling of the condenser, as was observed in the experiments. In the further tests of the LPCS by using the larger superconductive magnet as a load it turned out that the contact surface of the heated coil frame and the stream was large enough to assure heat fluxes well below the critical value.

4.3.3 Joint test of the HTS magnet and the LPCS

The preparations of the joined test of the prototype HTS magnet and the LPCS cooling capacity included the following steps. The test magnet (see fig. 4.31) was equipped with the same heater as previously applied on the shortcut (b in fig. 4.31). On the outer surface of the magnet frame a PT1000 sensor was mounted (a in fig. 4.31). As the magnet was about to be tested at high current it required thick copper current lines from the cryogenic region to the outside (c in fig. 4.32). In the LPCS experiments, as opposed to later real operation of the complete electron cooler, there are no intermediate temperature regions where the current lines can be thermally anchored. Hence, they produce a significant heat leak which must be taken into account.

High current lines can be optimized in such a way, that the sum of the heat produced in the wire by resistive heating and that from the heat leak through its cross-section is minimized. The optimization algorithm is given in [84]. For our geometry we needed 1.5 m wires from the magnet suspension point in the middle of the CSR linear chamber to the electric feedthroughs on the side ISO-K 200 flange (see the magnet mounted inside of the chamber in fig. 4.32). The planned experimental current was 60 A. According to [84] the optimally sized copper wire to carry the current I from the room temperature region to the region of 30 K should have a cross-section area A which fulfills the criterion $LI/A \approx 4.5 \times 10^6$ A/m where L is the wire length. This gives $A = 20$ mm², so standard 25 mm² wires were used. The minimum heat input for the optimized wire from 290 K to 30 K is 40 mW/A, which for the pair of wires at 60 A gives 4.8 W. For the situation without electric current applied one can estimate the heat leak as $2A(\int_{30K}^{290K} KdT)/L$, where K is the thermal conductivity of copper and A is the actual cross-section of 25 mm². The integral $\int_{30K}^{290K} KdT$ according to [80] is 1320 W/cm, which gives a conductive heat leak of 4.4 W. To assure that this heat input is not applied to a too small surface and to provide mechanical support for the current lines without putting shear load on the coil feedthroughs, the lines were pressed by aluminum plates to the coil frame, with thick Kapton foil providing electrical isolation (see c in fig. 4.31). As the metalized superisolation is electrically conducting, all open electric contacts were isolated either by Kapton foil (feedthroughs, e in fig. 4.32) or spiral PE isolator (current lines). The absence of electric shortcuts was tested prior to the mounting of the coil and after installation in the chamber. The current leads were equipped with voltage contacts (g in fig. 4.31) to measure the coil resistance in a way similar to the liquid nitrogen experiment (see sec. 4.1.5). The cooling couplings were connected to the LPCS outputs by 60 cm flexible reinforced metal hoses (a in fig. 4.32). The test magnet and lines were isolated with 30 layers of superisolation. The magnet was suspended on 4 stainless steel wires (b in fig. 4.32) to the top flange of the linear chamber.

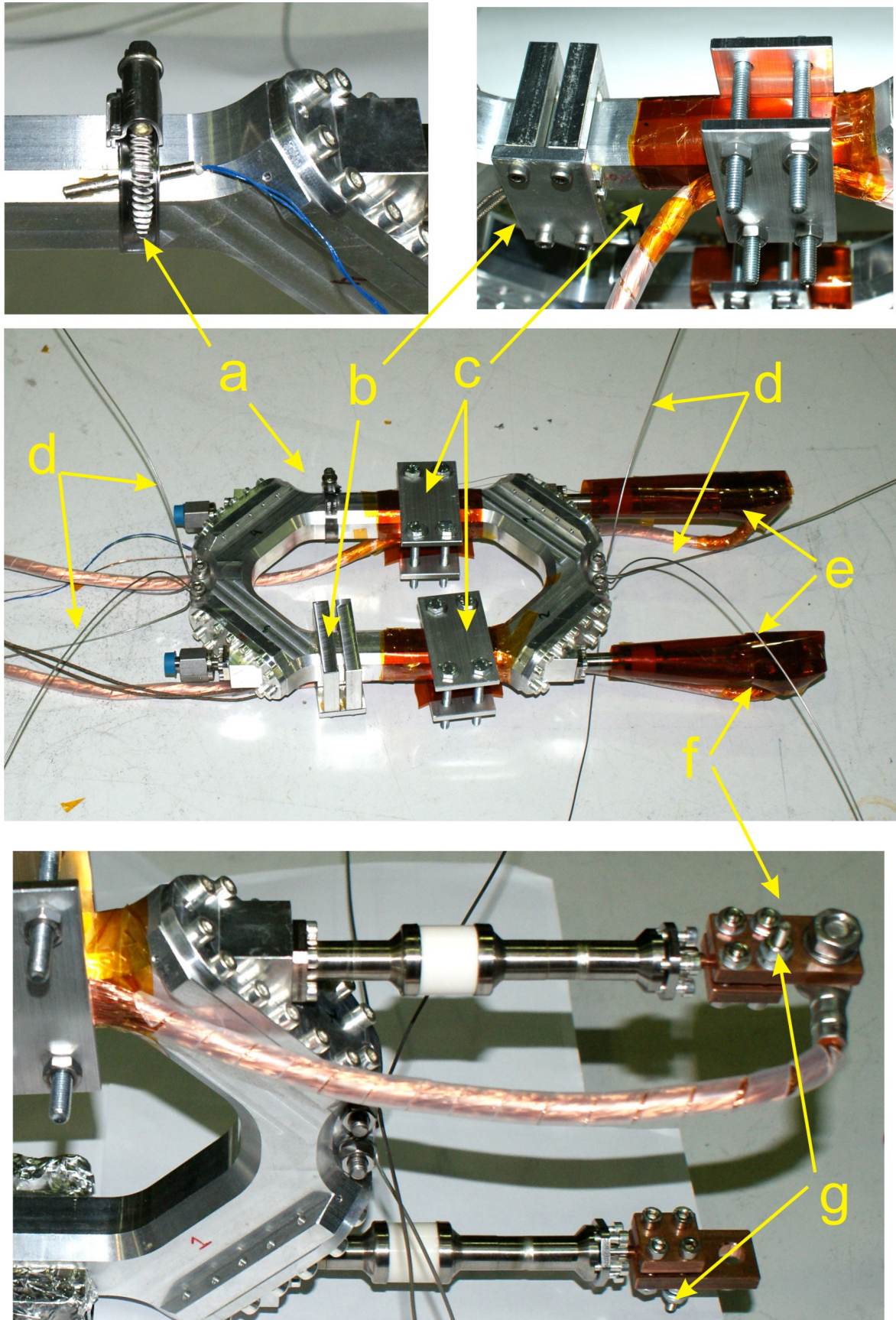


Figure 4.31: Preparation of the test magnet for cryogenic operation. a) PT1000 sensor, b) 100 W heating element (bottom heater) c) anchoring of copper current lines to the coil body through thick Kapton foil d) stainless steel suspension wires e) Kapton foil isolation around electric contacts f) current contacts. Two copper plates are pressed by 4 screws, one screw on each contact (g) is used to mount voltage contacts for resistance measurements.

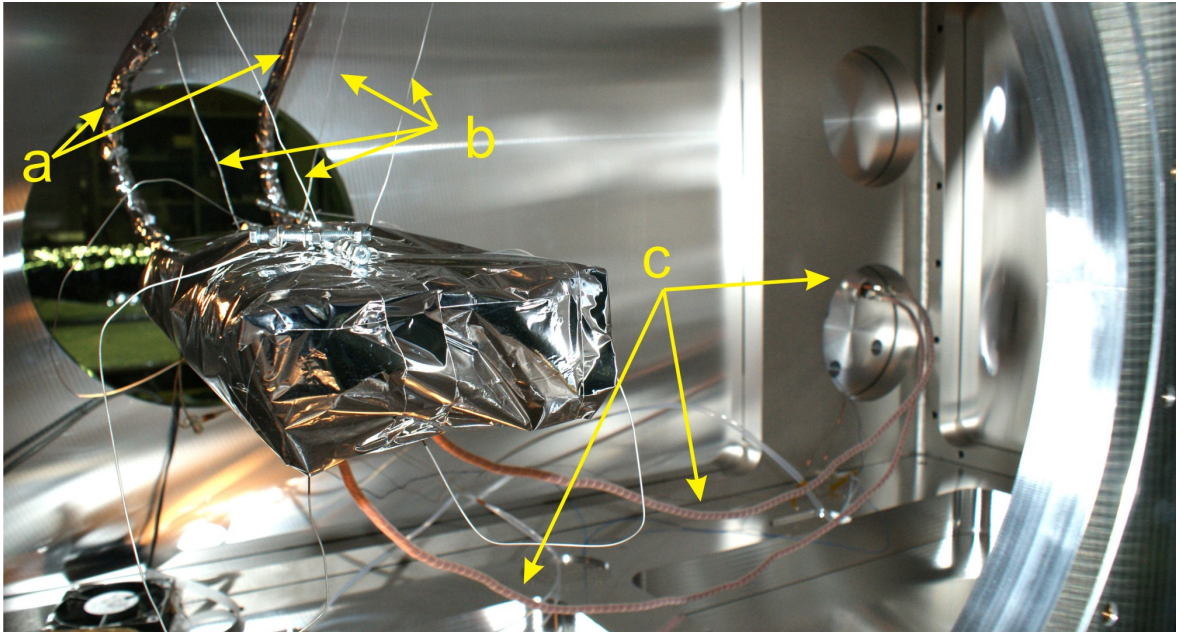


Figure 4.32: Mounting of the test magnet in the load cryostat chamber. a) flexible hose lines supplying neon, b) suspension wires mounted to the transition flange between the LPCS and the load cryostats, c) high current lines.

Check of cryogenic mechanics. A part of the test program was to demonstrate the vacuum tightness of the test magnet when the overpressure is applied from the inside under cryogenic conditions. To make this test the load cryostat was equipped with a quadrupole mass spectrometer (QMS) to look for the presence of neon in the vacuum system during the operation. The mass spectra were taken with the LPCS pumped down, with the LPCS pressurized with neon, during the cooling down process, operation of the system and after warming up. The mass spectra are given in fig. 4.33. One can see that the mass of 20 (the black arrow in fig. 4.33), possibly corresponding to neon, is present in the spectrum even when the LPCS is not filled with neon. The peak in the mass spectrum, however, can be attributed to doubly ionized ^{40}Ar , whose atmospheric abundance is 0.93% and therefore significant signal can be expected in the residual gas of a high vacuum chamber. In case of neon presence in the gas composition the heavier neon isotope ^{22}Ne with relative abundance of 10.2% [103] would have to be detected as well (the hypothetic magnitude of ^{22}Ne if the mass 20 signal is caused by ^{20}Ne is shown by the red arrow in fig. 4.33). However, the spectra exhibit no mass 22 signal of this magnitude. Comparing the mass spectra taken under varying conditions, one sees that in the absence of neon in the LPCS and with the pressurized and cooled system the mass 20 signals are two orders of magnitude lower than that of oxygen (32) and three orders of magnitude lower than that of water (18) and nitrogen (28). In addition, the intensity of the mass of interest approximately follows the change of the total vacuum pressure, which decreases from 3.1×10^{-6} mbar in the warm system to 2.5×10^{-6} mbar in the cold, with a short bump to 4.1×10^{-6} mbar, when the cooling is switched off (see fig. 4.34). Hence we conclude that the presence of neon under any pressure and temperature in the LPCS does not affect the residual gas composition. Thus we can state that the test magnet has no leaks in cryogenic operation and the mechanical concept is proven to be working.

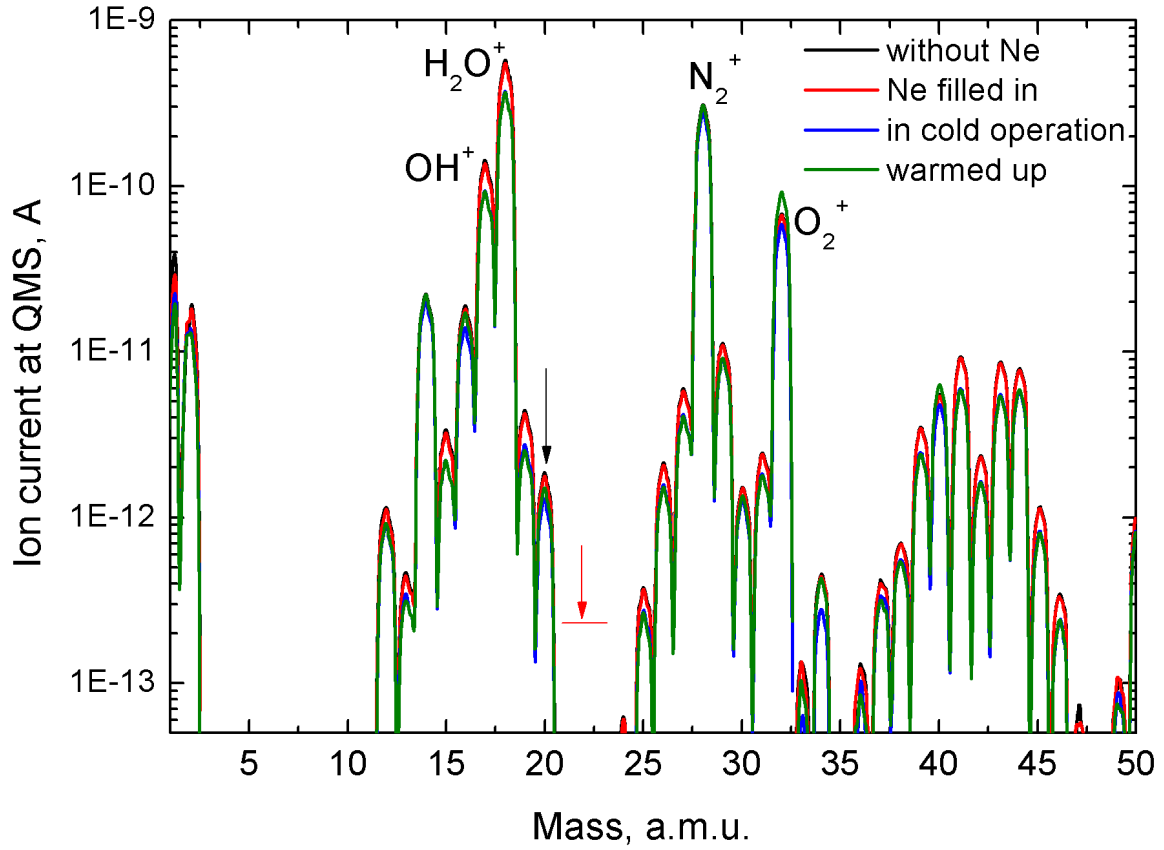


Figure 4.33: Mass spectra of the load chamber during the test of the magnet. The spectra taken at different stages of operation show no detectable changes in the residual gas composition associated with mass 20. The red arrow shows the position of ^{22}Ne signal if the mass 20 signal would be caused by the neon presence.

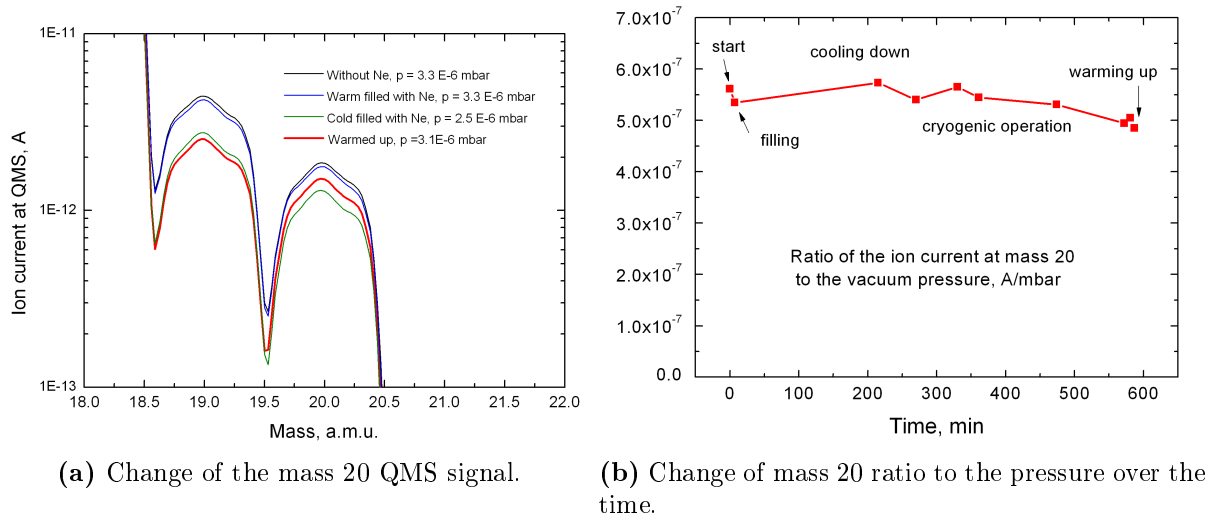


Figure 4.34: Left, change of the mass 20 QMS signal at the different moments of the operation cycle. Right, change of the ratio of the mass 20 QMS signal to the vacuum pressure in the load cryostat as a function of time.

LPCS cooling power. The cooling power tests were carried out in the same way as in the previous tests with the short cut. The LPCS was cooled down, the flow rate

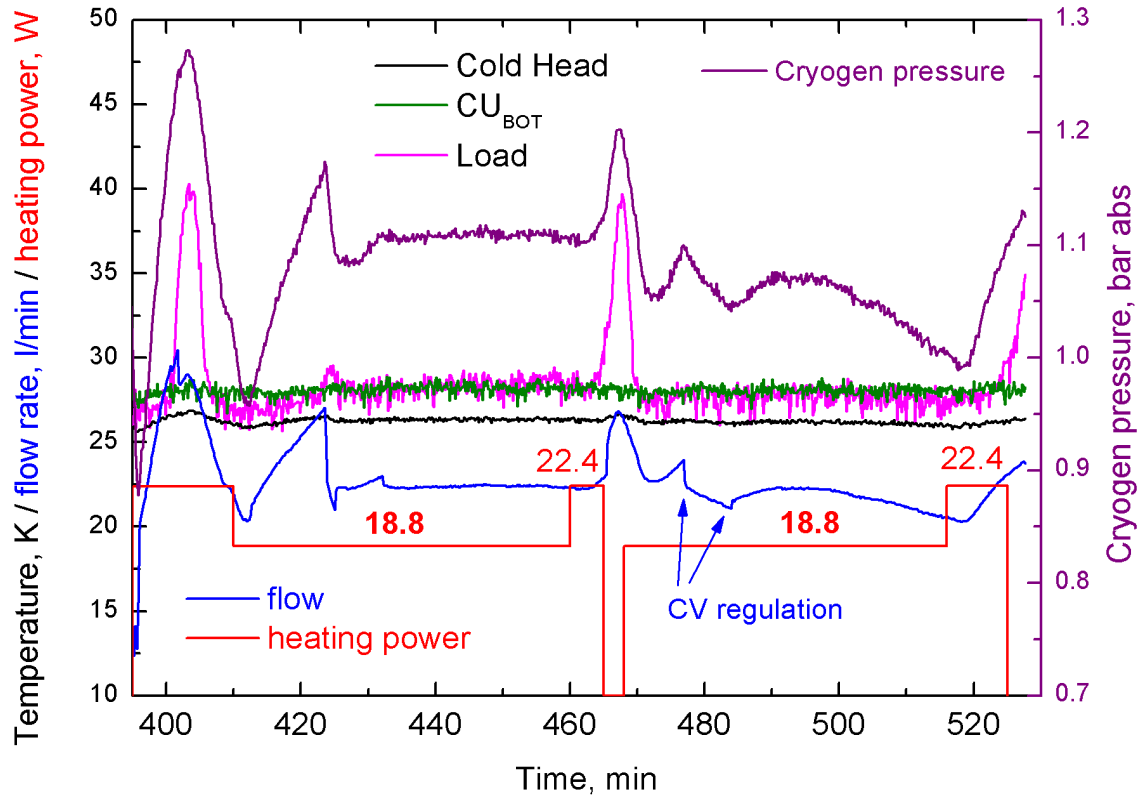


Figure 4.35: Transfer of the cooling power to the load at 1.1 bar working pressure.

was set by the control valve and the load applied by electric heating was gradually transferred from the top to the bottom heater while the temperature of the coil was kept constant at the 30 K level. There were two series of tests performed under different conditions. In the first series the working pressure in the cryogenic region was about 1.1 bar absolute, as set after initial filling of Ne gas. In the second test a series of Ne gas injections was performed in order to increase the amount of this medium in the circuit by a factor of 1.5 and to set the working cryogenic pressure to 1.5-1.6 bar. In both experiments complete transfer of the cooling power to the load was achieved; this is realized when no heating power is applied to the top heater and the bottom heater is at the maximum power. One can see the tests of maximum cooling power at normal pressure in fig. 4.35 and at elevated pressure in fig. 4.36. From these graphs we see that the cooling power of the cold head balances an electric heating power of 18.8 and 25.3 W, respectively, depending on the operation settings. The higher cooling power of 21.8 W in the second experiment before the additional gas injections, as compared to the first test, is due to an optimization of the flow rate, which was reduced from 22.4 to 18.9 l/min. In all cases, the calculated sum of ohmic and conductive load of 4-5 W from the current leads must be added to the full transferred cooling power.

In order to find out the cooling power used to pre-cool the neon after the heat exchanger to the boiling temperature a further test was performed (see fig. 4.37). Here the flow rate was changed to see how it affects the maximum power transferred to

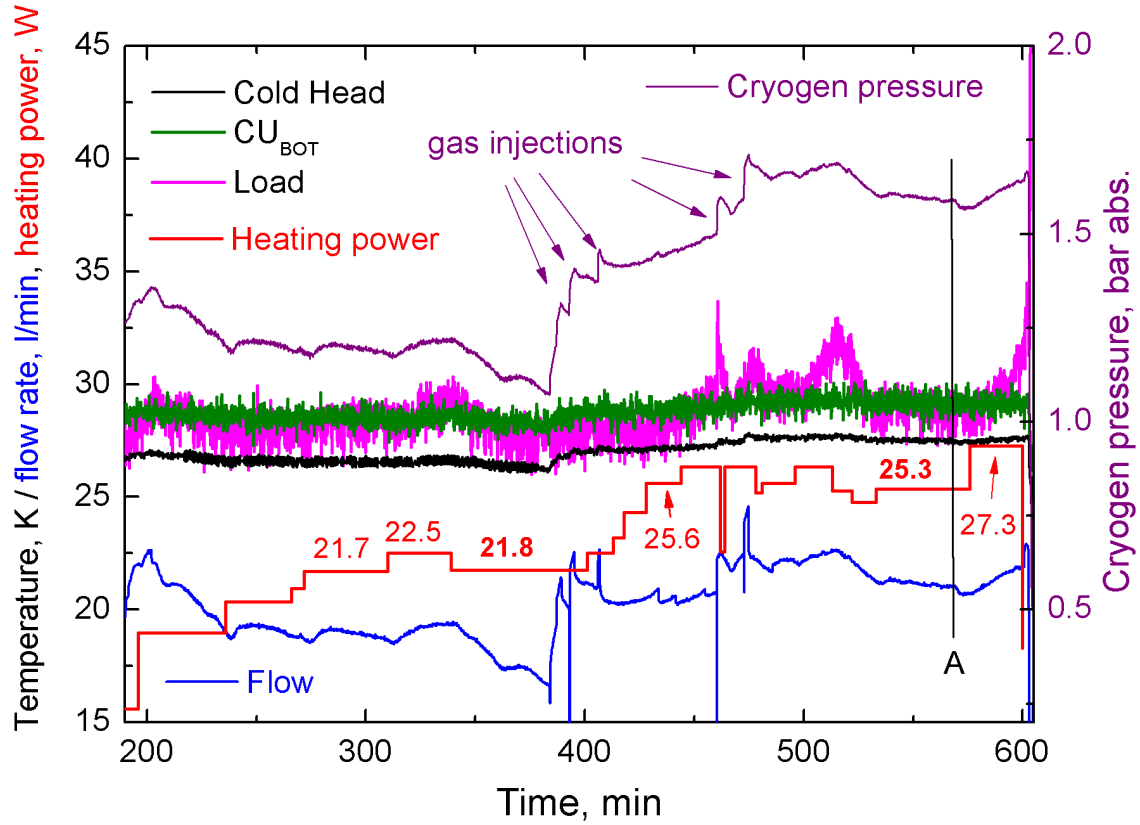


Figure 4.36: Transfer of the cooling power to the load at 1.5-1.6 bar working pressure after additional gas was injected to the cold system.

the load. For these measurements the LPCS was set to parameters similar to the parameters one can see at point A (~ 570 min) in fig. 4.36. The important parameters are the temperature of the cold head and the working pressure. By varying the flow rate and measuring the maximum transferred cooling power, as in the points B (~ 260 min) and C (~ 300 min) in fig. 4.37, one can find the absorbed cooling power as a function of the flow rate.

It was found that an increase of the flow rate from $f_1 = 21.1$ l/min (A) to $f_2 = 25.8$ l/min (B) and $f_3 = 26.3$ l/min (C) caused a reduction in transferred cooling power ΔP of 3.5 W as the additional amount of gas must be pre-cooled in the condenser unit and less cooling power is available for the condensation, therefore the fraction of the liquid phase in the flow is reduced. Averaging over the two measurements yields a value of the sensible heat $c_p \Delta T = \Delta P / \Delta \dot{m}$ gives a value of 48.6 J/g, which must be removed from the gas entering the condenser unit. Therefore for the flow of 0.32 g/s, corresponding to the operation with the maximum electric heating of 25.3 W (point A in fig. 4.36), the power used to pre-cool the gas in the condenser unit is 15.3 W. This together with the electric power of 25.3 W and the heat leak from the current leads of 4-5 W sums up to about 45-46 W of the total power (see summarized in table 4.3), which is close to the rated cooling capacity of the cold head at 27 K.

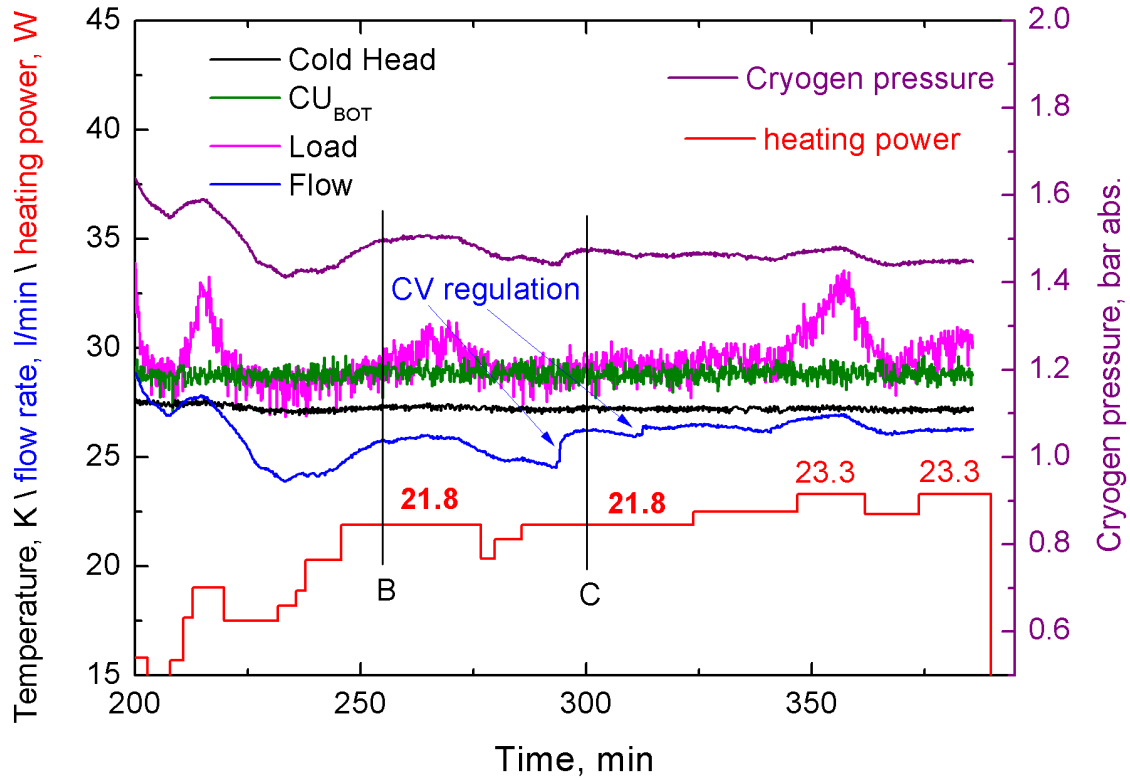


Figure 4.37: Test of the transferred cooling power as a function of the flow rate.

The power of 15.3 W used to pre-cool the gas flow of 0.32 g/s means that, given the specific heat of neon of $c_p = 1.040$ J/gK, the gas entering the condenser has a temperature 44.6 K above the boiling point (i.e. about 75 K). This is higher than the approach temperature of 10 K used in the design of the exchanger (see sec. 4.2.2). The reason explaining the discrepancy is that the temperature of the return flow is higher than used in the design. The return flow temperature measured in experiments is 45-50 K whereas the value of 30 K was used in the design. The reason for the return line to be warmer are the cryogenic feedthroughs between the two cryostats. The two temperature sensors installed on the top flanges of these feedthroughs show that their temperatures are 45 and 80 K for the in- and out- feedthroughs, respectively. The flanges are warmer than the parts of the circuit up- and downstream from both of them. This means that their temperature is defined by some heat leaks from the bottom flange of the room temperature vacuum chamber. Therefore an improvement of the cooling power is possible if the feedthrough will be optimized for better thermoisolation. Any reduction of the heat leak in this region will result in a doubled gain of the available cooling power. The factor of two originates from the fact that not only part of the transferred cooling energy is leaking through the thermal bridges, this part also gets subtracted from the cooling energy available in the heat exchanger. Apart from these heat leaks, the operation test of the LPCS can be considered successful as the cooling power of about 30 W delivered to the load exceeds the estimation of the needed power

Table 4.3: Cooling power balance for operation at the 30 K load temperature.

Contribution	Power, W
Required for copper magnets	20 W
a Electric heating used in tests	21.8-25.3 W
b Current leads heat leaks	4-5 W
Total delivered to the load at 30 K, a+b	25.8 - 30.3 W
c Pre-cooling of Ne	15.3 W
Total cooling power attributed, a+b+c	~45.6 W
Rated power of the cold head	~ 50 W

by a factor of 1.5.

HTS magnet operation. The prototype HTS magnet was operated during the tests, and in no cases any additional heat load was observed in the system. The first operation was started in gas cooling mode at the coil temperature of 60 K and repeated at the normal operation temperature of 30 K. The measured resistance of the test magnet at 30 K under 60 A current was $15 \mu\Omega$ ($23 \mu\Omega$ at 60 K under 60 A), close to that in the liquid nitrogen test (see sec. 4.1.5). Therefore we can state that the cooling of the coil was as effective as when immersed in a bath of cryogen for both two-phase and gas cooling modes. A Hall probe outside of the linear chamber detected the magnetic field produced by the coil. A field of 0.02 ± 0.005 mT (0.2 ± 0.05 G) was measured about half a meter from the coil in horizontal plane (in terms of fig. 4.38a at the point (0,0,50)), and 0.03 ± 0.005 mT at a point 50 cm above on the side of the LPCS cryostat tower (15,50,15). These two point are the closest to the coil placements for the Hall probe outside of the vacuum chamber. Comparing measured data to the coil geometry from the numeric field model scaled to the parameters of the prototype coil (19 turns, 60 A) we get the graph shown in fig. 4.38b. The dipole fields decreases very strong with the distance. While under the given setting the field in the middle of the coil is 92 G, the field measured at the point (0,0,50) is only 0.227 G, which is close to measured value. The calculated value for the field at the point (15,50,15) is 0.0298 mT.

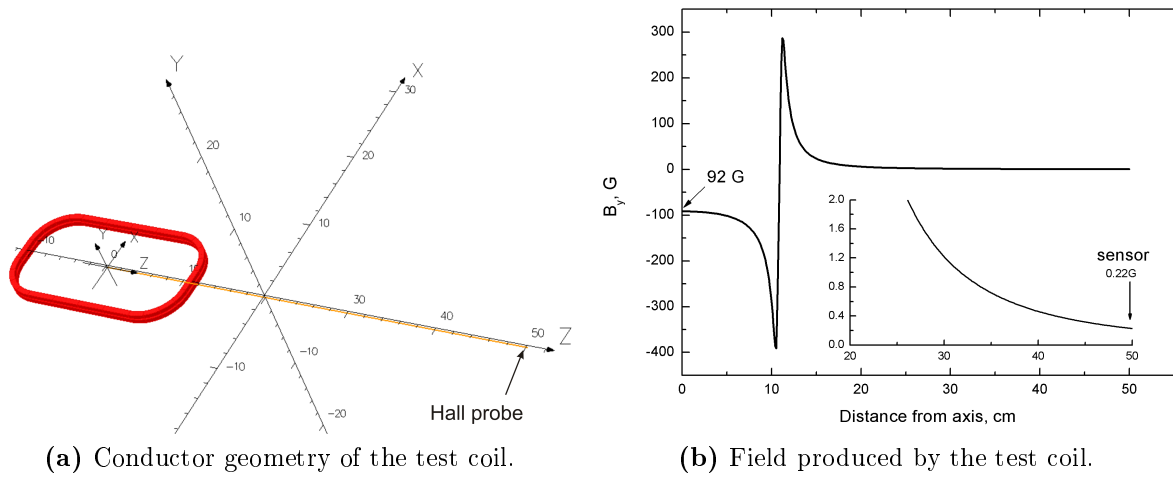


Figure 4.38: Numerically calculated field strength of the prototype coil in the far range. The figure on the left shows the position of the measurement axis as compared to the conductor geometry, dimensions in cm. The plot on the right shows the magnetic field strength along the specified above line. The insert shows the far field region with the necessary magnification.

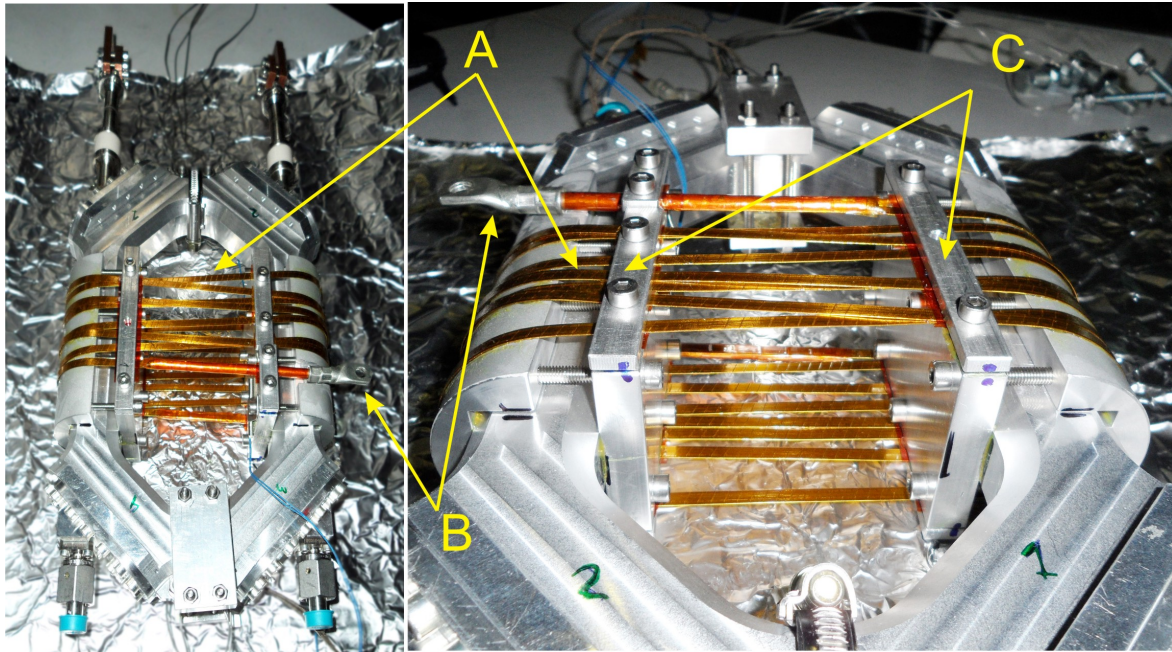


Figure 4.39: Test of a conductively cooled HTS prototype coil. A) HTS turns, B) high current contacts, C) the only pressed thermal contacts to the cooled surface.

Conductively cooled magnet. The realization of the large scale magnets denoted previously as MS, RS, THS and TSV is not covered in this work. However a series of tests on the LPCS and the test coil were completed. In these tests a prototype coil simulating a conductively cooled HTS magnet with sparse thermal contacts was studied (see fig. 4.39).

The new coil is wound on the outer surface of the prototype HTS compensator coil equipped with special side profiles. The outer winding is cooled only by conductive heat transfer in the regions of pressed aluminum contacts (C in fig. 4.39), thus this device is later referred to as dry magnet. The pressed contacts are mounted on the side

profiles made of two pieces squeezing the long bars of the test coil frame. The coil was isolated with 30 layers of superisolation, connected to the same current lines used in the previous tests and cooled by the LPCS. The resistance of the coil was measured under currents up to 80 A. The total resistance was measured to be $200 \mu\Omega$, which is higher than in the test with medium cooled HTS. This can be explained by two additional pressed electric contacts in the system and smaller contact surface of these contacts. The additional contact compared to the previous test are the cable shoes (C) on the copper bars soldered to the HTS wire. The resistance however remained in the range expected for contact resistance. A sharp rise of the resistance at the temperature close to the transition point was observed and confirms that the HTS was superconducting below (see fig. 4.40). The temperature of the coil frame when the transition is taking place is about 10 K lower than the transition point, however the HTS material itself is warmer due to the contact to the current leads and higher temperature of the side profiles compared to the coil frame.

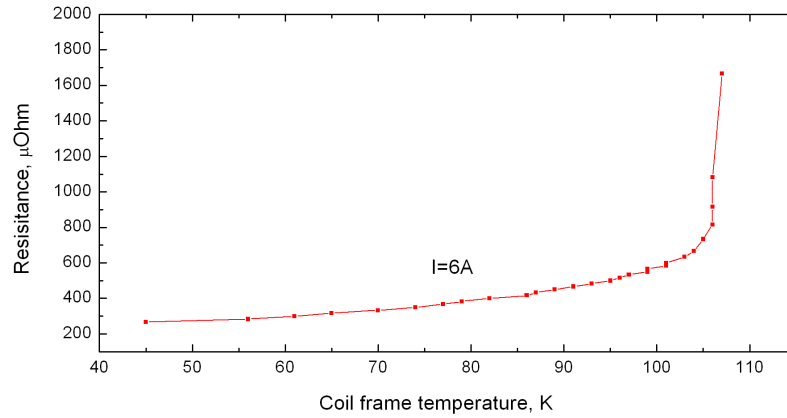


Figure 4.40: Resistance of the conductively cooled prototype coil during the warming up. The resistance measured under 6 A current after the cold head was stopped. Data by S. Vogel.

4.4 Summary of the cryogenic tests

In the series of tests described in this section the performances of the prototype HTS magnet and the LPCS were tested. The mechanical concept of the magnet was proven to be working as it demonstrated vacuum tightness and the ability to carry the design current of 60 A in realistic operation conditions. The LPCS demonstrated its ability to deliver a cooling power of 24-30 W (see table 4.3) to the load depending on operation settings, which exceeds estimated requirement for the electron cooler magnet system (see table 4.2). As all the tests were performed as one day experiments from cooling down to turning off the cold head, it is necessary to mention a few upgrades which will be needed to enable continuous operation of the LPCS. As it was already mentioned the Vakuubrand ME 4R NT compressors loose the cooling medium and for continuous operation it is preferable to replace them with more tight devices. The second point

concerns the control of the system. The key parameter to operate the LPCS in the narrow temperature gap between condensation of neon and its freezing is to set proper heating conditions and then maintain a constant flow. This was successfully achieved and allowed to run the system stable without adjusting the valve for hours. However, small disbalance in the loads can be expected to lead to slow drifts of the flow rates and pressures, which have tendency to give rise to runaway processes if not corrected. Therefore the manual control valve (CV in fig. 4.26) should be replaced by an automatic valve getting a slow feedback from the MFM and the cold head temperature for automated continuous operation.

Based on experiments on the prototype cryogen-filled coil and the dry test magnet the final decision was made to build the rest of the magnets of the electron cooler (MS, RS, THS and TSV) as conductively cooled superconductive magnets. The main principle of these dry magnets is that the wire is wound on a heat conducting metal supporting structure and is periodically pressed to it by thermal contacts. The supporting structure is cooled by the LPCS.

Chapter 5

Summary and outlook

For the cryogenic ion storage ring efficient phase space cooling by electrons opens many new possibilities. The challenges of realizing an electron cooling device working at ultra-low energies and under cryogenic conditions were addressed in this work. An electron cooler complying with the CSR experimental conditions is a wide energy range device covering the electron energy interval from 1 to 1000 eV, providing sufficient electron current at any energy in that range and able to operate in the cryogenic environment, although partly independent from the operation of the CSR cooling circuit. This work demonstrated the feasibility of dense ultra-low energy electron beams and presented the design concept of the electron cooler together with prototypes of some of its key components which were successfully built and taken in operation.

For the first time, an ultra-low energy electron beam of suitable quality at electron energies below 10 eV down to a fraction of eV was demonstrated in experiments at the TSR electron target with the cryogenic photocathode electron source. The applied beam deceleration technique could be used to achieve defined beam transport under conditions of well-controlled space-charge and contact potentials, which otherwise introduce large uncertainties for few-eV electron energies and below. The electron beam density was increased by an order of magnitude while keeping the proper beam quality. Such increase of the electron density makes it possible to perform electron cooling of heaviest ion species up to 160 a.m.u. mass, which strongly profits from the enhanced beam density.

A mechanically realistic design of the guiding magnetic system of the cooler was developed and numerically modeled. The field geometry was adapted in a way to make it more suitable for low energy electrons and ions. The guiding system features a novel toroid-free merging scheme complying with low energy ions in an electrostatic storage ring and operates at the optimal field strength providing safe electron transport while minimizing the influence on the ion beam. The magnet design provides sufficient access to the internal beam line structures to bring in the cryogenic cooling, mechanical support and outer connections, enables both cryogenic and warm operation by keeping sufficient space for thermal isolation and decoupling between the components and

provides the magnetic field fulfilling the quality requirements for the desired electron cooler operation.

The conductor geometries established in the model were used to develop mechanical concepts of the magnets and specify the requirements to the cryogenic cooling system for the magnets. The magnets were divided in two groups depending on the winding density. For the first group (cryogen-filled) the superconductive realization was found to be of greatest advantage, whereas the second group could be realized either as superconductive or resistive, depending on providing proper cooling to these magnets by means of thermal conductance (dry magnets). A prototype cryogen-filled HTS magnet representing the mechanical solution for 16 out of 25 guiding magnets of the model was built and successfully taken in operation. The tests proved the mechanical solution to be working at the cryogenic and vacuum conditions of the future CSR electron cooler. Further tests on conductively cooled HTS magnets proved the feasibility of such a solution for the rest of the guiding magnets present in the guiding magnetic system. Thus, the final design of the guiding system was established as based on both cryogen-filled and conductively cooled HTS magnets.

In order to carry out the tests of prototypes and later serve in the complete cooler, a low pressure cryogenic cooling system (LPCS) was designed, built, tested and taken into operation. The operation principle of the LPCS is based on forced circulation of neon at a few bar pressure undergoing the liquid-to-gas transition at ~ 30 K. The LPCS was designed to support the magnet operation keeping the option to build the dry magnets out of copper wire. This put a constraint of 20 W of the cooling power at a stable temperature of 30 K. The built system surpassed the cooling power limit with a factor of 1.5 safety margin by delivering in the tests at 30 K temperature 25-30 W of cooling power, depending on the operation settings. The system demonstrated its ability to stably operate at a very low cryogen inventory of 30-40 g in the entire volume, most of which remains in the heat exchanger and the room temperature buffer. It also demonstrated flexible operation in a wide range of gas flow regimes at different fractions of the liquid phase in the cold flow, including operation at flows exceeding the normal operation flow by a factor of 3.3. As the magnet realization was established as entirely superconductive, the demand of the cooling power and the temperature stability requirements are now eased, however having additional cooling power available allows to keep a safety margin to account for minor thermal leaks or imperfections in the radiative thermoinsulation.

With its key design concepts developed and tested, the further construction of the cooler can be started up rapidly, being now mainly a technical effort. According to the actual schedule the cooler is expected to be commissioned together with the CSR to store its first beam in 2013. When built, the CSR electron cooler, based on the results reported here, will open new experimental opportunities for molecular physics. By combining multiple advances compared to previous early attempts of electron cooling at

ultra-low energies, including one order of magnitude improvements in electron density and temperatures, together with two orders of magnitude enhancement of the ion beam lifetime, it will be possible to address experimental problems on complex heavy ions stored at energies of 2-12 keV per nucleon. This opens a new range to extend state-of-the-art molecular physics experiments, already performed at the TSR, towards more complex ions, including organic species now beyond the reach of storage ring experiments.

Electron cooling is required for most of these experiments as a tool to prolong the ion storage, while in collision experiments the electron beam interacts with the ion beam directly. Long ion storage in a cryogenic environment gives the unique opportunity to apply in such experiments a stored ion beam with a rovibrational state population close to the ground state. It is a perfect benchmark to extend and improve theoretical molecular physics as calculations can be compared to more conclusive state-controlled experimental data. Such an advance in molecular physics is not limited to the processes taking place under the conditions similar to the experimental settings of the CSR, but the obtained theoretical understanding will result in a fundamental progress of molecular physics.

A special place in the row of the future research goals for the CSR is associated with the study of organic molecules in ISM-relevant conditions. These experiments will bring us closer to the understanding how such organic molecules are formed in space from inorganic matter, which molecules can be formed, in which reactions and at which rate and how the reaction chains look like. This brings us to such a general question as the origin of life and its spreading in the universe. The organic matter of cosmic origin transported by comets is now considered as one of the primary sources of organic molecules and biologic monomers such as amino-acids on the prebiotic Earth [104]. Understanding the basic reaction paths governing the organic chemistry in ISM conditions will be a big step towards understanding the role of space-born organic matter in the origin of life and its occurrence in the universe.

Bibliography

- [1] Herbst, E. and Van Dishoeck, E. F. (2009) Complex organic interstellar molecules. vol. 47 of *Annual Review of Astronomy and Astrophysics*, pp. 427–480.
- [2] Herbst, E. and Klemperer, W. (1973) Formation and depletion of molecules in dense interstellar clouds. *Astrophys. J.*, **185**, 505–533.
- [3] McCarthy, M. C., Gottlieb, C. A., Gupta, H., and Thaddeus, P. (2006) Laboratory and astronomical identification of the negative molecular ion C_6H^- . *Astrophys. J. Lett.*, **652**, 141–144.
- [4] Smith, I. W. M. (2011) Laboratory Astrochemistry: Gas-Phase Processes. *Annual Review of Astronomy and Astrophysics*, vol. 49 of *Annual Review of Astronomy and Astrophysics*, pp. 29–66, Annual Reviews.
- [5] Bryans, P., Landi, E., and Savin, D. W. (2009) A new approach to analyzing solar coronal spectra and updated collisional ionization equilibrium calculations. II. Updated ionization rate coefficients. *Astrophys. J.*, **691**, 1540–1559.
- [6] de Heer, W. A. (1993) The physics of simple metal clusters: experimental aspects and simple models. *Rev. Mod. Phys.*, **65**, 611–676.
- [7] Froese, M. W., et al. (2011) Thermionic power-law decay of excited aluminum-cluster anions and its dependence on storage-device temperature. *Phys. Rev. A*, **83**, 023202.
- [8] Hansen, K., Andersen, J. U., Forster, J. S., and Hvelplund, P. (2001) Formation and fragmentation of negative metal clusters. *Phys. Rev. A*, **63**, 1–8.
- [9] Andersen, J. U., Gottrup, C., Hansen, K., Hvelplund, P., and Larsson, M. O. (2001) Radiative cooling of fullerene anions in a storage ring. *Europ. Phys. J. D*, **17**, 189–204.
- [10] Buhr, H., et al. (2008) Inelastic electron collisions of the isotopically symmetric helium dimer ion $^4\text{He}_2^+$ in a storage ring. *Phys. Rev. A*, **77**, 032719.
- [11] Novotny, O., et al. (2009) Dissociative recombination of CF^+ : experiment and theory. *J. of Phys. Conf. Ser.*, **192**, 012021.

- [12] Petrignani, A., et al. (2009) Spectroscopy and dissociative recombination of the lowest rotational states of H_3^+ . *J. of Phys. Conf. Ser.*, **192**, 012022.
- [13] Buhr, H., et al. (2010) Hot water molecules from dissociative recombination of D_3O^+ with cold electrons. *Phys. Rev. Lett.*, **105**, 103202.
- [14] Nordhorn, C., et al. (2011) Branching ratios in dissociative recombination of formyl and isoformyl cations. *J. of Phys. Conf. Ser.*, **300**, 012004.
- [15] Mendes, M. B., et al. (2012) Cold electron reactions producing the energetic isomer of hydrogen cyanide in interstellar clouds. *Astrophys. J. Lett.*, **746**, L8.
- [16] Stützel, J., et al. (2009) Fragmentation by electron recombination for HF^+ and CF^+ . *J. of Phys. Conf. Ser.*, **194**, 062028.
- [17] Hahn, M., Bernhardt, D., Lestinsky, M., Müller, A., Novotný, O., Schippers, S., Wolf, A., and Savin, D. W. (2010) Storage ring measurement of electron impact ionization for Mg^{7+} forming Mg^{8+} . *Astrophys. J.*, **712**, 1166.
- [18] Hahn, M., et al. (2011) Storage ring cross section measurements for electron impact ionization of Fe^{11+} forming Fe^{12+} and Fe^{13+} . *Astrophys. J.*, **729**, 76.
- [19] Schippers, S., et al. (2011) Dielectronic recombination of xenonlike tungsten ions. *Phys. Rev. A*, **83**, 012711.
- [20] Schmidt, E. W., Bernhardt, D., Hoffmann, J., Lestinsky, M., Lukić, D. V., Müller, A., Orlov, D. A., Savin, D. W., Schippers, S., and Wolf, A. (2009) Experimental rate coefficient for dielectronic recombination of neonlike iron forming sodiumlike iron. *J. of Phys. Conf. Ser.*, **163**, 012028.
- [21] Lestinsky, M., et al. (2009) Electron-ion recombination of Fe X forming Fe IX and of Fe XI forming Fe X: Laboratory measurements and theoretical calculations. *Astrophys. J.*, **698**, 648.
- [22] Baumann, P., et al. (1988) The Heidelberg heavy ion Test Storage Ring TSR. *Nuc. Inst. and Meth. A*, **268**, 531–537.
- [23] Møller, S. P. (1993) The Aarhus SStorageRing for ions and electrons ASTRID. *Proceedings of particle accelerator conference 1993*, pp. 1741–1743.
- [24] Shirai, T., et al. (2004) S-LSR: test ring for beam crystal, its design and ordering simulation. *Nuc. Inst. and Meth. A*, **532**, 488–491.
- [25] Møller, S. P. (1994) Recent developments in small cooling rings. *Proceedings of European particle accelerator conference 1994*, pp. 173–177.

- [26] Schlachter, A. S., Stearns, J. W., Graham, W. G., Berkner, K. H., Pyle, R. V., and Tanis, J. A. (1983) Electron capture for fast highly charged ions in gas targets: An empirical scaling rule. *Phys. Rev. A*, **27**, 3372–3374.
- [27] Andersen, T., Andersen, L. H., Balling, P., Haugen, H. K., Hvelplund, P., Smith, W. W., and Taulbjerg, K. (1993) Metastable-ion lifetime studies utilizing a heavy-ion storage ring : Measurements on He^- . *Phys. Rev. A*, **47**, 890–896.
- [28] Froese, M., et al. (2009) Cryogenic ion beam storage. *Proceedings of particle accelerator conference 2009*, pp. 4860–4862.
- [29] Welsch, C. P., Harasimowicz, J., Kühnel, K. U., Papash, A., Putignano, M., Schmidt, P., and Ullrich, J. (2009) Present status of the USR project. *Hyperfine Interactions*, **194**, 137–143.
- [30] Löfgren, P. L., et al. (2006) Design of the double electrostatic storage ring DESIREE. *Proceedings of European particle accelerator conference 2006*, pp. 252–254.
- [31] Schmidt, H. T., et al. (2009) The DESIREE project - a status report. *J. of Phys. Conf. Ser.*, **194**, 142013.
- [32] Stiebing, K. E., et al. (2010) FLSR - The Frankfurt low energy storage ring. *Nuc. Inst. and Meth. A*, **614**, 10–16.
- [33] Jinno, S., Takao, T., Omata, Y., Satou, A., Tanuma, H., Azuma, T., Shiromaru, H., Okuno, K., Kobayashi, N., and Watanabe, I. (2004) TMU electrostatic ion storage ring design for operation at liquid nitrogen temperature. *Nuc. Inst. and Meth. A*, **532**, 477–482.
- [34] Tanabe, T., Chida, K., Noda, K., and Watanabe, I. (2002) An electrostatic storage ring for atomic and molecular science. *Nuc. Inst. and Meth. A*, **482**, 595–605.
- [35] Tanabe, T., Noda, K., and Syresin, E. (2004) An electrostatic storage ring with a merging electron beam device at KEK. *Nuc. Inst. and Meth. A*, **532**, 105–110.
- [36] Møller, S. P. (1997) ELISA, an electrostatic storage ring for atomic physics. *Nuc. Inst. and Meth. A*, **394**, 281–286.
- [37] Bernard, J., Montagne, G., Brèdy, R., Terpend-Ordacièrre, B., Bourgey, A., Kerleroux, M., Chen, L., Schmidt, H. T., Cederquist, H., and Martin, S. (2008) A "tabletop" electrostatic ion storage ring: Mini-ring. *Rev. of Sci. Inst.*, **79**, 075109.

- [38] Danared, H. (2008) Applicability of stochastic cooling to small electrostatic storage rings. *Proceedings of European particle accelerator conference 2008*, pp. 3464–3466.
- [39] Berg, F. (2011) *Die Ionenoptik der Injektionsstrahlführungslinien des kryogenen Speicherrings CSR*. Master's thesis, Ruprecht Karl Universität Heidelberg.
- [40] Laux, F. (2011) *Entwicklung von kapazitiven Positions-, Strom- und Schotkysignal-Messsystemen für den kryogenen Speicherring CSR*. Ph.D. thesis, Ruprecht Karl Universität Heidelberg.
- [41] Kühnel, K., Putignano, M., Welsch, C., Schröter, C., and Ullrich, J. (2008) A novel beam profile monitor based on a supersonic gas jet. *Proceedings of European particle accelerator conference 2008*, pp. 1182–1184.
- [42] Grieser, M., Habs, D., Hahn, R. v., Kleffner, C. M., Repnow, R., Stampfer, M., Jaeschke, E., and Steck, M. (1993) Advanced stacking methods using electron cooling at the TSR Heidelberg. *Proceedings of particle accelerator conference 1991*, pp. 2817–2819.
- [43] Tanabe, T. and Noda, K. (2003) Storage of bio-molecular ions in the electrostatic storage ring. *Nuc. Inst. and Meth. A*, **496**, 233–237.
- [44] Amitay, Z., Zajfman, D., and Forck, P. (1994) Rotational and vibrational lifetime of isotopically asymmetrized homonuclear diatomic molecular ions. *Phys. Rev. A*, **50**, 2304–2308.
- [45] Mendes, M. (2009) *Molecular fragmentation by recombination with cold electrons studied with a mass sensitive imaging detector*. Ph.D. thesis, Ruprecht Karl Universität Heidelberg.
- [46] Day, C. (2007) Basics and applications of cryopumps. *CERN accelerator school. Vacuum in Accelerators*, pp. 241–274.
- [47] von Hahn, R., et al. (2011) The electrostatic Cryogenic Storage Ring CSR - Mechanical concept and realization. *Nuc. Inst. and Meth. B*, **269**, 2871–2874.
- [48] Lange, M., et al. (2010) A cryogenic electrostatic trap for long-time storage of kev ion beams. *Rev. of Sci. Inst.*, **81**, 055105.
- [49] Orlov, D. A., Lange, M., Froese, M., Hahn, R. v., Grieser, M., Mallinger, V., Rappaport, M., Sieber, T., Weber, T., and Wolff, A. (2008) Cryogenic and vacuum technological aspects of the low-energy electrostatic Cryogenic Storage Ring. *Advances in cryogenic Engineering: Transactions of the Cryogenic Engineering Conference - CEC*, **53**, 1233–1239.

- [50] Courant, E. and Snyder, H. (1958) Theory of the alternating-gradient synchrotron. *Annals of physics*, **3**, 1–48.
- [51] Fadil, H., Grieser, M., von Hahn, R., Orlov, D. A., Schwalm, D., Wolf, A., and Zajfman, D. (2005) Low energy electron cooling and accelerator physics for the heidelberg CSR. *AIP Conf. Proc.*, vol. 821, pp. 346–350.
- [52] Budker, G. I. (1968) An effective method of damping particle oscillations in proton and antiproton storage rings. *Soviet Atomic Energy*, **22**, 438–440.
- [53] Budker, G. I., Derbenev, Y. S., Dikansky, N. S., Kudelainen, V. I., Meshkov, I. N., Parkhomchuk, V. V., Pestrikov, D. V., Sukhina, B. N., and Skrinsky, A. N. (1975) Experiments on electron cooling. *IEEE Trans. on Nuclear Science*, **22**, 2093–2097.
- [54] Poth, H. (1990) Electron cooling: Theory, experiment, application. *Physics Report*, **196**, 135–297.
- [55] Pierce, J. R. (1954) *Theory and design of electron beams*. D. van Nostrand company inc., second edn.
- [56] Danared, H. (1993) Electron cooling at CRYRING. *Physica Scripta*, **48**, 405–412.
- [57] Andler, G., et al. (2000) Extending the use of the CRYRING storage ring. *Proceedings of European particle accelerator conference 2000*, pp. 545–547.
- [58] Sprenger, F., Lestinsky, M., Orlov, D. A., Schwalm, D., and Wolf, A. (2004) The high-resolution electron-ion collision facility at TSR. *Nuc. Inst. and Meth. A*, **532**, 298–302.
- [59] Krantz, C. (2009) *Intense electron beams from GaAs photocathodes as a tool for molecular and atomic physics*. Ph.D. thesis, Ruprecht Karl Universität Heidelberg.
- [60] Meshkov, I. and Sidorin, A. (2004) Electron cooling. *Nuc. Inst. and Meth. A*, **532**, 19–25.
- [61] Nagaitsev, S., et al. (2006) Antiproton cooling in the Fermilab recycler ring. *AIP Conf. Proc.*, vol. 821, pp. 39–47.
- [62] Calabrese, R., Kudelainen, V., Novokhatsky, A., and Tecchio, L. (1990) A high-intensity electron source from GaAs. *Measurement Science and Technology*, **1**, 665–666.
- [63] Habs, D., Kramp, J., Matl, P. K. K., Neumann, R., and Schwalm, D. (1988) Ultracold ordered electron beam. *Physica Scripta*, **T22**, 269–276.

- [64] Scheer, J. J. and van Laar, J. (1965) GaAs-Cs: A new type of photoemitter. *Solid State Comm.*, **3**, 189–193.
- [65] Bell, R. L. (1973) *Negative electron affinity devices*. Clarendon Press.
- [66] Bradley, D. J., Allenson, M. B., and Holeman, B. R. (1977) The transverse energy of electrons emitted from gaas photocathodes. *J. of Phys. D*, **10**, 111–125.
- [67] Orlov, D. A., Hoppe, M., Weigel, U., Schwalm, D., Terekhov, A. S., and Wolf, A. (2001) Energy distributions of electrons emitted from GaAs(Cs,O). *App. Phys. Lett.*, **78**, 2721–2723.
- [68] Weigel, U. (2003) *Cold intense electron beams from gallium arsenide photocathodes*. Ph.D. thesis, Ruprecht Karl Universität Heidelberg.
- [69] Orlov, D., Weigel, U., Schwalm, D., Terekhov, A., and Wolf, A. (2004) Ultra-cold electron source with a GaAs-photocathode. *Nuc. Inst. and Meth. A*, **532**, 418–421.
- [70] Orlov, D. A., Weigel, U., Hoppe, M., Schwalm, D., Jaroshevich, A. S., Terekhov, A. S., and Wolf, A. (2003) Cold electrons from cryogenic GaAs photocathodes: energetic and angular distributions. *Hyperfine Interactions*, **146**, 215–218.
- [71] Spitzer, Jr., L. (1962) *Physics of fully ionized gases*. Interscience publishers a division of John Wiley & Sons.
- [72] Smith, L. P. and Hartman, P. L. (1940) The formation and maintenance of electron and ion beams. *J. of App. Phys.*, **11**, 220–229.
- [73] Caulton, M. (1965) Retarding-field analyzers for the measurement of axial-velocity distributions in electron beams. *RCA Rev.*, **26**, 217–241.
- [74] Aleksandrov, A. V., et al. (1992) Relaxations in electron beams and adiabatic acceleration. *Phys. Rev. A*, **46**, 6628–6633.
- [75] Dikansky, N. S., Kudelainen, V. I., Lebedev, V. A., Meshkov, I. N., Parkhomchuk, V. V., Seryj, A. A., Skrinsky, A. N., and Sukhina, B. N. (1988) Ultimate possibilities of electron cooling. Tech. Rep. 88-61, Budker INP.
- [76] Kudelainen, V. I., Lebedev, V. A., Meshkov, I. N., Parkhomchuk, V. V., and Sukhina, B. N. (1982) Temperature relaxation in a magnetized electron beam. *Soviet Physics JETP*, **56**, 1191–1196.
- [77] Busch, H. (1926) Berechnung der Bahn von Kathodenstrahlen im axialsymmetrischen elektromagnetischen Felde. *Annalen der Physik*, **386**, 974–993.

- [78] Fadil, H., Orlov, D. A., Grieser, M., and Wolf, A. (2006) Design of a low energy electron cooler for the Heidelberg CSR. *Proceedings of European particle accelerator conference 2006*, pp. 1630–1632.
- [79] Jackson, J. (1999) *Classical electrodynamics*. Wiley.
- [80] Goodall, D. (1970) A.P.T division Culham laboratory.
- [81] Schwarz, M., Weiss, K., Heller, R., and Fietz, W. H. (2009) Thermal conductivity measurement of HTS tapes and stacks for current lead applications. *Fusion Engineering and Design*, **84**, 1748–1750.
- [82] American Superconductor (2010) *Service Note SN002 Guidelines for Handling and soldering Amperium Wire*.
- [83] American Superconductor (2006) *Service Note: Guidelines for Handling, Soldering and Splicing of High Strength Plus, Compression Tolerant and Hermetic Superconductor Wire*.
- [84] Ekin, J. (2007) *Experimental techniques for low temperature measurements: cryostat design, materials, and critical-current testing*. Oxford Univ. Press.
- [85] Powell, R. and Aboud, A. (1958) Electrical contact resistance of copper-copper junctions at low temperatures. *Rev. of Sci. Inst.*, **29**, 248–249.
- [86] Laquer, H. L. and Hammel, E. F. (1957) Cryogenic electromagnets. I. Feasibility study. *Rev. of Sci. Inst.*, **28**, 875–878.
- [87] Purcell, J. R. and Payne, E. G. (1963) High-field liquid H₂-cooled aluminum-wound magnet. *Rev. of Sci. Inst.*, **34**, 893–897.
- [88] Prodell, A. G. (1965) Liquid neon-hydrogen bubble chamber. *Rev. of Sci. Inst.*, **36**, 1174–1175.
- [89] Giger, U., Pagani, P., and Trepp, C. (1971) The low temperature plant for the Big European Bubble Chamber BEBC. *Cryogenics*, **11**.
- [90] Bewilogua, L. (1966) Neon in cryogenic engineering. *Cryogenics*, **6**, 24–26.
- [91] Richardson, R. N., Scurlock, R. G., and Tavner, A. C. R. (1995) Cryogenic engineering of high temperature superconductors below 77 K. *Cryogenics*, **35**, 387–391.
- [92] Richardson, R. N. and Tavner, A. C. R. (1995) Neon liquefaction system for high T_c experiments. *Cryogenics*, **35**, 195–198.

- [93] Bianchetti, M., Al-Mosawi, M. K., Yang, Y., Beduz, C., and Giunchi, G. (2006) A closed Neon liquefier system for testing superconducting devices. *AIP Conf. Proc.*, vol. 823 I, pp. 729–734.
- [94] Trociewitz, U., van Eck, H., van der Laan, D., Thompson, S., Mbaruku, A., Weijers, H., and Schwartz, J. (2002) Development of a LNe test facility. *Advances in cryogenic engineering, vol 47, pts A and B*, vol. 613 of *AIP Conf. Proc.*, pp. 139–146.
- [95] Stautner, W., Xu, M., Laskaris, E. T., Amm, K., Huang, X., Thompson, P. S., Budesheim, E., and Conte, G. (2009) The cryogenics of an MRI demonstrator based on HTS technology with minimum coolant inventory technology. *IEEE Trans. on Applied Superconductivity*, **19**, 2297–2300.
- [96] Griesheiml, M. (1986) *Gase-Handbuch*. Messer Griesheim GmbH.
- [97] Timinger, H., David, B., Eckart, R., and Overweg, J. (2008) Design parameters for cryogenic thermosyphons. *AIP Conf. Proc.*, vol. 985, pp. 1307–1314.
- [98] Felder, B., Miki, M., Tsuzuki, K., Izumi, M., and Hayakawa, H. (2010) Optimization of a condensed-neon cooling system for a HTS synchronous motor with Gd-bulk HTS field-pole magnets. *J. of Phys. Conf. Ser.*, **234**.
- [99] Ventura, G. and Risegari, L. (2008) *The art of cryogenics*. Elsevier.
- [100] McAdams, W. H. (1954) *Heat transmission*. McGraw-Hill.
- [101] Bich, E., Millat, J., and Vogel, E. (1990) The viscosity and thermal conductivity of pure monatomic gases from their normal boiling point up to 5000 K in the limit of zero density and at 0,101325 MPa. *J. of Phys. and Chem. Ref. Data*, **19**, 1289–1305.
- [102] Anonymous (1973) Cryogenie. *Bulletin d’Informations Scientifiques et Techniques*, **186**, 77–100.
- [103] Pavese, F., Fellmuth, B., Head, D. I., Hermier, Y., Hill, K. D., and Valkiers, S. (2005) Evidence of a systematic deviation of the isotopic composition of neon from commercial sources compared with its isotopic composition in air. *Analytical Chemistry*, **77**, 5076–5080.
- [104] Chyba, C. and Sagan, C. (1992) Endogenous production, exogenous delivery and impact-shock synthesis of organic molecules: An inventory for the origins of life. *Nature*, **355**, 125–132.

Acknowledgments:

I wish to thank Andreas Wolf for giving we the opportunity to take part in such an interesting and challenging project. Thank for your guidance, useful discussions and encouragement. I want to thank Klaus Blaum, our group leader for his constant support of the project. Amongst my colleagues I want especially thank Claude Krantz for his significant contribution in this work in such things as preparations of experiments at the TSR, building the DAQ of the LPCS, mounting of the LPCS. And special thanks for the proof reading of this thesis. I wish to thank Dima Orlov who was supervising me in the first two years of the project, when most of the key design ideas were proposed and discussed, who also taught me basic lessons on interactions with institute design and production facilities. My thanks to Michael Lange for the great deal of practical cryogenic experience he shared on the construction phase. I want to thank all of my colleagues in the Wolf/von Hahn part of the Blaum division for the positive and productive atmosphere they have created and maintained through these years.

As during this work I got to know a great part of the MPIK non-scientific staff I wish to thank many of them for their help. First I'd like to thank our German-class teacher Claudia Müller, who made all the further communications possible. We had a great time on this classes, and it turned to be really fruitful. Thank you Claudia, I hope your new students enjoy your classes as much as we did, and have as much use out of it. I'm glad I had an opportunity to work with Volker Mallinger, now-retired chief of the fine mechanical workshop. Thanks for the many practical discussions, proposed solutions and your good personal contacts to the industry, you sometimes had to pull to make them do things for us, even if they did not want to in first, but just for the old times sake they did. I want to thank Thorsten Spranz, Mr. Mallinger's successor, for his collaborative approach in running of small projects for us, always finding gaps to put them in, never making us wait long and never letting paperwork slow the production down. For countless small parts, leak-tests, crane-assisted mountings I'd like to thank Karl Hahn personally and his entire workshop, special thanks to Steffen Vogel, Christian Kaiser, Karlheinz Hallatschek and Rainer Flekensteiner. For the second half of countless parts and tests I'd like to thank Cryolab division consisting of Dirk Kaiser and Michael Frauenfeld, who help a lot during the struggle with leaks and safety approval of the LPCS.